MODELING AND MEASUREMENTS OF THERMAL TRANSPORT IN LI-ION BASED ENERGY CONVERSION AND STORAGE DEVICES

by

KRISHNA SHAH

Presented to the Committee Members

Dr. Ankur Jain (Committee Chairman)

Dr. Miguel Amaya

Dr. Abdolhossein Haji-Sheikh

Dr. Haiying Huang

Dr. Albert Tong

of The University of Texas at Arlington in Partial Fulfillment

of the Requirements

for the Completion of

DOCTOR OF PHILOSOPHY

THE UNIVERSITY OF TEXAS AT ARLINGTON

June 23rd, 2017

To my Grandparents

ACKNOWELDGEMENT

One of the key figures in the journey of a student is the mentor who sets an example for the student to aspire to. I have been very fortunate to have an exemplary guide in Dr. Ankur Jain. I had always fancied myself doing cutting edge scientific research and I reached out to Dr. Jain with the hope to get an opportunity to get involved in the research activities at Microscale Thermophysics Laboratory. He opened the door to his laboratory which in turn opened the gateway to the world of research for me. I will always be grateful to him for that. He played a much bigger role in my development as a researcher in the coming years. He effectively changed the way he played the role of a mentor as he saw me transitioning from a novice in the field in my early years to someone who can come up with innovative ideas and work with certain amount of autonomy. He played a big part in that transition itself. At times, he guided me when I sought his guidance. At other times, he would let me find the way out on my own when he knew I was capable of that. In the later years, he encouraged me to exercise my wings to fly. I can't say enough to express my gratitude for the role he has played in my career and in helping me achieve this significant milestone of my life. He has truly been my academic father.

I would like to take this opportunity to attempt to recognize the role my parents and my sister have played of being my support system without expecting anything in return. I would like to thank them for understanding my ambition to pursue this degree and taking the hardship in their lives so that I can fulfil my dreams. They believed in me in the toughest times during this journey and didn't let their struggles affect my conviction in pursuing the degree. I would like to thank Nimisha for the intellectual conversations related to my research and helping me crystalize my ideas better. I would like to thank her for the much needed moral support at times. I am indebted to the rest of

my family for their constant encouragement and support. I would like to thank my friend Avnish Thakkar for being there for me whenever needed.

I am thankful to my dissertation committee for being critical of my work and helping me realize my own shortcomings. The learning experience of defending my Ph.D. Dissertation will help me immensely as I am taking the next step into the research world. I would also like to thank everyone at Microscale Thermophysics Laboratory for their willingness to help and providing constructive criticism about my work over these years.

Finally, I would like to thank the MAE department at UTA for the financial support without which this wouldn't have been possible.

August 8, 2017

ABSTRACT

THERMAL MODELING AND MEASUREMENTS OF LI-ION BASED ENERGY STORAGE DEVICES

Krishna Shah

The University of Texas at Arlington, 2017

Supervising Professor: Ankur Jain

Heat transfer is of significant importance in energy conversion and storage devices such as Lithium-ion batteries for its safe operation and performance. Li-ion batteries are considered to be the state of the art among the energy storage devices due to their very high energy density and high power density. However, the safety of Li-ion batteries has become a concern in light of recent incidents, where there have been catastrophic events reported due to overheating of large battery packs. It is imperative to fully understand the nature of thermal transport in Li-ion cells. However, this has not been explored in detail yet.

Recent findings have suggested very large thermal conductivity anisotropy in cylindrical Li-ion batteries. In order to make accurate predictions of thermal behavior of the Li-ion cell, it is very important for thermal models to account for such a high degree of anisotropy.

In the present work, analytical steady state and transient thermal models have been developed for a cylindrical Li-ion cell. These models can be used as a tool to optimize design parameters and provide directions for further research in improving heat transfer inside a cell for improved safety.

A key conclusion from this thermal modeling work is the presence of a very large temperature gradient inside the battery, which indicates poor heat transfer from the core to the

surface of a cell, even if cooled aggressively at the surface. This can be explained by a thermal resistor model where the radial conduction resistance is shown to be the rate limiting factor in heat dissipation.

From the thermal modeling work, it appears that the heat from the core of the cell isn't being effectively transferred to the surface. This can be due to the large thermal resistance offered by the battery material which the heat has to propagate through. If an axial fluidic channel is provided through the core of the cell, it can significantly improve heat removal from the core of the cell.

Fluid flow through an annular channel is a promising strategy for cooling a Li-ion cell. A simplified analytical model is developed to understand this in detail. The model predicts temperature rise inside a cell as a function of average convective heat transfer coefficient over the channel surface and the size of the channel. Gain in terms of higher charge/discharge rate due to the effective cooling is also estimated. Reduction in temperature rise or increase in power density is also compared against the reduction in energy density as a function of channel size.

A related fundamental problem of conjugate heat transfer is solved. A classical example of such a problem is flow in a thick tube, which is similar to the problem of the proposed design of a Li-ion battery with an axial fluidic channel. A framework is proposed to solve conjugate heat transfer problem and is demonstrated by solving a couple of commonly occurring conjugate heat transfer problems in reality. The method is validated with a well validated past model and finite element solver.

Experimental demonstration of the conceptual design of a Li-ion cell with an annular channel has been done on a thermal test cell. Various cooling strategies, active as well as passive, have been implemented, evaluated and compared. Active cooling is demonstrated by passing air

through the channel in the thermal test cell. For passive cooling, a heat pipe/copper rod is inserted in the channel with the tip protruding outside the cell. The results from this work show effectiveness of internal cooling of a Li-ion cell over convectional external cooling.

Thermal runaway leads to catastrophic events in energy storage devices with high energy density, such as a pack of Li-ion cells. An experimentally validated thermal model is developed to capture the nonlinear nature of heat generation in a Li-ion cell due to the temperature dependent behavior of exothermic electrochemical reactions. The thermal modeling effort lead to the discovery of a non-dimensional number named as Thermal Runaway Number (TRN) which can help predict onset of thermal runaway and determine thermal stability of a Li-ion cell. This analysis can prove to be crucial to better understand thermal runaway phenomena in Li-ion batteries.

Further, thermal modeling to compute temperature in Li-ion cell with temperature dependent heat generation has also been developed. The model has been experimentally validated by simulating temperature dependent heat generation for different values of heat generation parameters. Effect of heat transfer parameters on temperature has also been analyzed.

LIST OF FIGURES

Figure 8.7 Temperature computed for individual reactions and the total of individual reactions

LIST OF TABLES

CHAPTER 1

INTRODUCTION

A significant amount of research has been carried out in the past few decades on Li-ion batteries for energy storage. Despite several advantages over other energy storage technologies such as high specific energy and energy density [1-2], the commercialization of Li-ion battery technology has been slower than expected due to risks associated with high temperature operation and other safety-related concerns. Such concerns have been highlighted in several recent incidents, where Li-ion batteries and battery packs have been found to be responsible for fires aboard aircrafts [3-4]. These incidents underscore the importance of developing a fundamental understanding of the thermal characteristics of Li-ion cells, particularly the capability of temperature prediction during the operation of a cell.

Similar to any other energy storage device, charging or discharging a Li-ion battery results in heat generation, which causes an increase in temperature due to exothermic electrochemical reactions and Joule heating [5-6]. Heat generation rate is known to be a function of depth-of-discharge, temperature and the rate at which a cell is charged or discharged, often referred to as C-rate [7].

There are severe limitations to temperature rise permitted in a Li-ion cell, particularly for military applications with high reliability requirements. Thermal runaway at high temperature is a well-known problem in Li-ion batteries [8-9]. While a small temperature rise is known to actually improve performance due to reduced impedance [10], a larger temperature rise results in a series of exothermic

reactions associate with certain electrochemical processes including decomposition of the Solid-Electrolyte Interface (SEI) [11-12], short circuit due to separator layer rupture from dendrite formation, which ultimately leads to catastrophic failure [8]. Fundamentally, thermal runaway in a Li-ion cell is a cascade of successive processes and reactions that feed into one another through heat generation that increases with temperature, eventually leading to explosion and fire [9,13]. Pertinent processes in thermal runaway include decomposition of the solid-electrolyte interface [14], various chemical reactions involving the electrolyte and electrode binder [11,15,16], and eventually, decomposition of the electrolyte [17] and the positive electrode active material [18]. A large amount of literature is available on understanding each of these processes [9,13,14,15,19,20]. In particular, the reaction kinetics and heat generation profiles of these processes have been widely studied, both theoretically [19] and through experimental measurements using tools such as Differential Scanning Calorimetry (DSC) and Accelerated Rate Calorimetry (ARC) [14,15,20]. These processes are modeled using Arrhenius reaction kinetics, with a reaction rate that increases exponentially with temperature [9,13]. Numerical values of these reaction rates and heat generation rates, as well as their temperature dependence have been determined [13]. Due to these temperature dependent processes and heat generation, Li-ion cells must operate in a very narrow temperature window. In addition to absolute temperature rise, spatial uniformity of the temperature field is also desirable [21], since this prevents imbalance of temperature-dependent electrochemical reaction

rates within the cell or battery pack. This makes thermal modeling and thermal management of Li-ion cells of great importance.

Despite the clear importance of thermal management of cylindrical Li-ion batteries, only a limited amount of literature is available on thermal management and cooling of Li-ion batteries. Only a few studies have reported measurement of thermophysical properties such as thermal conductivity and heat capacity of Li-ion cells [12, 22]. Early work in this direction did not recognize the strong anisotropy in thermal conduction in a Li-ion cell. Recent measurements have reported a method for rapid measurement of anisotropic thermal conductivity as well as heat capacity of a Li-ion cell [14]. These measurements indicate nearly two orders of magnitude difference in the radial and axial thermal conductivities of a Li-ion cell [14]. It is important to determine the limits of air/liquid based convective cooling approaches [7] and to develop a sound theoretical framework to understand the dependence of temperature rise in a convectively cooled Li-ion cell on various parameters, such as geometry, cooling, etc. A first step towards effective thermal management of Li-ion cells is the capability to accurately model and predict temperature fields within an operating cell. The temperature field resulting from the heat generation depends on a variety of parameters including geometry, material properties, etc. and needs to be modeled accurately. A number of models are available for predicting volumetric heat generation rates as a function of electrical operating parameters of the cell, ranging from very simple, which assume uniform heat generation rate [5], to very sophisticated [9; 21]. Some papers also model

volumetric heat generation as a space dependent parameter, accounting for Joule heating that occurs primarily at the two current collector tabs, resulting in non-uniformity, particularly at high discharge rates [9]. Heat generation modeling is complicated by the fact that heat generation may vary with time in specific applications, if the charge/discharge rate changes [6]. For example, in an electric vehicle, changes in demand on the battery due to vehicle acceleration and other factors may result in the heat generation rate being a function of time.

In contrast to heat generation modeling, limited work has been reported on temperature field prediction [9, 23-28], which is a more critical parameter for safety and performance considerations. While these models provide a basis for temperature prediction, there are several shortcomings. Many past models are one-dimensional [24] and do not account for the spirally-bound geometry of a cylindrical Li-ion cell, boundary conditions encountered in actual applications, or the thermal conduction anisotropy in a cylindrical cell. Several thermal models of a Li-ion cell reported in the recent past treat the cell as a lumped body with a single temperature [24,25], which may not be an appropriate assumption for most applications. Three-dimensional thermal models for a Li-ion cell have been presented [26], but this model is solved numerically, and does not offer analytical, closed-form solutions for the temperature field. Some recent work accounts for the spiral nature of the electrodes in a cylindrical Li-ion cell [29], but this work neglects the axial dimension of the cell and does not present a closed-form analytical solution. Recent work has presented analytical models for temperature distribution

in prismatic Li-ion cells [27,28], but these models do not readily apply to a cylindrical geometry, where heat transfer characteristics are fundamentally different from a prismatic cell.

The operation of a Li-ion cell is inherently a transient thermal phenomenon. As a Li-ion cell is charged and discharged at a rate that changes with time based on variations in load requirements and power availability, the heat generation rate within a Li-ion cell also changes as a function of time. For example, a sudden increase in power demand may produce pulsed spikes in the heat generation rate in the cell as a function of time, due to which the cell temperature may also rise. Depending on the thermal mass of the cell and the C-rate, a steady-state may never actually be reached, and the entire operation of the cell may be transient in nature. In such a case, it is important to predict the nature of temperature spikes in response to changes in C-rates, so that appropriate thermal management mechanisms may be designed. This highlights the need for a thorough fundamental understanding of the transient thermal behavior of a Li-ion cell and the capability to predict temperature rise as a function of time due to time-varying heat generation rate.

Some research has also been carried out on thermal modeling and measurements for Li-ion cells in thermal runaway situations [19, 8,30, 31, 32, 33,34]. Analytical methods and simulation tools [19,8,17,18,30,31] have been used for modeling thermal behavior of a cell at elevated temperatures. Experiments have been carried out to measure temperature of a cell or an appropriate thermal surrogate [32,33] during runaway. However, not much work has been carried out

on connecting heat removal and heat generation processes that occur during thermal runaway. While heat generation is a function of the chemical reactions occurring within the cell, heat removal from the cell comprises of two processes that occur in series [35,36,37] – thermal conduction within the cell to its outside surface, and heat removal which is usually through convection from the outside surface to the ambient. The nature of interaction between these heat generation and heat transfer processes eventually determines the thermal state of the cell, and whether thermal runaway occurs or not. It is critical to model both in a holistic fashion to better understand thermal runaway, and design the means to prevent thermal runaway. Specifically, it is of interest to determine how thermal transport properties of the cell and its ambient conditions influence and govern the occurrence of thermal runaway. Such experimentally-verified theoretical limits on the occurrence or avoidance of thermal runaway may result in valuable design tools for safety of Li-ion cells.

The interaction between heat generation and heat removal has been represented in past papers in the form of a Semenov plot [37,38], that compares the rates of heat generation and heat removal as functions of the temperature of the cell. A Semenov plot uses the imbalance between the two processes – which increase linearly and exponentially respectively as functions of temperature – as the basis for predicting thermal runaway [37,38]. However, this approach assumes the cell to be a lumped thermal mass with uniform temperature throughout the cell volume. As shown by recent measurements [39,40], this may not be an accurate assumption.

As a consequence, the Semenov analysis predicts the thermal runaway process to be independent of the thermal conductivity of the cell, which is not accurate in several cases. For example, the Biot number [41] for a typical 26650 cell in natural convection conditions can be estimated to be 2-6.5, based on recent thermal conductivity measurements of the cell [22,42]. A value of Bi>1 indicates strong temperature gradients within the cell, making the lumped mass based Semenov analysis inaccurate. Because the Semenov approach neglects heat transfer within the cell, it has not been possible so far to predict the internal and external thermal conditions needed to prevent thermal runaway for a specific cell chemistry, with well-known chemical kinetics and heat generation rates as functions of temperature. Accounting for this phenomenon will help optimize materials design from a thermal perspective, and help maintain a balance between internal and external heat transfer for avoiding thermal runaway.

In the present work, a cell-level steady-state analytical thermal model for a cylindrical Li-ion cell being cooled on the outside surface by convective flow is presented. Thermal conduction anisotropy within the cell is modeled. Closed-form analytical solutions for both uniform and space-dependent heat generation rates are presented. An analytical solution to the energy conservation equations that govern transient thermal transport within a heat-generating cylindrical Li-ion cell is also described and implemented to develop a transient model. This approach results in expressions for the temperature field in the cell due to time-varying heat generation rate. This experimentally-validated analytical model is used to develop an

understanding of the role of various physical parameters on transient temperature rise. The thermal response of the cell to a spike in heat generation, and to a sequence of multiple discharge-charge cycles is also investigated. Various trade-offs between thermal design and other cell-level design considerations are identified.

The Steady-state and transient models for the thermal conduction within a cylindrical Li-ion cell highlight the importance of radial thermal conductance within the cell in determining the temperature field of the cell. One particular challenge in the cooling of cylindrical Li-ion cells is that while the radial outer surface is most commonly available for heat dissipation, thermal conductance within the cell in the radial direction is particularly poor. Cooling at the outer surfaces is likely to be ineffective for the core regions of the cell, which are farthest from the outer surface. Due to the relatively large axial thermal conductivity, axial conduction within the cell may provide an effective heat dissipation pathway. However, the two outer surfaces at the axial ends of the cylinder are normally used for connecting to the anode and cathode, and are not available for heat dissipation.

Theoretical and experimental analysis has also been carried out to investigate thermal runaway in Li-ion cells by extending the Semenov analysis to account for heat transfer within the cell. The governing energy conservation equation that accounts for both heat generation and heat removal processes is solved to determine a non-dimensional parameter – named the Thermal Runaway Number (TRN) – whose value is shown to govern if thermal runaway occurs. This parameter includes contributions from heat transfer processes within and outside

the cell, as well as the rate of increase in heat generation with temperature. Results indicate that thermal conductivity within the cell is a critical thermal property governing runaway. Experiments that implement a temperature-dependent heat generation with a controllable temperature slope are carried out to validate the theoretical model. These experimental data are in good agreement with theoretical results, and demonstrate successful avoidance of thermal runaway through changes in the convective heat transfer coefficient external to the cell. Design guidelines that predict the parameter space in which thermal runaway is prevented are developed using the model. The experimentally-verified fundamental insights in this paper may lead to design guidelines for thermal properties of the cell and its ambient for prevention of thermal runaway.

In addition to thermal runaway analysis, a non-linear semi-analytical thermal model has been developed. This thermal model can be utilized for both nominal and thermal abuse conditions to compute temperature field in a cell. Thus, this if conditions favorable to thermal runaway exist. The model is based on solution of non-linear heat equation with piecewise linear heat generation profile, with respect to temperature. The model is validated experimentally by simulating temperature dependent heat generation in a thermal test cell. The simulated temperature dependent heat generation has been made to behave similar to exothermic heat generation in a Li-ion cell. The model is used to analyze effect of various heat generation, heat transfer and heat dissipation parameters on the thermal state and temperature of the cell. Effect of high discharge rate in pushing a cell into

thermal runaway has been shown by the model. In addition, simulation of thermal abuse such as oven test is also demonstrated using this model. Finally, this model has been utilized in determining thermal thresholds in terms of various parameters in heat generation, heat transfer and heat dissipation. Such analysis and the model presented in this work can also help determine guidelines for future considerations as this technology continues to develop.

Overheating is a key issue in Li-ion based energy storage devices, which raises safety related concerns. This makes thermal management of Li-ion cells technologically important. A variety of approaches for cell cooling have been investigated. Convective cooling with air or liquid flow over the cell [43], and coldplate [44] cooling are two commonly used approaches. Thermal management using phase change materials (PCMs) and microchannel fluid flow have also been investigated [45-47]. Fundamentally, the process of heat removal from a Li-ion cell is a two-step process – heat generated inside the cell is first conducted to the outside surface of the cell, followed by heat removal from the surface [35]. The second step of this process occurs typically through convection with a coolant, such as air, or conduction through the surrounding material of the battery pack. It has been shown that thermal conduction within the Li-ion cell is usually the slower, and hence rate-determining step [35]. This emanates from the poor thermal conductivity of the Li-ion cell, particularly in the direction normal to the electrodes [48]. This makes it particularly difficult to remove heat generated in the core of the cell, resulting in a hot core and a large temperature gradient within the cell. Measurements have shown

as much as 24 °C temperature gradient between the core and outer surface of a 26650 cell at 10C discharge rate [39]. While a phase change material may address short transient power spikes, this approach does not address the problem of steady-state thermal management of Li-ion cells. This approach may also be difficult to integrate with the manufacturing of Li-ion cells and may interfere with the performance of the cell. Finally, inclusion of any non-electrochemical material inside the cell will reduce energy storage capacity. An alternative possible approach is to provide a through-hole along the axis of the cell and flow a liquid or gas coolant through this channel. This opens up a new mechanism for heat removal which reaches the core of the cell, making it more effective than cooling the outer surface. However, this results in reduced cell capacity, since the cell volume is reduced. In view of this trade-off, it is important to carry out a comprehensive thermal analysis to fully understand the thermal benefits of coolant flow in an annular Li-ion cell, and compare these benefits with costs associated with reduced cell capacity. Such an exercise may help determine the feasibility of this thermal management approach, and develop practical guidelines for multi-physics optimization design and operation of Li-ion cells.

As a part of the present work, analytical models for determining the steady-state and transient temperature distributions in a heat-generating annular Li-ion cell containing an axial through-hole with coolant flow are developed. The effect of the coolant is modeled using a convective heat transfer coefficient at the inner wall. The governing energy conservation equations are solved to derive an expression for steady-state and transient temperature distributions. Results are in excellent

agreement with finite-element simulations. The effect of various thermal parameters, including convective boundary conditions and precooling of the coolant, on temperature distribution is examined. It is shown that precooling provides limited benefit in thermal performance of the cell. It is shown that the provision of axial cooling reduces the cell temperature, making it possible for the cell to dissipate more heat. This provides additional thermal head that may be used to operate the cell at a higher C-rate. This can be viewed as a trade-off between the energy and power capacities of the cell. By quantifying this trade-off, this work contributes towards a comprehensive multi-physics understanding of this type of Li-ion cell thermal management approach.

Following up on modeling efforts, experimental work is also done to evaluate and demonstrate core cooling of Li-ion cell. It investigates thermal management of a Li-ion cell utilizing cooling through a hollow tube passing through the cell. The effectiveness of cooling a thermal test cell through internal air flow, as well as heat pipe and metal rod insertion is experimentally investigated. A thermal test cell of the same dimensions as a 26650 Li-ion cell, and similar thermal properties is fabricated. Heat generation in the test cell through Joule heating is used to mimic electrochemical heating in a Li-ion cell. Experimental data is shown to be in good agreement with finite-element simulation results. This approach is shown to result in effective cooling of the Li-ion cell due to the direct access that this provides to the core of the cell. Despite the manufacturing challenges and thermal-electrochemical trades that an embedded heat pipe may present, the

dramatic improvement in thermal management may make this an attractive approach for thermal management of Li-ion cells.

The analytical model developed for an annular cylinder to model a Li-ion with axial fluidic channel led to a more fundamental problem of conjugate heat transfer. Conjugate heat transfer involving coupled conduction and convection is of significance in many engineering systems. A large volume of past research [50-63] has been devoted to solving temperature fields for a fluid flowing in contact with a solid body, wherein thermal convection within the fluid domain occurs in conjunction with conduction within the solid domain. While the effect of conduction in the solid body is important in the thermally developing fluid region [51,64], it is also clearly important in case of internal heat generation in the solid that is being convected by the flowing fluid [65]. This makes it critical to develop analytical solutions for conjugate problems involving convection in fluid flow and conduction in a solid which is in contact with the fluid flow. Problems involving external flow and internal flow are both of interest.

Derivation of solutions for convection-only or conduction-only problems is relatively straightforward. Well-known solutions exist for specific boundary conditions such as constant temperature or constant heat flux [50,53-54]. Similarly, theoretical solutions for a variety of conductions problems are also available [66,67]. However, analytical derivation of temperature distribution in conjugate problems is a lot more challenging [68]. A fundamental problem underlying several conjugate heat transfer problems was first solved by Graetz [52-53], who derived

an analytical expression for temperature in a fluid flowing through a duct with constant temperature boundary condition, assuming that the flow is hydrodynamically developed and thermally developing. Analytical expressions for eigenvalues and eigenfunctions for this solution have been computed [56], and this solution has been used to derive the solution for a more general problem with continuously or discretely varying wall temperature using linear superimposition [52,56-57]. Boundary layer solution for fluid flow over a plate for thermal boundary layer non-similarity arising from both velocity field and streamwise variation of temperature have been analyzed [55]. The case of constant or axially varying wall heat flux has also been analyzed. While axial conduction in the fluid is mostly neglected, some papers have accounted for this phenomenon [58,69], which is relevant for specific technological applications.

While the classical convection problems for internal and external flows do not consider thermal conduction within the solid body in contact with the fluid flow, solutions to these problems provide the building blocks for deriving temperature distributions in conjugate problems, where thermal conduction in the solid and thermal convection in the fluid must be considered simultaneously. A number of approaches have been presented for solving this conjugate problem. A series form of the wall temperature has been assumed, and energy conservation at the solid-liquid interface has been used to derive expressions for coefficients of the series form [59-60,70]. This results in analytical expressions for the entire temperature distribution. In particular, expressions for pipe flow [59], a plate in liquid or gas

flow [60-61], flow between parallel plates [59,71] and for turbulent flows [69] have been presented. A solution for the conjugate problem of flow over a flat plate has also been presented using the method of the asymptotic solution of singular integral equations [62]. In addition to such approaches, the integral transform technique has also been used for solving conjugated heat transfer problems [72-73]. Semi-analytical [74-78] and purely numerical [79-81] techniques have also been used. These papers utilize discretization based on finite-element or finite-difference based methods.

This work presents a solution for the conjugate heat transfer problem using an iterative approach that utilizes analytical solutions of both conduction and convection problems solved independently. Solutions to these two sub-problems are coupled with each other through temperature continuity and energy conservation at the solid-liquid interface. Both internal and external flow problems are addressed. In this method, the temperature at the interface between adjacent layers is assumed, based on which the temperature distribution in each layer is determined analytically. Using energy conservation at the interface between adjacent layers, the interface temperature distribution is determined. This is then used to iteratively improve the wall temperature distribution until reasonable convergence. Such an approach has been used in the past for analytical determination of temperature distribution in thermal conduction problems in a multi-layer solid body [82-84]. In addition, a few papers have also utilized a similar iterative method for semi-analytical solution of conjugate heat transfer problems,

wherein a finite-element or finite-difference discretization approach is used to numerically solve the thermal conduction problem [76-78,84]. The present approach determines both fluid and solid temperature distributions analytically. This results in reduced mathematical complexity compared to classical, non-iterative approaches [59-61,69,72], without the need to resort to discretization and numerical techniques used in past semi-analytical approaches [74-78]. It is found that only a small number of iterations are sufficient for reasonable convergence of results. The iterative method is utilized to analyze conjugate heat transfer in two specific problems – the cooling of a hollow heat generating cylinder with anisotropic thermal conductivity, and the cooling of a heat generating solid block due to fluid flow over the block.

CHAPTER 2

MODELING OF STEADY-STATE CONVECTIVE COOLING OF CYLINDRICAL LI-ION CELLS

Shah, K., Drake, S. J., Wetz, D. A., Ostanek, J. K., Miller, S. P., Heinzel, J. M., & Jain, A. (2014). Modeling of steady-state convective cooling of cylindrical Li-ion cells. Journal of Power Sources, 258, 374-381.

Abstract

While Lithium-ion batteries have the potential to serve as an excellent means of energy storage, they suffer from several operational safety concerns. Temperature excursion beyond a specified limit for a Lithium-ion battery triggers a sequence of decomposition, and release, which can preclude thermal runaway events and catastrophic failure. As a result, electronic controls and liquid or air-based convective cooling are often provided, particularly in high-rate discharge applications where significant heat generation is expected. To optimize these approaches, it is important to accurately model the thermal response of Lithium-ion batteries to convective cooling. This manuscript presents closed-form analytical solutions for the steady-state temperature profile in convectively cooled cylindrical Lithium-ion batteries. These models account for the strongly anisotropic thermal conductivity of cylindrical Lithium-ion batteries due to the spirally wound electrode assembly. Model results are in excellent agreement with experimentally measured temperature rise in a thermal test cell. Results indicate that improvement in radial thermal conductivity and improvement in the axial convective heat transfer coefficient may result in significant peak temperature reduction. Battery sizing optimization using the analytical model is discussed, indicating the dependence of thermal performance of the cell on its size and aspect ratio. Results presented in this manuscript are expected to aid in accurate thermal design and thermal management of Lithium-ion batteries.

Keywords: Lithium-Ion Batteries, Convective Cooling, Thermal Management, Safety, Thermal Runaway.

2.1 Analytical Model: Uniform Heat Generation

Consider a cylindrical Lithium-ion battery of radius R and height H shown schematically in Figure 2.1. Volumetric heat generation rate Q is assumed within the cell due to electrochemical reactions and Joule heating. In this Section, Q is assumed to be spatially uniform, whereas Section 3 considers the case where Q may be a function of space. It is assumed that the outside surfaces of the cell are being cooled with heat transfer coefficients of h_r and h_z for the curved surface and the end surfaces respectively.

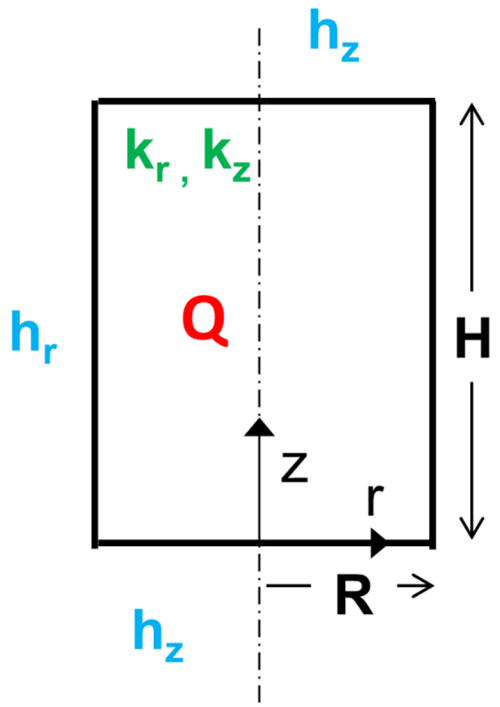

Figure 2.1: Schematic diagram showing battery geometry and thermal parameters for the analytical thermal model. Q may be uniform (Section 1.1) or may vary radially/axially (Section 22.2).

The ambient temperature for convective cooling is assumed to be T_0. The thermal conductivities in radial and axial directions are assumed to be k_r and k_z respectively. Recent measurements show that k_r and k_z differ by nearly two orders

of magnitude [22], thereby indicating the importance of anisotropic modeling of thermal conductivity in a cylindrical Li-ion cell. The governing steady state energy conservation equation in this case is given by

$$\frac{k_r}{r}\frac{\partial}{\partial r}\left(r\frac{\partial \theta}{\partial r}\right)+k_z\frac{\partial^2 \theta}{\partial z^2}+Q=0 \qquad (1)$$

where $\theta(r,z)$ is the temperature rise above ambient, given by

$$\theta(r,z)=T(r,z)-T_0 \qquad (2)$$

Equation (1) is a non-homogeneous partial differential equation subject to four homogeneous boundary conditions given by

$$\frac{\partial \theta}{\partial z}=\frac{h_z}{k_z}\theta \qquad \text{at z = 0} \qquad (3)$$

$$\frac{\partial \theta}{\partial z}=-\frac{h_z}{k_z}\theta \qquad \text{at z = H} \qquad (4)$$

$$\frac{\partial \theta}{\partial r}=0 \qquad \text{at r = 0} \qquad (5)$$

$$\frac{\partial \theta}{\partial r}=-\frac{h_r}{k_r}\theta \qquad \text{at r = R} \qquad (6)$$

The boundary conditions in equation (5) represent the requirement of symmetry and finiteness of the temperature profile at r=0, whereas boundary condition in equations (3), (4) and (6) represent energy balance at the respective surface.

The final solution is given by

$$\theta(r,z) = s(z) + w(r,z) \tag{7}$$

where

$$s(z) = \frac{QH^2}{2k_z}\left[\frac{z}{H}\left(1-\frac{z}{H}\right)+\frac{1}{Bi_H}\right] \tag{8}$$

and

$$\mathrm{w(r,z)} = \sum_{\mathrm{n=1}}^{\infty} \mathrm{A_n I_0(\lambda_n r)[\mu_n HCos(\mu_n z) + Bi_H Sin(\mu_n z)]} \tag{9}$$

Here,

$$A_n = \frac{-Bi_R \cdot \frac{1}{H}\int_0^H s(z)\left[\mu_n HCos(\mu_n z)+Bi_H Sin(\mu_n z)\right]dz}{\frac{1}{2}\left[(\mu_n H)^2 + Bi_H{}^2 + 2Bi_H\right]\left[\lambda_n R \cdot I_o'(\lambda_n R) + Bi_R I_o(\lambda_n R)\right]} \tag{10}$$

The eigenvalues μ_n are obtained from roots of the transcendental equation

$$Tan(\mu H) = \frac{2Bi_H \cdot (\mu H)}{(\mu H)^2 - Bi_H{}^2} \tag{11}$$

where $\mathrm{Bi_H}$ and $\mathrm{Bi_R}$ are axial and radial Biot numbers, respectively, defined as $Bi_H = \frac{h_z H}{k_z}$ and $Bi_R = \frac{h_r R}{k_r}$.

Finally,

$$\lambda_n = \sqrt{\gamma} \cdot \mu_n \tag{12}$$

where γ is the degree of anisotropy given by

$$\gamma = \frac{k_z}{k_r} \tag{13}$$

For the case of Li-ion batteries, γ is expected to be greater than one. Recent measurements indicate a value of γ=200 for 26650 geometry $LiFePO_4$ cells [22].

In addition to the peak temperature rise, another important thermal parameter of interest is the temperature gradient within the cell, defined as the difference between the maximum and minimum temperature. In particular, it is desirable to reduce the difference between maximum and minimum temperature in a cell, since a gradient leads to performance imbalance, etc. From equation (7), the temperature gradient within the cell is given by

$$\theta_g \equiv \theta_{\max} - \theta_{\min} = \frac{QH^2}{8k_z} + \sum_{n=1}^{\infty} A_n \left(\mu_n H Cos\left(\frac{\mu_n H}{2}\right) + Bi_H Sin\left(\frac{\mu_n H}{2}\right) - \mu_n H \cdot I_0(\lambda_n R) \right) \tag{14}$$

Equation (14) provides a means to quantify the temperature non-uniformity within the cell as a function of various non-dimensional parameters.

2.2 Analytical Model: Non-Uniform Heat Generation

Since the rate of electrochemical reactions contributes to heat generation, spatial variation in rate of electrochemical reactions may lead to space-dependent Q. In such a case, the temperature field in the Li-ion cell continues to be governed by equation (1) and boundary conditions (3) - (6), except that the Q term in equation (1) is a function of space. Two particular cases of interest are considered in this Section: one in which Q is a function of z only, Q(z); and second, in which Q is a function of r only, Q(r).

2.2.1 Solution for axially varying heat generation rate:

Any given well-behaved function Q(z) can be approximated by an N-order polynomial as follows [85]:

$$Q(z) = \sum_{i=0}^{N} c_i \left(\frac{z}{H} \right)^i \tag{17}$$

where the coefficients c_i are chosen appropriately to fit the function Q(z).

With such a polynomial approximation for Q(z), the function s(z) is given by

$$s(z) = -\frac{H^2}{k_z} \sum_{i=0}^{N} \frac{c_i}{(i+1)(i+2)} \left[\left(\frac{z}{H} \right)^{i+2} - \frac{\left(\frac{z}{H} + \frac{1}{Bi_H} \right)(Bi_H + i + 2)H}{2 + Bi_H} \right] \tag{18}$$

Equation (18) above, together with equations (8) and (10) - (13) completely define the temperature field for axially varying heat generation.

2.2.2 Solution for radially varying heat generation rate:

In case the heat generation rate varies in the radial direction, a solution of the temperature field may be derived by first approximating Q(r) with a polynomial expansion,

$$Q(r) = \sum_{i=0}^{N} c_i \left(\frac{r}{R} \right)^i \tag{19}$$

The solution approach for this case is similar to one described in Section 2 following equation (7). The solution is given by

$$\theta(r,z) = s(r) + \sum_{n=1}^{\infty} A_{1n} J_0(\lambda_n r) \left[\begin{array}{l} Cosh(\mu_n z) + Cosh(\mu_n (H-z)) + \\ \frac{h_z}{k_z \mu_n} [Sinh(\mu_n z) + Sinh(\mu_n (H-z))] \end{array} \right] \tag{20}$$

where

$$A_{1n} = \frac{-h_z \int_0^R r s(r) J_0(\lambda_n r) dr}{\frac{J_0^{\,2}(\lambda_n R)}{2\lambda_n^{\,2}} \left[(\lambda_n R)^2 + \left(\frac{h_r R}{k_r} \right)^2 \right] \left[\begin{array}{l} k_z \mu_n \left(Sinh(\mu_n H) + \frac{h_z}{k_z \mu_n} Cosh(\mu_n H) \right) + \\ h_z \left(Cosh(\mu_n H) + \frac{h_z}{k_z \mu_n} Sinh(\mu_n H) \right) \end{array} \right]} \tag{21}$$

The eigenvalues μ_n are determined from roots of the transcendental equation

$$\frac{h_r R}{k_r} J_0(\lambda_n R) + \lambda_n R J_0'(\lambda_n R) = 0 \tag{22}$$

where μ_n is related to λ_n through the degree of anisotropy and is given by equations using equation (12) - (13).

Also, s(r) is given by

$$s(r) = \sum_{i=0}^{N} \frac{c_i R^2}{(i+2) k_r} \left[\frac{1}{Bi_R} + \frac{1}{(i+2)} \left(1 - \left(\frac{r}{R} \right)^{i+2} \right) \right] \tag{23}$$

Equations (20) - (23) define the temperature solution in the case of a radially varying heat generation. For more details on the derivation of these analytical solutions, please refer to [35].

The next Sections discuss experimental validation of the analytical model, and presents a parametric analysis of the dependence of temperature field on various parameters including the degree of anisotropy and external convective

cooling coefficient. A few design studies enabled by the analytical models are also discussed.

2.3 Experimental Validation

The temperature model presented in this paper is validated by comparison with experimental data. Experimental data on temperature rise at different heating powers and analytical model results are both plotted in Figure 2.2. The analytical

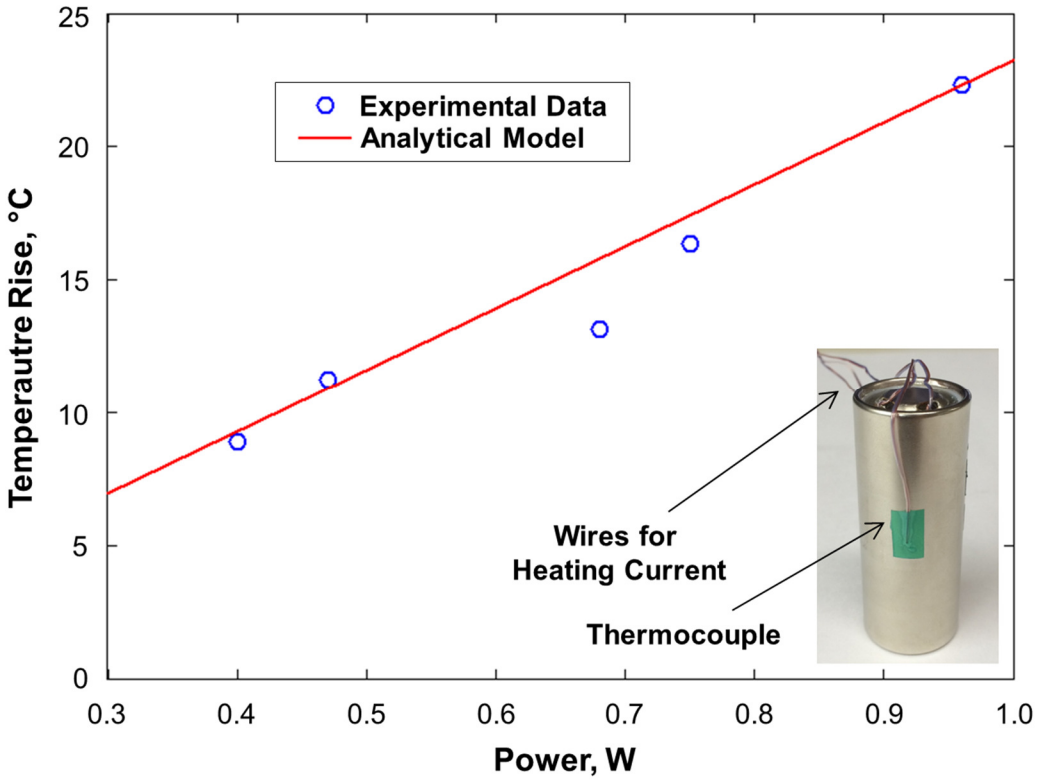

Figure 2.2. Comparison of analytical model with experimental data on temperature rise at the outer surface of a 26650 cell at mid-height as a function of heating power.

model is in good agreement with experimental data, and captures the trend of temperature rise as a function of heating power.

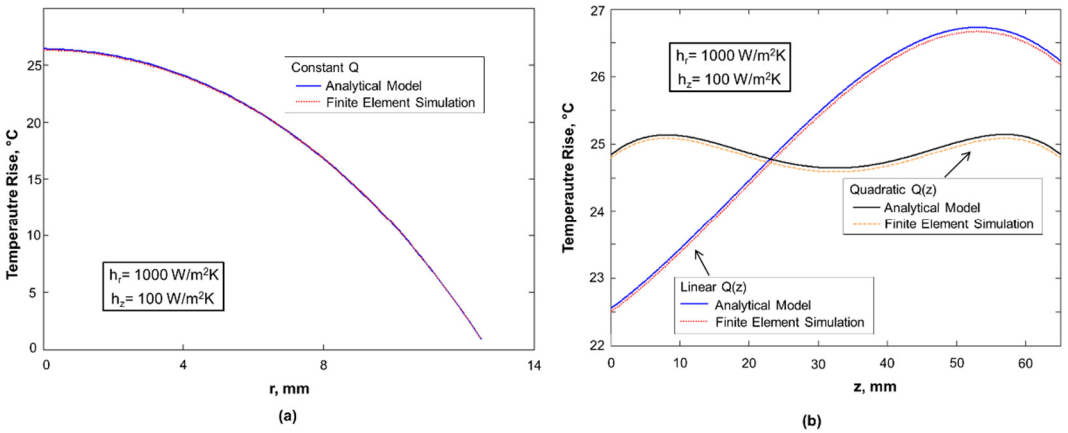

Figure 2.3 Comparison of analytical models presented in Sections 2.1 and 2.2 with finite-element simulation results for (a) radial temperature variation at z = H/2 with uniform heat generation, and (b) axial temperature variation at r = 0 with two cases of axially varying heat generation.

In addition, the analytical model presented in this paper is also compared with finite-element model (FEM) simulations. Figure 2.3(a) shows the radial temperature variation at mid-cell height for uniform heat generation of 6 W over the entire cell volume. While the analytical model accounts for any general polynomial, Figure 2.3(b) shows the axial temperature variation at r = 0 for two specific cases of z-dependent heat generation rate: a linear variation given by $Q(z) = 2 \cdot Q_{\max} \frac{z}{H}$ and a quadratic variation given by $Q(z) = 12 \cdot Q_{\max} \left(\frac{z}{H} - \frac{1}{2} \right)^2$. In each case, the analytical model compares well with FEM results.The temperature solution for various cases in Sections 1 and 2 is derived in the form of an infinite series. It is found that these series converge very quickly as the number of terms increases. Considering only three eigenvalues is sufficient for temperature computation with an error of less than 1%.

2.4 Results and Discussion

2.4.1 Dependence of temperature field on γ and h_r

Figure 2.4 shows a steep increase in peak temperature at low values of k_r. The measured value of k_r [22] is indicated with a blue arrow.

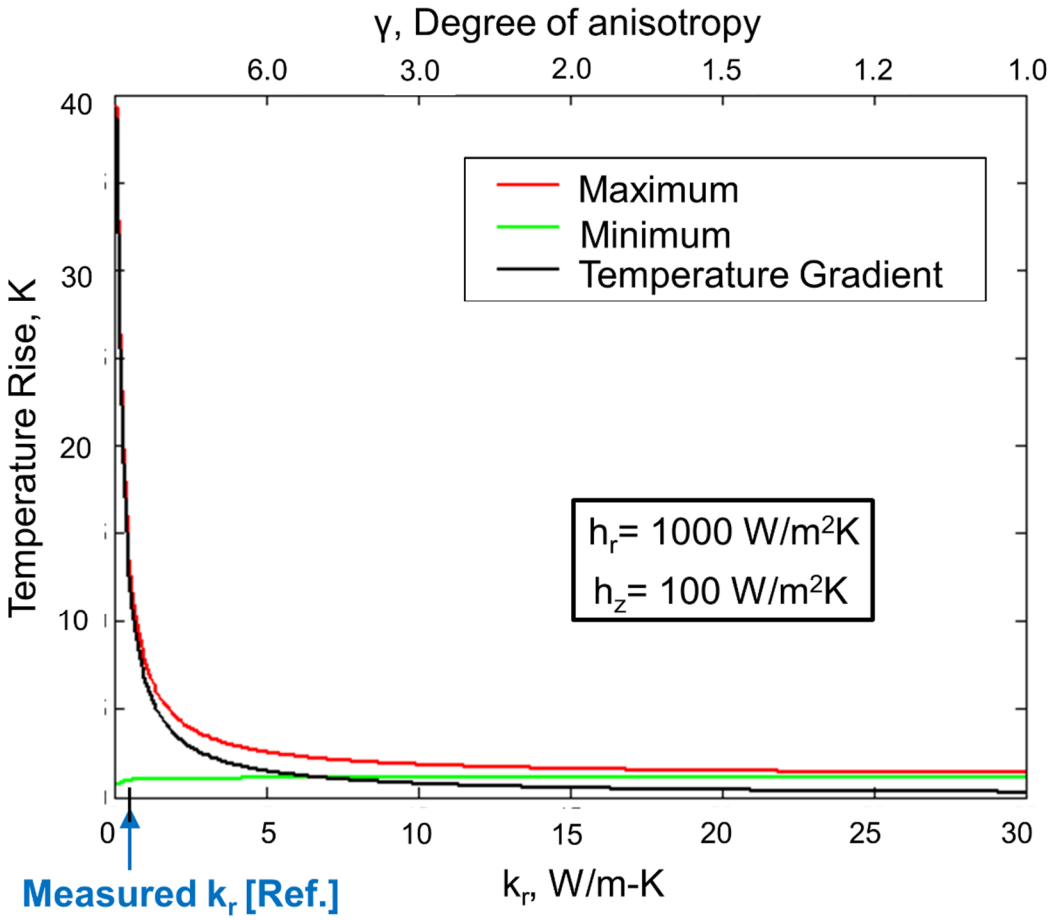

Figure 2.4. Variation of peak temperature rise with radial thermal conductivity of battery material, showing significant potential for temperature reduction by improving radial thermal conductivity.

This figure shows that the greater the degree of anisotropy, the larger is the peak temperature rise. There is significant potential for reducing temperature rise by improving radial thermal conductivity and, hence, reducing γ. In effect, radial conduction is the rate-limiting step in heat dissipation. In most practical cases, convective cooling is available at the radial surface at r = R, whereas the top and bottom ends are used primarily for electrical interconnection. Finally, since k_z has been measured to be much larger k_r [22], improvement in k_r is more beneficial for temperature reduction.

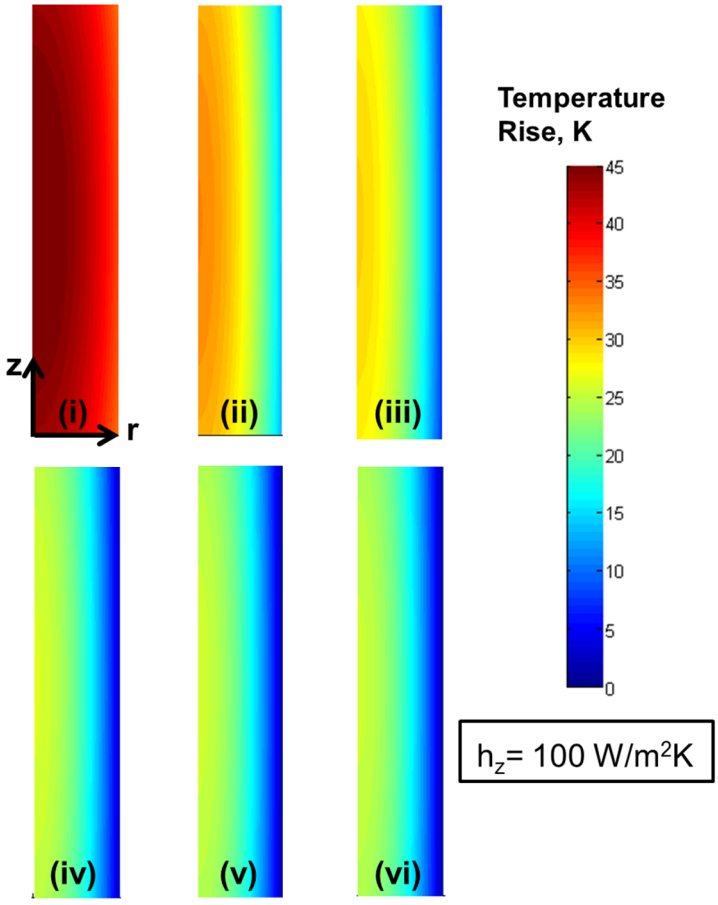

Figure 2.5. Variation of temperature field in a 26650 cell as a function of heat transfer coefficient for h_r=(i) 10 W/m^{2}K, (ii) 50 W/m^{2}K, (iii) 100 W/m^{2}K, (iv) 500 W/m^{2}K, (v) 1000 W/m^{2}K, (vi) 1500 W/m^{2}K.

Figure 2.5 shows 2D cross-section temperature color plots for various values of h_r. As the radial convective heat transfer coefficient increases, the cell temperature field reduces as expected. However, beyond approximately h_r = 1000 W/m^{2}K, there is negligible incremental improvement in the temperature profile. This is further illustrated in Figure 2.6(a) which shows temperature line plots as function of r at the cell's mid-height. These results show that improvement in the external convective heat transfer coefficient helps reduce cell temperature, but this effect quickly saturates. Beyond a specific value, there is not much further improvement. This illustrates the limitation of radial convective cooling mechanisms for cylindrical Li-ion cells. The fundamental reason behind this is that heat flow from within the cell to the ambient encounters two thermal resistances in series – one due to thermal conduction within the cell material, and the second due to convective heat transfer at the outside surface of the cell.

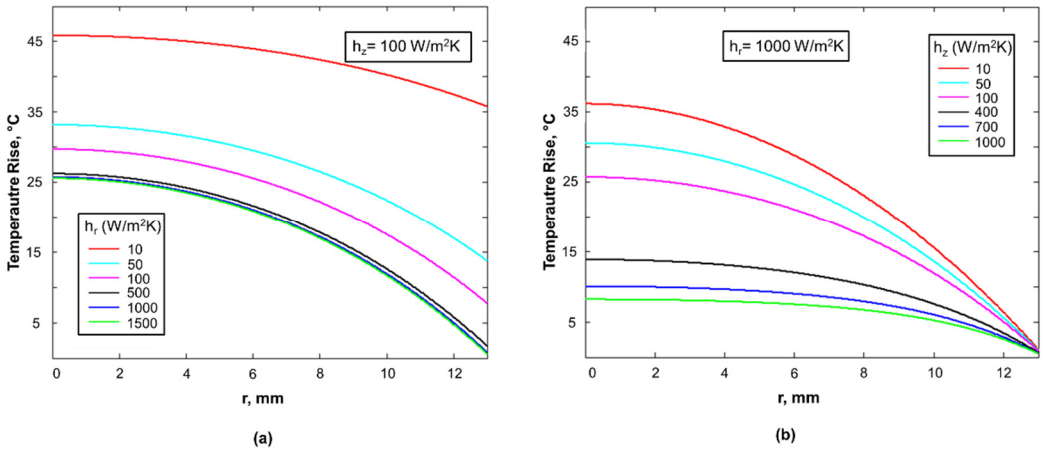

Figure 2.6. 1D Solution for temperature as a function of r at mid-height for various values of (a) h_r and (b) h_z.

In the radial direction, it is the conduction thermal resistance within the cell that is dominant, which is caused by a very low value of radial thermal conductivity [22].

As h_r increases, the convective heat transfer resistance rapidly becomes negligible compared to the conduction resistance, which dominates the thermal response of the cell.

When considering the axial-direction, Figure 2.6(b) shows the temperature profiles for different values of h_z. As h_z increases, the temperature profiles become lower and lower, and do not saturate similar to the radial case in Figure 2.6(a). These results indicate that there may be significant potential in cooling the Li-ion cells from the top and bottom surfaces despite the lower surface area because axial conduction within the cell is more effective than radial conduction. Convective heat transfer at the axial ends may be complicated by the presence of electrical connections. On the other hand, overall heat transfer in the radial direction also requires a close examination of the conduction resistance within the cell, which is shown to be the slower, rate-determining step in radial conduction. Improvements in convective heat transfer at the axial ends, and radial conduction within the cell may be effective technological tools for reducing operating temperature in Li-ion cells.

In addition to absolute temperature rise, temperature gradient within a cell is also of interest for thermal design of cells. It is desirable to minimize spatial variation in temperature within the cell. Temperature variation causes an electrochemical imbalance which may reduce cell lifetime and reliability. Figure 2.7 plots the intra-cell temperature gradient as a function of the radial convective heat transfer coefficient h_r. It is found that as h_r improves, the temperature gradient within the cell actually increases. This is because at higher

values of h_r, heat generation in the region close to the r = R surface gets dissipated more and more effectively, whereas heat generation in the core of the cell continues to see the internal thermal resistance, which remains unaffected by the improved value of h_r. This demonstrates that while increasing h_r may produce limited improvement in the absolute temperature rise, it may actually increase the intra-cell temperature gradient.

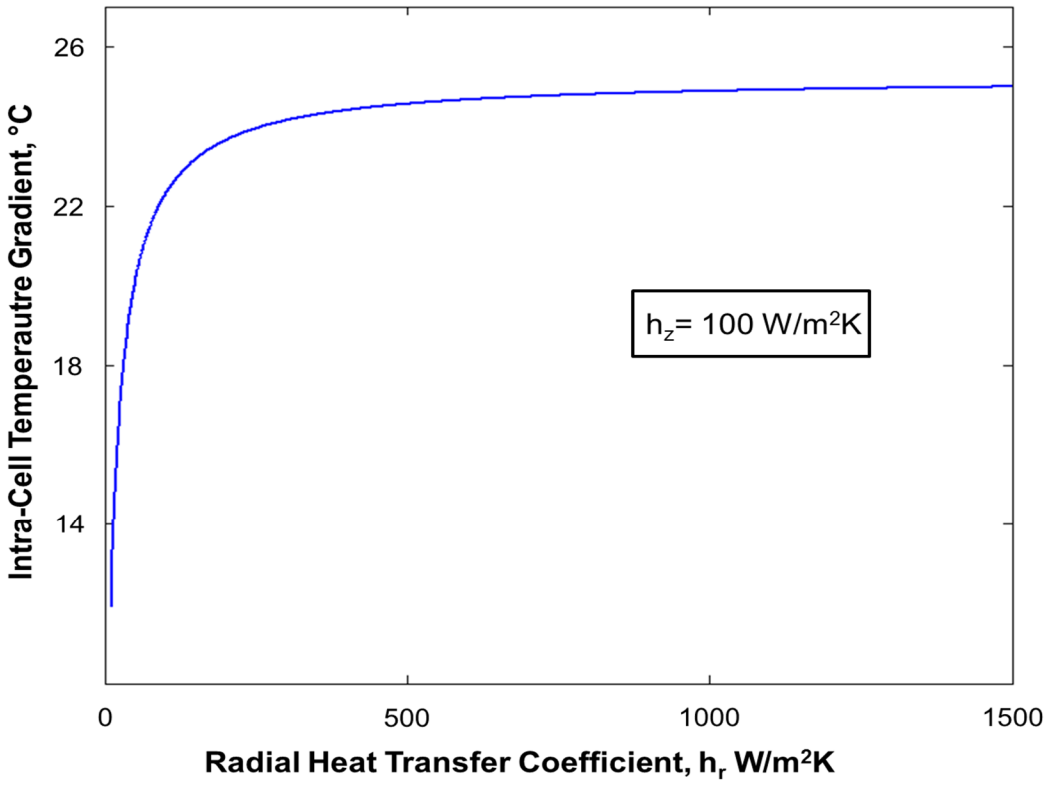

Figure 2.7. Effect of radial heat transfer coefficient on intra-cell temperature gradient

2.4.2 Battery sizing optimization

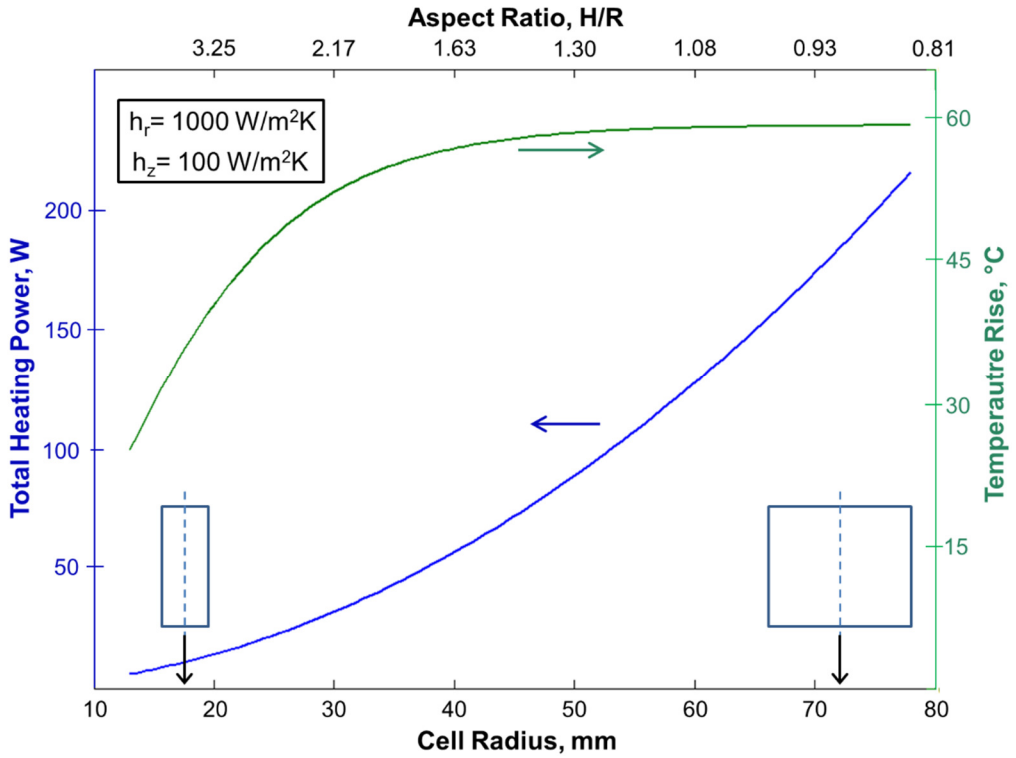

Figure 2.8: Effect of battery size on total power and maximum temperature rise, assuming constant power density

One application of the analytical models presented in previous Sections for battery sizing is presented next. Two particular design optimization problems are discussed. The first problem relates to trade-offs between cell power and temperature rise as functions of cell size. It is of interest to understand how the cell temperature changes as the cell size increases. Figure 2.8 plots the total power and temperature rise as functions of the cell radius, assuming that the cell height and other parameters remain constant. Figure 2.8 shows that as the cell radius increases and aspect ratio H/R decreases, the energy capacity of the cell increases in a

quadratic fashion. On the other hand, the peak temperature rise in the cell also increases, but the rate of increase with radius slows down after a certain radius. This is because assuming constant cell power density based on the packing density of the electrode material inside the cell, a larger cell has more storage capacity and hence greater total power. On the other hand, increased size also leads to greater heat generation, which causes greater temperature rise. The increase in temperature with increasing radius however is not as rapid particularly for larger cells because a larger cell has larger outer surface available for convective cooling. Figure 2.8 demonstrates the fundamental trade-off between power storage and thermal management. Increasing the cell size makes it more attractive from the power perspective, but also exacerbates the thermal management problem.

While Figure 2.8 examines the effect of increasing the cell size, it is also instructive to examine the dependence of peak temperature on the aspect ratio of the cell while maintaining the same total volume. In several applications, the cell volume is fixed due to system-level considerations, while it might be possible to change the aspect ratio within the fixed cell volume. The choice then is whether to have a thin and slender cell, or a short and stout cell. For constant total cell volume V and hence constant total power capacity, the radius and height are related to each other. For a given radius, the height is given by $H = \frac{V}{\pi R^2}$. If convective heat transfer is limited to only the r = R boundary, then assuming uniform heat generation in the cell, the temperature field is given by equation (15), which shows that the peak temperature at r = 0 increases as R increases. Thus in this case, it is thermally

preferable to have thin cells of high aspect ratio *H/R*. If on the other hand, convective heat transfer occurs at both $r = R$ and the top/bottom faces of the cell, then the peak temperature depends on *R* in a more complicated fashion.

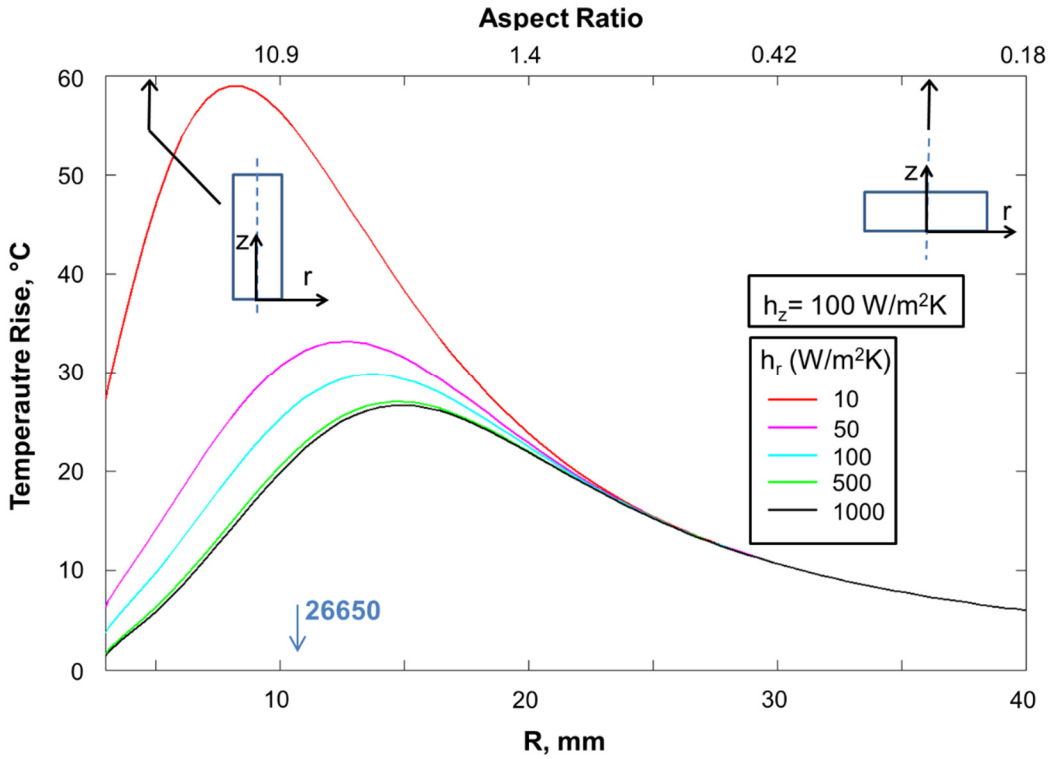

Figure 2.9: Variation of peak temperature rise as a function of cell radius for fixed total cell volume

Figure 2.9 plots peak temperature rise for this case as a function of *R* for fixed total volume, fixed h_z, and for different values of the radial convective heat transfer coefficient, h_r. The total fixed volume is assumed to be that of a 26650 cell. Figure 2.9 shows that there is a radius at which the temperature rise attains a maximum. This could be considered a worst-case radius, which roughly corresponds to the radius that minimizes the integral of heat transfer coefficient with respect to area over all surfaces. Note that the worst-case radius is a function of h_r and h_z, and that it becomes larger and larger as h_r increases over h_z.

Figure 2.9 shows the position of the 26650 cell on the x-axis, indicating the 26650 geometry is far from optimal particularly for low values of h_r. Reducing the radius of the 26650 cell while increasing height to maintain constant volume may be helpful in reducing the peak temperature rise, particularly when the convective heat transfer coefficient h_r is somewhat low.

CHAPTER 3

AN EXPERIMENTALLY VALIDATED TRANSIENT THERMAL MODEL FOR CYLINDRICAL LI-ION CELLS

Shah, K., Drake, S. J., Wetz, D. A., Ostanek, J. K., Miller, S. P., Heinzel, J. M., & Jain, A. (2014). An experimentally validated transient thermal model for cylindrical Li-ion cells. Journal of Power Sources, 271, 262-268.

Abstract

Measurement and modeling of thermal phenomena in Li-ion cells is a critical research challenge that directly affects performance and safety. Even though the operation of a Li-ion cell is in most cases a transient phenomenon, most available thermal models for Li-ion cells predict only steady-state temperature fields. This paper presents the derivation, experimental validation and application of an analytical model to predict the transient temperature field in a cylindrical Li-ion cell in response to time-varying heat generation within the cell. The derivation is based on Laplace transformation of governing energy equations, and accounts for anisotropic thermal conduction within the cell. Model predictions are in excellent agreement with experimental measurements on a thermal test cell. The effects of various thermophysical properties and parameters on transient thermal characteristics of the cell are analyzed. The effect of pulse width and cooling time for pulsed operation is quantified. The thermal response to multiple cycles of discharge and charge is computed, and cell-level trade-offs for this process are identified. The results presented in this paper may help understand thermal phenomena in Li-ion cells, and may contribute towards thermal design and optimization tools for energy conversion and storage systems based on Li-ion cells.

Keywords: Lithium-ion Cells, Energy Conversion, Transient Thermal Management, Battery Cooling, Laplace Transforms.

3.1 Analytical Model

Figure 3.1 shows a schematic of a heat-generating, cylindrical Lithium-ion cell of radius R and height H. Heat generation within the cell occurs due to a variety of physical mechanisms, including Joule heating, entropic heating, enthalpies of reactions, etc. [5,86]. The volumetric heat generation rate Q(t) is assumed to be uniform in space, but time-dependent. Convective heat transfer is assumed to occur on the outside surfaces, with heat transfer coefficients given by h_r and h_z for the

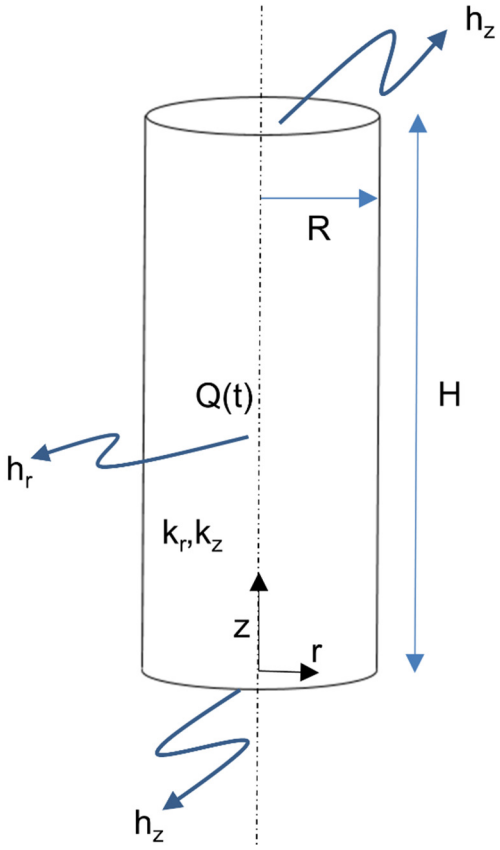

Figure 3.1. Schematic of the geometry of a cylindrical Li-ion cell under consideration.

radial and axial outer surfaces respectively. Thermal conductivity of the Li-ion cell is assumed to be anisotropic [14], with values of k_r and k_z in radial and axial directions respectively.

The transient temperature field for this problem is governed by the following energy conservation equation:

$$\frac{k_r}{r}\frac{\partial}{\partial r}\left(r\frac{\partial \theta}{\partial r}\right)+k_z\frac{\partial^2\theta}{\partial z^2}+Q(t)=\rho C_p\frac{\partial \theta}{\partial t} \tag{24}$$

where $\theta(r,z,t)$ is the temperature rise above ambient.

Equation (24) is a non-homogeneous, transient partial differential equation subject to four homogeneous boundary conditions given by

$$\frac{\partial \theta}{\partial z}=\frac{h_z}{k_z}\theta \qquad \text{at z = 0} \tag{25}$$

$$\frac{\partial \theta}{\partial z}=-\frac{h_z}{k_z}\theta \qquad \text{at z = H} \tag{26}$$

$$\frac{\partial \theta}{\partial r}=0 \qquad \text{at r = 0} \tag{27}$$

$$\frac{\partial \theta}{\partial z}=-\frac{h_r}{k_r}\theta \qquad \text{at r = R} \tag{28}$$

In addition, it is assumed that the cell is at ambient temperature at t=0

$$\theta=0 \qquad \text{at t = 0} \tag{29}$$

Deriving an analytical expression for equation (24) subject to boundary conditions (25)-(28), and initial condition (29) is not straightforward due to the time-dependence of the heat generation term. To do so, Laplace transform of equations

(24)-(28) is carried out, resulting in the following governing equation in the Laplace space:

$$\frac{k_r}{r}\frac{\partial}{\partial r}\left(r\frac{\partial \bar{\theta}}{\partial r}\right)+k_z\frac{\partial^2 \bar{\theta}}{\partial z^2}+\bar{Q}(s)=\frac{\rho C_p}{s}\bar{\theta} \tag{30}$$

subject to

$$\frac{\partial \bar{\theta}}{\partial z}=\frac{h_z}{k_z}\bar{\theta} \qquad \text{at z = 0} \tag{31}$$

$$\frac{\partial \bar{\theta}}{\partial z}=-\frac{h_z}{k_z}\bar{\theta} \qquad \text{at z = H} \tag{32}$$

$$\frac{\partial \bar{\theta}}{\partial r}=0 \qquad \text{at r = 0} \tag{33}$$

$$\frac{\partial \bar{\theta}}{\partial r}=-\frac{h_r}{k_r}\bar{\theta} \qquad \text{at r = R} \tag{34}$$

where $\bar{\theta}(r,z)$ and $\bar{Q}(s)$ are Laplace transforms of the temperature rise field $\theta(r,z,t)$ and heat generation term $Q(t)$ respectively. s is the Laplace variable.

The final solution is found to be

$$\bar{\theta}(r,z)=\bar{p}(z)+\sum_{n=1}^{\infty}c_n I_0(\lambda_n r)\left[\mu_n H Cos(\mu_n z)+Bi_H Sin(\mu_n z)\right] \tag{35}$$

where,

$$\overline{p}(z) = A \cdot Sinh\left(\sqrt{\frac{\rho C_p s}{k_z}} z\right) + B \cdot Cosh\left(\sqrt{\frac{\rho C_p s}{k_z}} z\right) \tag{36}$$

The coefficients A and B in equation (36) are determined by using boundary conditions in the z-direction, which results in

$$A = \frac{\frac{\overline{Q}(s)}{\rho C_p s}\left(\sqrt{\rho C_p s k_z}\, Sinh\left(\sqrt{\frac{\rho C_p s}{k_z}} H\right) + h_z\left(Cosh\left(\sqrt{\frac{\rho C_p s}{k_z}} H\right) - 1\right)\right)}{2\sqrt{\rho C_p s k_z}\, Cosh\left(\sqrt{\frac{\rho C_p s}{k_z}} H\right) + h_z Sinh\left(\sqrt{\frac{\rho C_p s}{k_z}} H\right) + \frac{\rho C_p s k_z}{h_z} Sinh\left(\sqrt{\frac{\rho C_p s}{k_z}} H\right)} \tag{37}$$

$$B = \frac{A\sqrt{\rho C_p s k_z}}{h_z} - \frac{\overline{Q}(s)}{\rho C_p s} \tag{38}$$

Note that the series coefficients c_n in equation (35) are given by

$$c_n = \frac{-Bi_R \cdot \frac{1}{H}\int_0^H \overline{p}(z)\left[\mu_n H Cos(\mu_n z) + Bi_H Sin(\mu_n z)\right] dz}{\frac{1}{2}\left[(\mu_n H)^2 + Bi_H{}^2 + 2Bi_H\right] \cdot \left[\lambda_n R \cdot I_o'(\lambda_n R) + Bi_R I_o(\lambda_n R)\right]} \tag{39}$$

The eigenvalues μ_n are obtained from roots of the transcendental equation

$$Tan(\mu H) = \frac{2Bi_H \cdot (\mu H)}{(\mu H)^2 - Bi_H{}^2} \tag{40}$$

where Bi_H and Bi_R are axial and radial Biot numbers, respectively, defined as $Bi_H = \frac{h_z H}{k_z}$ and $Bi_R = \frac{h_r R}{k_r}$.

Finally,

$$\lambda_n = \sqrt{\gamma\left(\frac{\rho C_p s}{k_z} + \mu_n^{\,2}\right)} \tag{41}$$

where γ is the degree of anisotropy given by

$$\gamma = \frac{k_z}{k_r} \tag{42}$$

Equations (35)-(42) represent an analytical solution for the temperature field in the Laplace space. Since the resulting expression is somewhat complicated, conversion into time domain is carried out using de Hoog's quotient difference algorithm [87] for inverse Laplace transformation, as implemented by Hollenbeck [88].

While the solution methodology described above is applicable for spatially-uniform heat generation rate, a different approach needs to be adopted if, in addition to time, heat generation rate is a function of space as well. This could be done similar to a recently reported approach for solving the corresponding steady state problem with space dependent heat generation [35].

3.2 Experimental Validation

A thermal test cell is utilized for experimentally validating the thermal model discussed in section 1. This thermal test cell has the same dimensions as a 26650 cell, and has a thin stainless steel resistive heater rolled inside the cell body. The test cell is placed in a chamber without forced air flow, representative of natural convection conditions. A K-type thermocouple attached to the outside surface of the test cell at mid-height provides temperature measurements as a function of time, which is compared against computations based on the model shown in Section 3.1.

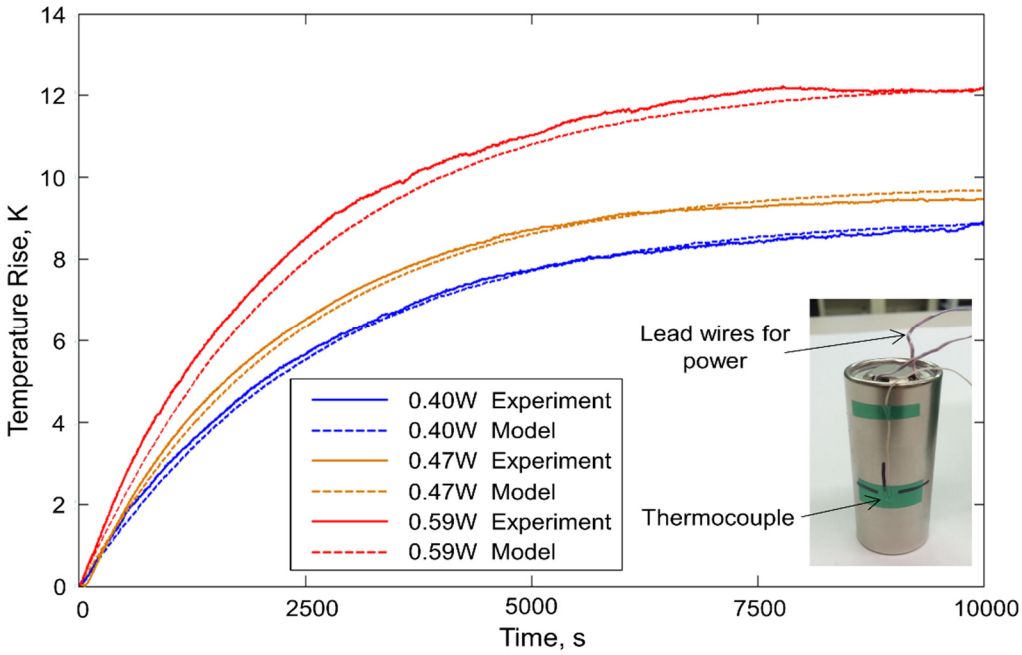

Figure 3.2. Temperature plot showing experimental validation of the analytical model.

A picture of the thermal test cell with the thermocouple and lead wires for the heater is shown in the inset of Figure 3.2. A Keithley 2401 sourcemeter is used to source the heating current, and a NI 9213 DAQ is used for temperature acquisition. All instruments are controlled by a LabVIEW code, which regularly

makes minor adjustments to the heating current in order to provide constant power. This accounts for any increase in resistance of the heater due to increased temperature inside the cell.

The analytical model in Section 3.1 is used to predict the temperature as a function of time for the experimental conditions. Thermal properties of the same test cell used in experiments are implemented in the model. These properties – radial and axial thermal conductivities and heat capacity – are determined by using a recently described experimental technique [22]. The measured values for the test cell are found to be close to recently reported values for an actual 26650 cell. The convective heat transfer coefficients h_r and h_z are assumed to be 10 W/m^{2}K, which is representative of natural convection cooling [41]. Figure 2.2 presents the measured temperature rise at the outer surface at mid-height (r=R, z=H/2) as a function of time for three different heat generation rates. The temperature variation predicted by the analytical model presented in Section 3.1 is also shown in Figure 3.2. In each case, the analytical model is in excellent agreement with experimental data. The model correctly captures both absolute temperature rise and the time scale for the temperature rise for each power. The maximum deviation between the two during the entire experiment is 0.63 °C.

3.3 Results and Discussion

For further confirmation of the validity and accuracy of the analytical model derived in section 1, the temperature field is computed as a function of time for two cases, and compared with results from finite-element simulations. These cases address the temperature response of a 26650 Li-ion cell to two different heating

profiles – a constant heating of 6 W, and a step function where the heating power spikes from 2 W to 10 W between t=1000s and t=1500s.

Note that the heat generation rate is closely related to the C-rate through the discharge current and effective internal resistance of the cell as follows:

$$Q = I^2 \cdot r_{\text{int}} \tag{43}$$

Thus, assuming a 2.6 A-hr cell with an effective internal resistance of 20 mΩ, the 6 W heating case corresponds to a C-rate of 6.7C and the 2-10 W range corresponds to a C-rate range of 3.8-8.6C.

Figures 3.3(a) and 3.3(b) plot the temperature profile computed for these cases using the analytical model, along with results from finite-element simulations. Adequately fine meshing is carried out in these simulations to ensure grid-independence of results. In both cases, there is excellent agreement between the analytical model and results from finite-element simulations, which provides additional validation of the analytical model presented in section 3.1.

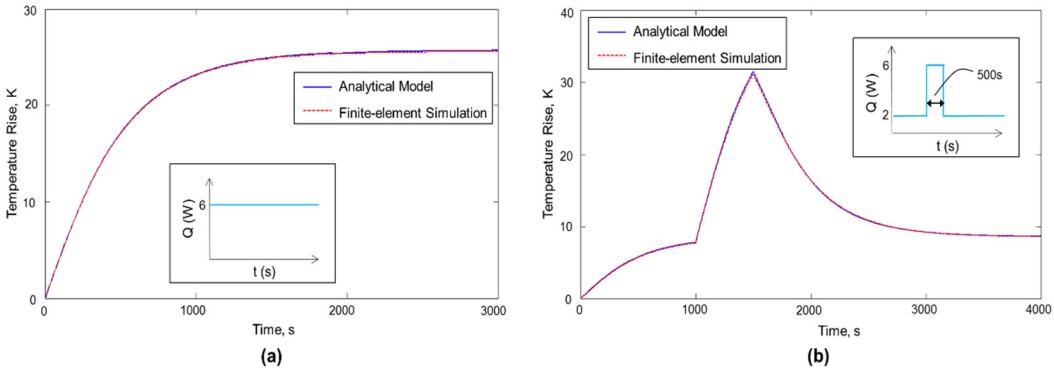

Figure 3.3. Comparison of analytical model with finite-element simulations (a) Constant, and (b) Pulsed heat generation profiles.

Since the external heat transfer coefficient h_r and radial thermal conductivity k_r are key parameters that determine thermal performance of the Li-ion cell, temperature is computed as a function of time for different values of these parameters, while considering the same heat generation rate. These plots, presented in Figure 3.4(a) and 3.4(b) show that the temperature profile and the peak temperature are strong functions of both h_r and k_r. The cell temperature reduces as h_r increases, since greater convective heat transfer on the cell surface reduces heat accumulated within the cell, and hence the cell temperature.

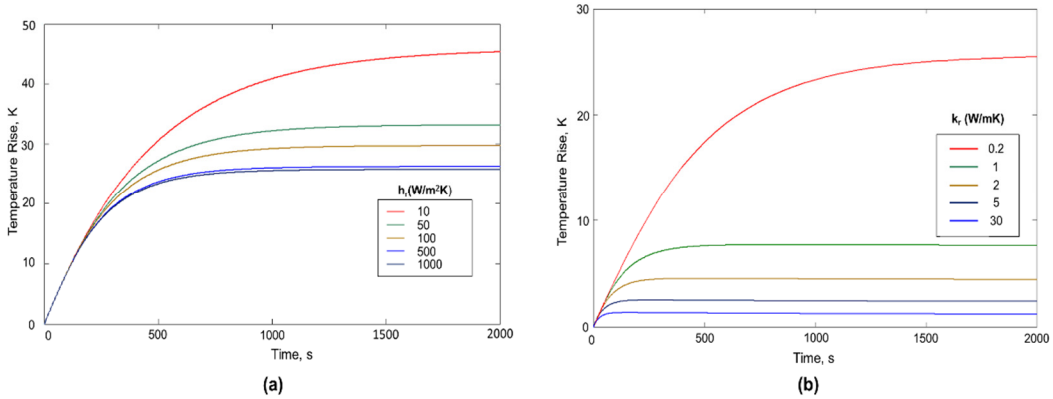

Figure 3.4. Plots showing variation in temperature profiles as function of (a) Convective heat transfer coefficient, h_r, (b) Radial thermal conductivity, k_r.

However, the effect of increasing h_r on lowering the cell temperature saturates, as seen in Figure 3.4(a). Increasing the value of h_r beyond around 500 W/m^2K has negligible incremental effect on reducing the cell temperature. This can be explained in terms of the overall thermal resistance comprising of the thermal conduction resistance within the cell, and convective resistance from the cell surface to the ambient. Once the latter resistance has been reduced sufficiently, it does not dominate any more, and the cell temperature becomes nearly independent of the convective thermal resistance. On the other hand, increasing the value of k_r,, which contributes towards reducing the internal conduction resistance, is found to

strongly reduce the cell temperature, as shown in Figure 3.4(b). No saturation effect similar to Figure 3.4(a) is observed in this case. The temperature curve continues to drop with increasing k_r. Note that the largest value of k_r examined in Figure 3.4(b) is 30 W/mK, which is the experimentally measured axial thermal conductivity [22], and hence likely to be the upper limit of k_r.

The analytical model is also used to investigate the thermal effects of transient spikes in heat generation rate during the operation of a Li-ion cell. It is assumed that the Li-ion cell encounters a pulse of excess load resulting in a 13.5 W heat generation, corresponding to 10C discharge rate. This is followed by zero heat generation rate. Such a pulse can occur, for example, during sudden acceleration of a hybrid/electric vehicle that demands large power draw from the battery for a short amount of time [89]. It is clearly of much importance to understand the thermal phenomena associated with such a power draw, particularly the peak temperature

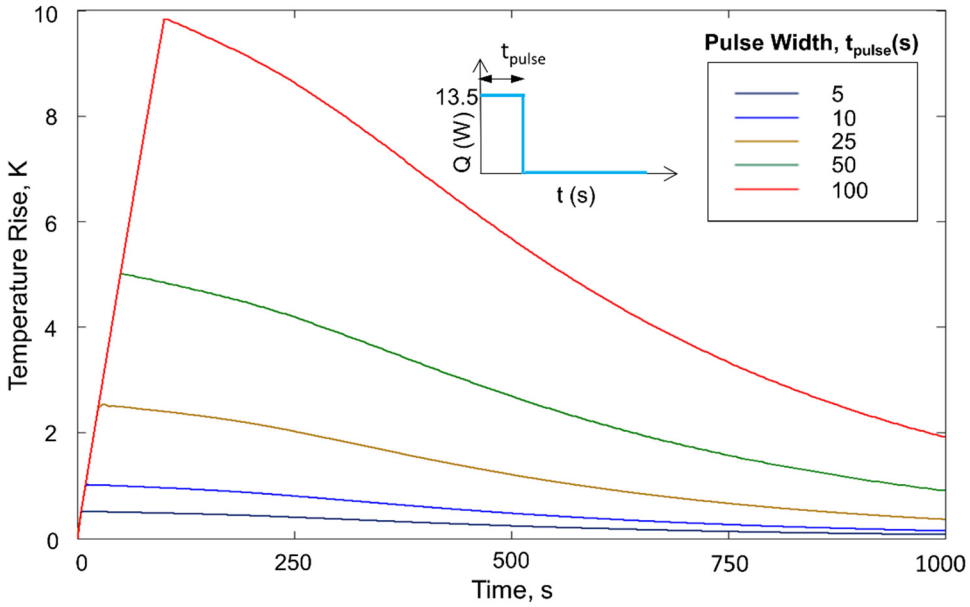

Figure 3.5. Plot of the maximum cell temperature as a function of time for different pulse widths.

reached by the cell, and the time taken by the cell to recover to baseline temperature.

Figure 3.5 presents plots of the cell temperature as a function of time for different pulse widths in the 2.5-30s range, which may be typical for vehicular applications [89]. h_r and h_z are assumed to be 100 W/m^{2}K each, and kr and kz are assumed to be 0.2 and 30 W/mK respectively, based on measurements [14].

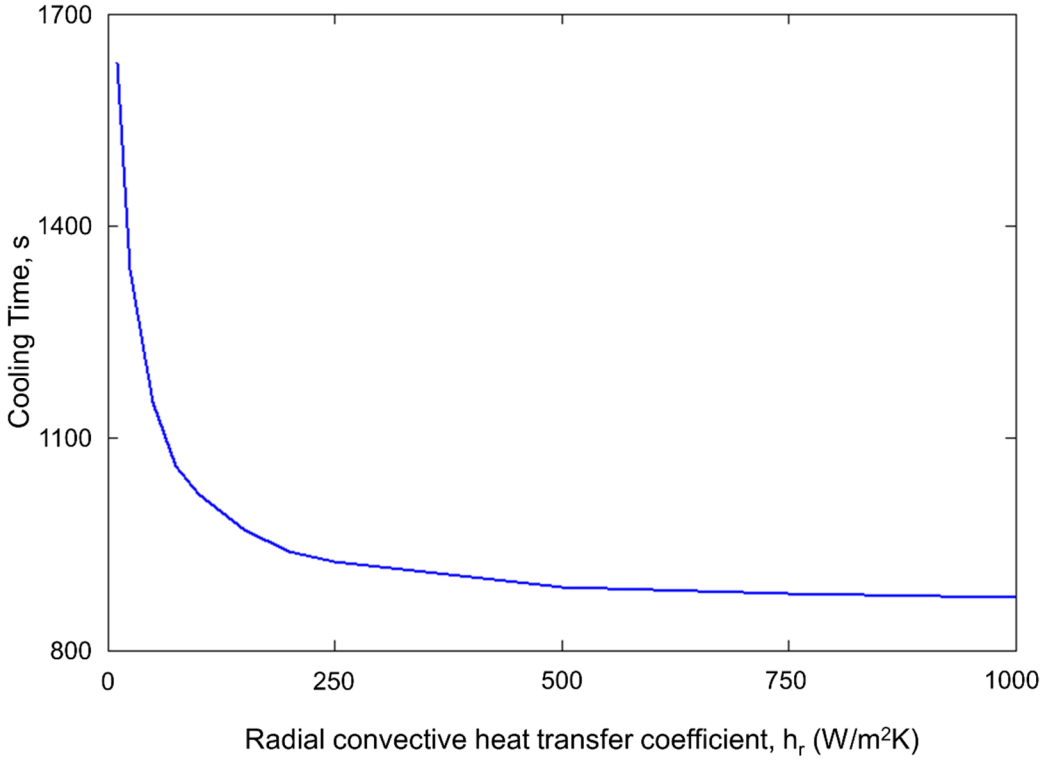

Figure 3.6. Plot of cooling time required to cool down to a baseline temperature of 1 °C above ambient as a function of the convective heat transfer coefficient hr.

Figure 3.5 shows that as the pulse width increases, the cell temperature increases as expected. The time taken to cool down back to a specific temperature also increases as the pulse width increases. One possible strategy for timely cooling is to increase convective heat transfer during the cooling process, for example by blowing more air or coolant, which effectively increases the value of h_r. Figure 3.6

plots the time required by the cell to cool down to a temperature of 1 °C above baseline temperature after a 50s pulse of 13.5 W as a function of the convective heat transfer coefficient h_r. In general, the time required to cool reduces as h_r increases. However, this effect saturates, similar to the saturation observed in Figure 3.4(a), wherein beyond around 500 W/m^{2}K, increasing h_r further results in only minimal improvement in time needed to cool. As shown in Figure 3.4(b), further improvements in the thermal performance of the Li-ion cell must come from improved thermal conductance within the cell due to dominance of the internal conduction resistance in the overall thermal resistance.

Another pulsed power scenario with interesting and technologically relevant thermal concerns is the discharge of a given energy in a pulse. In case the cell is to discharge a specific amount of energy, there may be a fundamental choice in whether to discharge the energy at high power over a short time, or at low power over a large time. While the former choice increases the power dissipated in the cell, there is more time in the latter for the cell temperature to rise. This problem is examined using the analytical model presented in section 3.1.

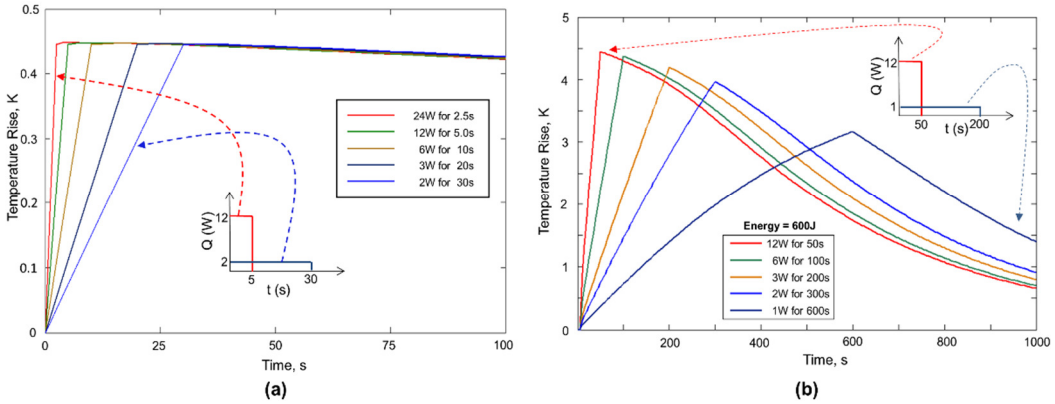

Figure 3.7. Temperature profile for various discharge rates dissipating a constant total energy for (a) short pulse duration, and (b) long pulse duration.

In particular, the maximum cell temperature is plotted in Figures 3.7 (a) and 3.7(b) as a function of time for a number of discharges that each dissipate a fixed amount of energy, but at different powers and discharge times. Figure 3.7(a) addresses relatively shorter pulse widths, with total 60 J energy dissipation, while Figure 3.7(b) addresses longer pulse widths, with total 600 J dissipation. h_r, h_z, k_r and k_z are assumed to be the same as in Figure 3.5. Figure 3.7(a) shows that at low pulse widths, the peak temperature reached is not a strong function of pulse width. On the other hand, for larger pulse durations, as shown in Figure 3.7(b), the cell temperature increases with decreasing discharge time due to increased power. Thus, it may be preferable to discharge over a longer time with lower power, although this effect is not significant in the short pulse width range.

Several energy conversion applications may require multiple periodic discharges – each of which results in heat generation – from the Li-ion cell, with a cooling time interspersed between successive discharges. Such successive discharges may cause heat buildup within the cell and excessive temperature rise, possibly leading to thermal runaway. As a result, thermal analysis of a multiple discharge process is of critical importance. The model presented in section 1 is utilized to compute the temperature as a function of time for a 10-step process of successive discharges. Each discharge is assumed to result in 6W heat generation over a 10 second period.

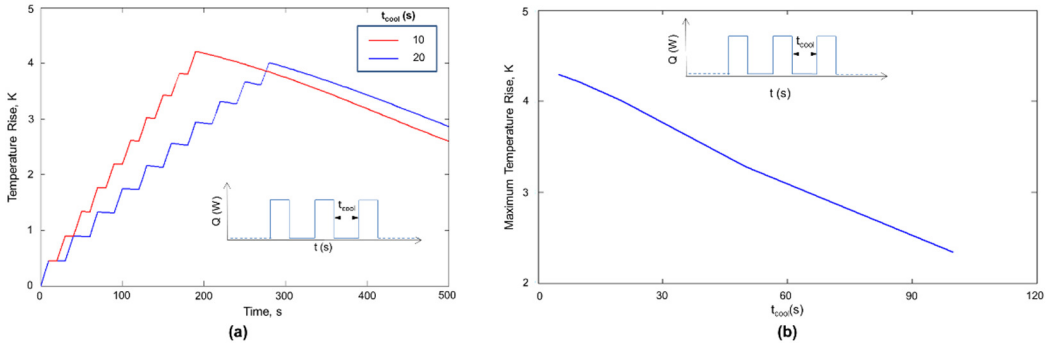

Figure 3.8. (a) Comparison of temperature profile for two different ten-step discharge-charge processes with cooling times of 10s and 20s, (b) Plot showing dependence of maximum temperature rise on cooling time.

Figure 3.8(a) presents the resulting temperature curves for two cooling times of 10 and 20 s. The cooling time is a critical parameter in the thermal well-being of the cell during the multiple discharge process. Figure 3.8(b) plots the peak temperature rise at the end of the ten-cycle process as a function of cooling time between successive discharges. A large cooling time permits the cell to recover between discharges, whereas heat buildup may occur within the cell if the cooling time is too small. Increasing the cooling time – which is clearly thermally beneficial – however, is in conflict with possible system-level goals of reducing total energy conversion time. A careful balance between conflicting objectives, driven by analytical models such as ones presented here may be the key for safe and optimal operation of Li-ion cell based energy conversion systems.

CHAPTER 4

MODELING OF STEADY-STATE AND TRANSIENT THERMAL PERFORMANCE OF A LI-ION CELL WITH AN AXIAL FLUIDIC CHANNEL FOR COOLING

Shah, K., & Jain, A. (2015). Modeling of steady-state and transient thermal performance of a Li-ion cell with an axial fluidic channel for cooling. International Journal of Energy Research, 39(4), 573-584.

Abstract

Thermal management of Li-ion cells is an important technological problem for energy conversion and storage. Effective dissipation of heat generated during the operation of a Li-ion cell is critical to ensure safety and performance. In this paper, thermal performance of a cylindrical Li-ion cell with an axial channel for coolant flow is analyzed. Analytical expressions are derived for steady-state and transient temperature fields in the cell. The analytical models are in excellent agreement with finite-element simulation results. The dependence of the temperature field on various geometrical and thermal characteristics of the cell is analyzed. It is shown that coolant flow through even a very small diameter axial channel results in significant thermal benefit. The trade-off between thermal benefit and reduction in cell volume, and hence capacity due to the axial channel is analyzed. The effect of axial cooling on geometrical design of the cell, and transient thermal performance during a discharge process is also analyzed. Results presented in this paper are expected to aid in the development of effective cooling techniques for Li-ion cells based on axial cooling.

Keywords: Lithium-Ion Cells, Battery Cooling, Battery Safety, Thermal Modeling.

4.1 Analytical Model

Consider an annular Li-ion cell with height H, and outer and inner radii R_o and R_i respectively, shown schematically in Figure 4.1. The cell is assumed to dissipate a constant volumetric heat generation Q, which is dependent on the C-rate of the cell. The radial and axial thermal conductivities of the cell are assumed to be k_r and k_z

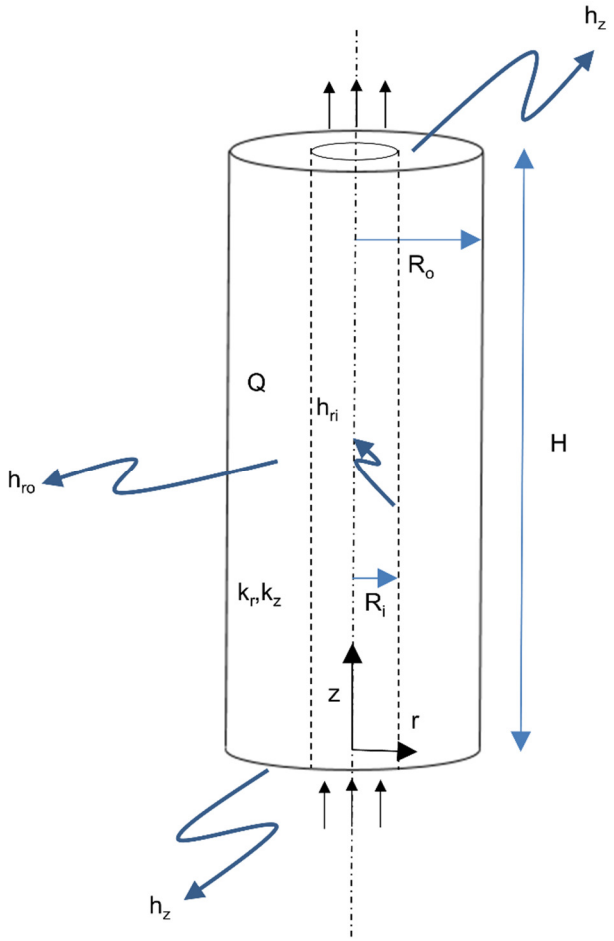

Figure 4.1. Schematic of geometry of the annular cell.

respectively. Assumption of anisotropic thermal conductivity is necessary based on recent measurements that show significant difference in radial and axial thermal conductivities [14].

For a general case, convective heat transfer coefficients h_{ro} and h_z are assumed at the outer surfaces in the radial (r=*R*) and axial directions (z=0, z=*H*) respectively. Setting any of these to zero makes these boundary conditions adiabatic. A constant temperature boundary condition, which is easier to model, but less realistic than convective heat transfer boundary conditions can also be analyzed using methods similar to one discussed here. Coolant flow through the axial channel is modeled using a convective heat transfer coefficient h_{ri} along the inner wall. Note that the convective heat transfer coefficients listed above are all assumed to be surface-averaged values over the respective surfaces. This significantly simplifies the analysis. Expressions for the steady-state and transient temperature distributions in the cell are derived in the following sub-sections.

4.1.1. Steady State Temperature Distribution

The governing steady state energy conservation equation for the annular cell is given by [66-67]

$$\frac{k_r}{r}\frac{\partial}{\partial r}\left(r\frac{\partial T}{\partial r}\right)+k_z\frac{\partial^2 T}{\partial z^2}+Q=0 \tag{44}$$

where *T(r,z)* is the temperature rise above ambient.

The governing equation is subject to the following boundary conditions [50]:

$$\frac{\partial T}{\partial z} = \frac{h_z}{k_z} T \qquad \text{at z = 0} \qquad (45)$$

$$\frac{\partial T}{\partial z} = -\frac{h_z}{k_z} T \qquad \text{at z = } H \qquad (46)$$

$$\frac{\partial T}{\partial r} = \frac{h_{ri}}{k_r} (T - T_{cool}) \qquad \text{at r = } R_i \qquad (47)$$

$$\frac{\partial T}{\partial r} = -\frac{h_{ro}}{k_r} T \qquad \text{at r = } R_o \qquad (48)$$

Where T_{cool} is the temperature of the coolant with respect to ambient temperature. For a coolant entering at the same temperature as ambient, T_{cool}=0.

The temperature distribution is

$$T(r,z) = s(z) + w(r,z) \qquad (49)$$

The two components of the temperature distribution are given by

$$s(z) = \frac{QH^2}{2k_z}\left[\frac{z}{H}\left(1 - \frac{z}{H}\right) + \frac{1}{Bi_H}\right] \qquad (50)$$

and

$$w(r,z)=\sum_{n=1}^{\infty}\left[\left(A_n+B_n\right)\cdot I_0(\lambda_n r)+\left(A_n\beta_1+B_n\beta_2\right)\cdot K_0(\lambda_n r)\right]\cdot\left[\mu_n HCos(\mu_n z)+Bi_H Sin(\mu_n z)\right] \tag{51}$$

The coefficients A_n and B_n in equation (8) are given by

$$A_n=\frac{-h_{ro}\int_0^H s(z)\left[\mu_n Cos(\mu_n z)+(h_z/k_z)Sin(\mu_n z)\right]dz}{\frac{1}{2}\left[(\mu_n H)^2+Bi_H{}^2+2Bi_H\right]\cdot\left[h_{ro}I_o(\lambda_n R_o)+k_r\lambda_n I_1(\lambda_n R_o)+\beta_1\left(h_{ro}K_o(\lambda_n R_o)-k_r\lambda_n K_1(\lambda_n R_o)\right)\right]} \tag{52}$$

$$B_n=\frac{-h_{ri}\int_0^H (s(z)-T_{cool})\left[\mu_n Cos(\mu_n z)+(h_z/k_z)Sin(\mu_n z)\right]dz}{\frac{1}{2}\left[(\mu_n H)^2+Bi_H{}^2+2Bi_H\right]\cdot\left[h_{ri}I_o(\lambda_n R_i)-k_r\lambda_n I_1(\lambda_n R_i)+\beta_2\left(h_{ri}K_o(\lambda_n R_i)+k_r\lambda_n K_1(\lambda_n R_i)\right)\right]} \tag{53}$$

where

$$\beta_1=\frac{k_r\lambda_n I_1(\lambda_n R_i)-h_{ri}I_o(\lambda_n R_i)}{k_r\lambda_n K_1(\lambda_n R_i)+h_{ri}K_o(\lambda_n R_i)} \tag{54}$$

$$\beta_2=\frac{k_r\lambda_n I_1(\lambda_n R_o)+h_{ro}I_o(\lambda_n R_o)}{k_r\lambda_n K_1(\lambda_n R_o)-h_{ro}K_o(\lambda_n R_o)} \tag{55}$$

The eigenvalues μ_n are obtained from roots of the transcendental equation

$$Tan(\mu H) = \frac{2Bi_H \cdot (\mu H)}{(\mu H)^2 - Bi_H{}^2} \tag{56}$$

where Bi_H is the axial Biot number, defined as $Bi_H = \frac{h_z H}{k_z}$.

Finally,

$$\lambda_n = \sqrt{\gamma} \cdot \mu_n \tag{57}$$

where γ is the degree of anisotropy given by

$$\gamma = \frac{k_z}{k_r} \tag{58}$$

Equations (49)-(58) represent the solution for the steady-state temperature distribution in the cell.

4.1.2. Transient Temperature Distribution

The modeling of transient thermal characteristics of the annular cell is important for understanding time-dependent phenomena such as pulsed power operation, periodic or one-time spike in heat generation rate, etc. In order to account for such phenomena, the heat generation term must be considered to be time-dependent. The modeling of transient temperature distribution presents additional challenges

compared to steady state modeling. The transient governing energy equation is given by

$$\frac{k_r}{r}\frac{\partial}{\partial r}\left(r\frac{\partial T}{\partial r}\right)+k_z\frac{\partial^2 T}{\partial z^2}+Q(t)=\rho C_p\frac{\partial T}{\partial t} \tag{59}$$

Where $T(r,z,t)$ is the temperature rise above ambient.

The boundary conditions associated with equation (59) are the same as for the steady state problem, equations (45-48) discussed in the previous section. In addition, it is assumed that the cell is at ambient temperature at t=0, i.e. T=0 at t=0.

The primary difficulty in solving the transient problem arises from the heat generation term, which is a general time-dependent function. The first step towards deriving a solution for this general case is to carry out a Laplace transform of the governing energy equation and associated boundary conditions. This results in a set of partial differential equations in the Laplace space, given by

$$\frac{k_r}{r}\frac{\partial}{\partial r}\left(r\frac{\partial \overline{T}}{\partial r}\right)+k_z\frac{\partial^2 \overline{T}}{\partial z^2}+\overline{Q}(s)=\frac{\rho C_p}{s}\overline{T} \tag{60}$$

subject to

$$\frac{\partial \overline{T}}{\partial z}=\frac{h_z}{k_z}\overline{T} \qquad \text{at z=0} \tag{61}$$

$$\frac{\partial \overline{T}}{\partial z} = -\frac{h_z}{k_z}\overline{T} \qquad \text{at z=}H \qquad (62)$$

$$\frac{\partial \overline{T}}{\partial r} = \frac{h_{ri}}{k_r}\overline{T} \qquad \text{at r=}R_i \qquad (63)$$

$$\frac{\partial \overline{T}}{\partial r} = -\frac{h_{ro}}{k_r}\overline{T} \qquad \text{at r=}R_o \qquad (64)$$

$\overline{T}(r,z)$ and $\overline{Q}(s)$ are Laplace transforms of *T(r,z,t)* and *Q(t)* respectively. Given a certain heat generation function *Q(t)*, the function $\overline{Q}(s)$ can be easily computed.

The final solution is found to be

$$\overline{T}(r,z) = \overline{p}(z) + \overline{w}(r,z) \qquad (65)$$

The first part of the solution, $\overline{p}(z)$ is given by

$$\overline{p}(z) = \overline{C}\,Sinh\left(\sqrt{\frac{\rho C_p s}{k_z}}z\right) + \overline{D}\,Cosh\left(\sqrt{\frac{\rho C_p s}{k_z}}z\right) \qquad (66)$$

The coefficients $\overline{C}$ and $\overline{D}$ in equation (66) are determined by using boundary conditions in the z-direction, which results in

$$\overline{C} = \frac{\frac{\overline{Q}(s)}{\rho C_p s}\left(\sqrt{\rho C_p s k_z}\,Sinh\left(\sqrt{\frac{\rho C_p s}{k_z}}H\right) + h_z\left(Cosh\left(\sqrt{\frac{\rho C_p s}{k_z}}H\right) - 1\right)\right)}{\sqrt{\rho C_p s k_z}\,Cosh\left(\sqrt{\frac{\rho C_p s}{k_z}}H\right) + h_z Sinh\left(\sqrt{\frac{\rho C_p s}{k_z}}H\right) + \frac{\rho C_p s k_z}{h_z}Sinh\left(\sqrt{\frac{\rho C_p s}{k_z}}H\right) + \sqrt{\rho C_p s k_z}\,Cosh\left(\sqrt{\frac{\rho C_p s}{k_z}}H\right)} \quad (67)$$

$$\overline{D} = \frac{\overline{C}\sqrt{\rho C_p s k_z}}{h_z} - \frac{\overline{Q}(s)}{\rho C_p s} \quad (68)$$

The second part of the solution, $\overline{w}(r,z)$ is found to be

$$\overline{\mathrm{w}}(\mathrm{r},\mathrm{z}) = \sum_{\mathrm{n}=1}^{\infty}\left[\left(\overline{\mathrm{A}}_{\mathrm{n}} + \overline{\mathrm{B}}_{\mathrm{n}}\right)\cdot \mathrm{I}_0(\lambda_{\mathrm{n}}\mathrm{r}) + \left(\overline{\mathrm{A}}_{\mathrm{n}}\overline{\beta}_1 + \overline{\mathrm{B}}_{\mathrm{n}}\overline{\beta}_2\right)\cdot \mathrm{K}_0(\lambda_{\mathrm{n}}\mathrm{r})\right]\cdot\left[\mu_{\mathrm{n}}\mathrm{HCos}(\mu_{\mathrm{n}}\mathrm{z}) + \mathrm{Bi}_{\mathrm{H}}\mathrm{Sin}(\mu_{\mathrm{n}}\mathrm{z})\right] \quad (69)$$

where,

$$\overline{A}_n = \frac{-h_{ro}\int_0^H \overline{p}(z)\cdot\left[\mu_n Cos(\mu_n z) + (h_z/k_z)Sin(\mu_n z)\right]dz}{\frac{1}{2}\left[(\mu_n H)^2 + Bi_H{}^2 + 2Bi_H\right]\cdot\left[h_{ro}I_o(\lambda_n R_o) + k_r\lambda_n I_1(\lambda_n R_o) + \overline{\beta}_1\left(h_{ro}K_o(\lambda_n R_o) - k_r\lambda_n K_1(\lambda_n R_o)\right)\right]} \quad (70)$$

$$\overline{B}_n = \frac{-h_{ri}\int_0^H \overline{p}(z)\cdot\left[\mu_n Cos(\mu_n z) + (h_z/k_z)Sin(\mu_n z)\right]dz}{\frac{1}{2}\left[(\mu_n H)^2 + Bi_H{}^2 + 2Bi_H\right]\cdot\left[h_{ri}I_o(\lambda_n R_i) - k_r\lambda_n I_1(\lambda_n R_i) + \overline{\beta}_2\left(h_{ri}K_o(\lambda_n R_i) + k_r\lambda_n K_1(\lambda_n R_i)\right)\right]} \quad (71)$$

where,

$$\overline{\beta}_1 = \frac{k_r\lambda_n I_1(\lambda_n R_i) - h_{ri}I_o(\lambda_n R_i)}{k_r\lambda_n K_1(\lambda_n R_i) + h_{ri}K_o(\lambda_n R_i)} \quad (72)$$

$$\overline{\beta}_2 = \frac{k_r \lambda_n I_1(\lambda_n R_o) + h_{ro} I_o(\lambda_n R_o)}{k_r \lambda_n K_1(\lambda_n R_o) - h_{ro} K_o(\lambda_n R_o)} \tag{73}$$

The eigenvalues μ_n are the same as eigenvalues for the steady state problem, given by equation (56). Finally,

$$\overline{\lambda}_n = \sqrt{\gamma\left(\frac{\rho C_p s}{k_z} + \mu_n^2\right)} \tag{74}$$

Equations (65)-(74) represent the solution for $\overline{T}(r,z)$, from where, the temperature distribution T(r,z,t) can be obtained from inverse Laplace transform. In case the Laplace transform is too difficult to invert explicitly, a numerical inversion technique is adopted using de Hoog's quotient difference method algorithm [87] for inverse Laplace transformation, as implemented by Hollenbeck [88].

4.1.3. Extension to space-dependent heat generation

The analytical derivations presented in sections 4.1.1 and 4.1.2 assumed uniform heat generation rate in the entire volume of the cell. While this is usually assumed to be the case, in general, the heat generation rate may vary with space, for example, if a short circuit causes high heat generation in a specific part of the cell. In such a case, an approach similar to one recently described for solid cells may be adopted

[35]. Any well-behaved function Q(z) can be written as a polynomial expansion as follows

$$Q(z) = \sum_{n=0}^{\infty} c_n \left(\frac{z}{H} \right)^n \tag{75}$$

Following this, s(z) can be determined by twice integrating the governing ordinary differential equation that contains the polynomial expansion for Q(z). The second part of the solution, w(r,z), given by equation (51) remains unchanged.

4.2 Comparison with finite-element simulation

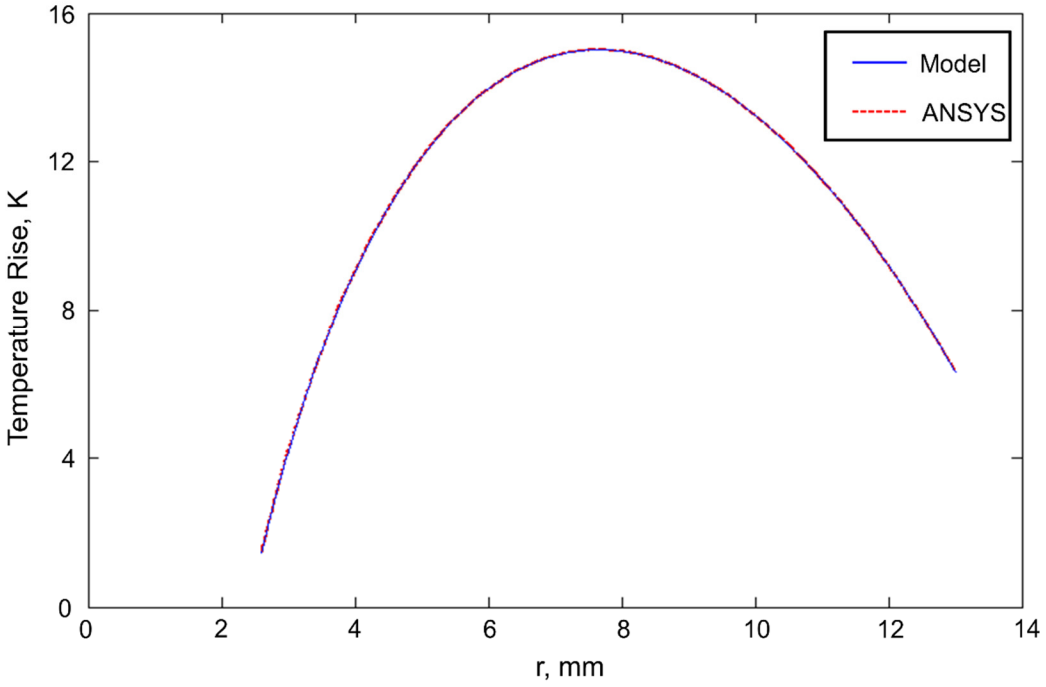

Figure 4.2. Comparison of temperature distribution as a function of *r* predicted by the steady state model with finite-element simulation results.

In order to validate the model presented in Section 4.1, the temperature distribution computed from the model is compared with finite-element simulations. Figure 4.2 plots the steady-state temperature computed using equations (49)-(58) as a function of the radial coordinate at mid-height. The cell considered here has the same outer dimensions as a 26650 cell, but has an axial hole of radius 1.3 mm. The convective heat transfer coefficients are assumed to be h_{ri}=1000 W/m^{2}K, h_{ro}=100 W/m^{2}K and h_z=100 W/m^{2}K. Based on recent measurements [22], the thermal conductivities of the cell are assumed to be k_r=0.2 W/mK and k_z=30 W/mK respectively. The cell is assumed to dissipate 6 W power. The temperature distribution predicted by a finite-element simulation software is also plotted, and there is excellent agreement between the two. The negligible error between the two occurs due to truncation errors in the respective computations.

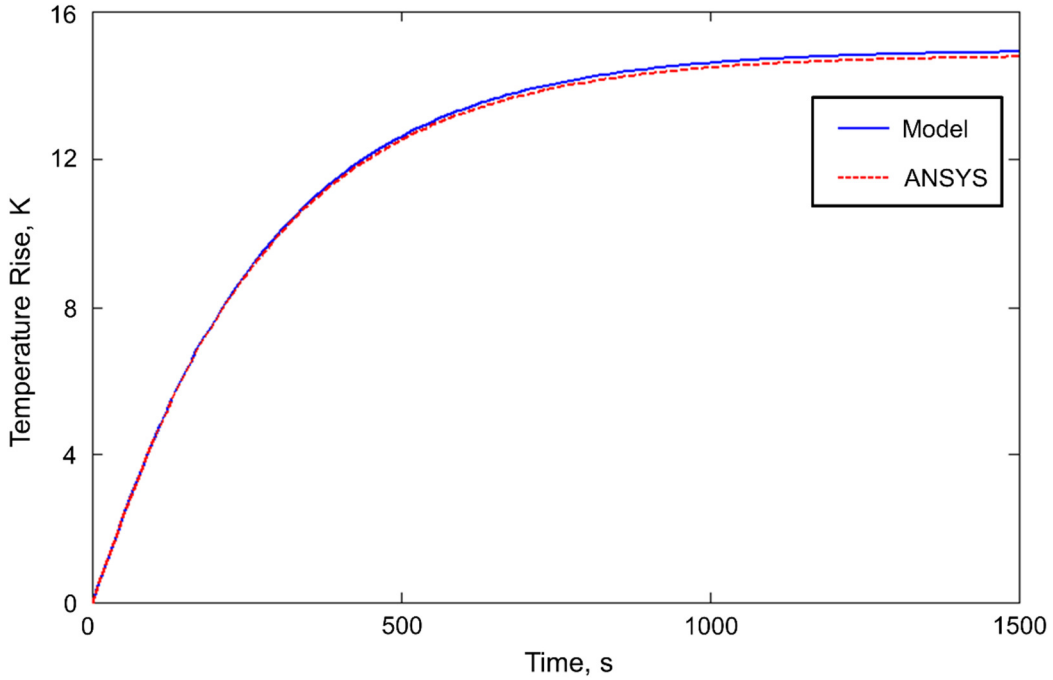

Figure 4.3. Comparison of peak cell temperature as a function of time predicted by the transient model with finite-element simulation results.

Figure 4.3 plots the temperature computed using equations (65)-(74) at the center of the cell material at mid-height as a function of time. The value of R_i is taken to be 2.6mm, and all other parameters are the same as Figure 4.2. Similar to Figure 4.2, there is good agreement between the transient model and finite-element simulation results.

Compared to the finite-element simulation, the analytical model presented in Section 4.1 is capable of computing temperature much faster, only a few seconds for the entire temperature distribution in the cell, compared to several minutes for a typical finite-element simulation tool, without even accounting for time needed to set up and mesh the problem geometry. Moreover, the analytical model provides a fundamental understanding of thermal characteristics of the annular cell, and facilitates rapid parametric studies of the effect of different variables on the temperature distribution.

4.3 Results and discussion

The analytical model presented in Section 4.1 is used for developing an understanding of the effect of various parameters on the temperature distribution in the annular cell, and to examine various trade-offs in the thermal design of an annular cell.

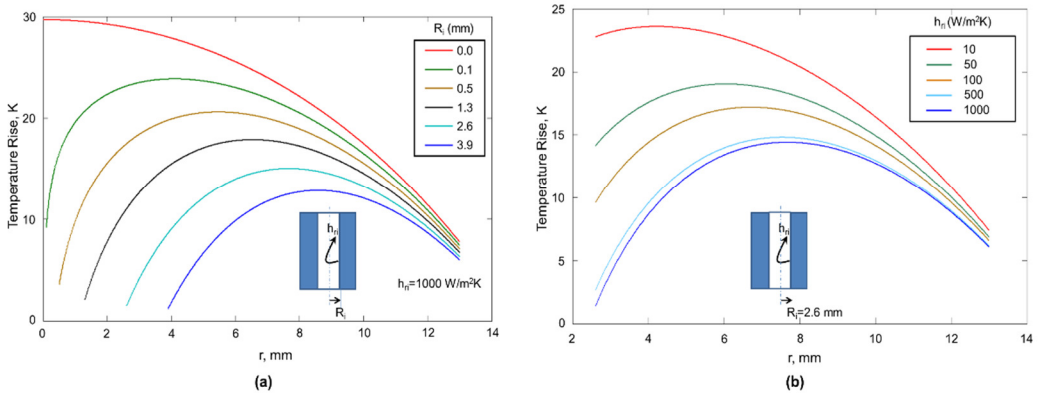

Figure 4.4. (a) Steady state temperature as a function of r for different values of R_i at fixed h_{ri}; (b) Steady state temperature as a function of h_{ri} for different values of R_i at fixed R_i.

Figures 4.4(a) and 4.4(b) plot the radial temperature distribution at mid-height as function of the inner radius R_i, and the inner convective heat transfer coefficient h_{ri} respectively for fixed outer geometry of the cell. In Figure 4.4(a), h_{ri} is held constant at 1000 W/m^{2}K, and in Figure 4.4(b), R_i is held constant at 2.6 mm. Figure 4.4(a) shows that as the inner radius increases, there is a substantial reduction in peak temperature rise. The peak temperature rise for an equivalent solid cell without an axial channel is 30.0 °C, also shown in Figure 4.4(a). In addition to temperature reduction, there is also a shift in the location where the peak temperature rise occurs. The greater the inner radius, the farther out is the location of peak temperature rise. Figure 4.4(b) shows, as expected, that for a given cell geometry, increasing the convective heat transfer coefficient h_{ri} reduces the peak temperature rise. A larger value of h_{ri} could be obtained, for example, by increasing the flow rate or thermal conductivity of the coolant.

Another possible strategy to reduce temperature rise through axial cooling is to precool the coolant prior to entering the annular cylinder. Figure 4.5 plots radial temperature distributions at mid-height when the coolant is precooled by different temperatures.

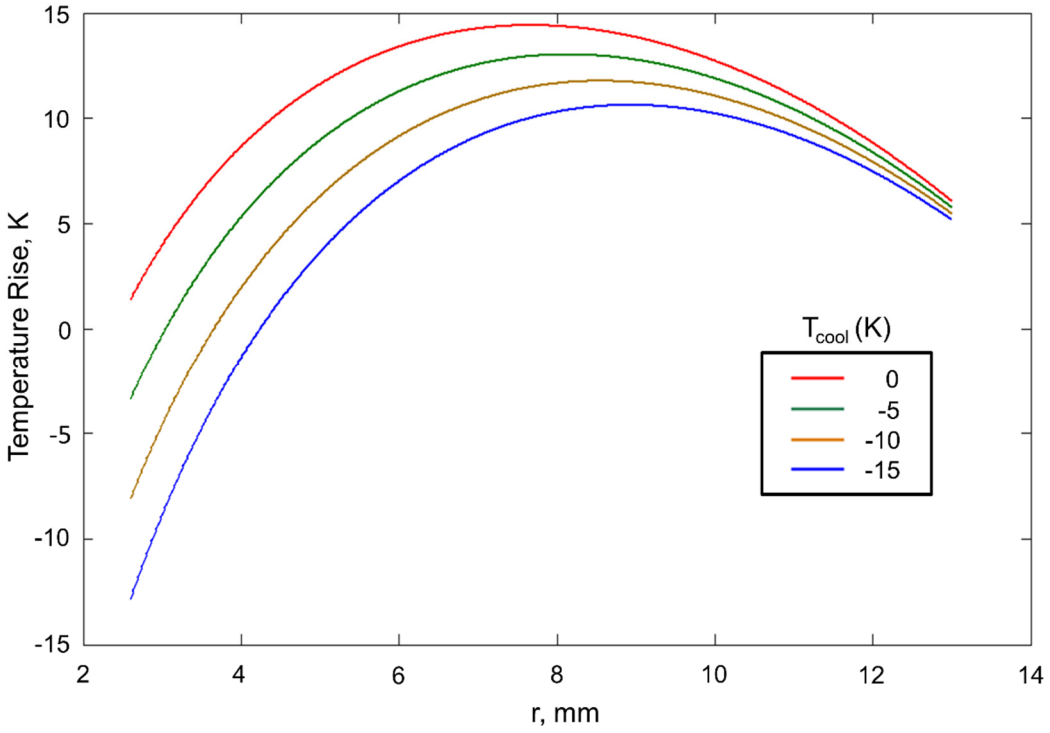

Figure 4.5. Temperature distribution in the annular cell as a function of extent of precooling of the coolant fluid.

Figure 4.5 shows that precooling may not be a particularly effective strategy for cooling of Li-ion cells. For example, precooling the coolant by 10 °C results in a peak temperature reduction of less than 5 °C. Precooling offers the advantage that it partially shifts the cooling load from the cell to the coolant, which in most cases is likely to be easier to implement, for example by using a remotely located chiller. It is possible in certain applications where performance is critical, and the cost of precooling is acceptable, that precooling may be an attractive option.

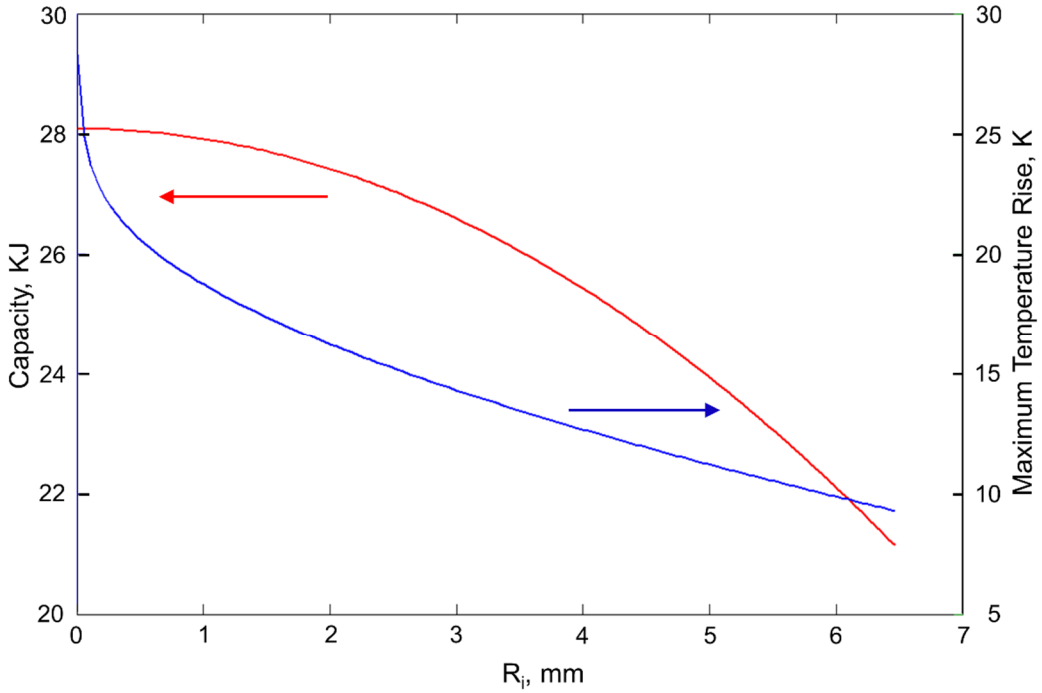

Figure 4.6. Cell capacity and peak temperature rise as functions of inner radius R_i.

One fundamental thermal-electrical trade-off that active cooling of an annular Li-ion cell must address is the trade-off between reduction in cell temperature and reduction in cell capacity. By increasing the inner radius of the annular cylinder, it is possible to reduce the cell temperature due to increased coolant flow. However, this also results in reduction in capacity of the cell since the increased coolant flow region reduces the cell volume and hence the cell capacity. This trade-off is analyzed in Figure 4.6, which plots the peak temperature rise in the cell and total capacity as functions of the inner radius of the cell. The heat generation rate in the cell is assumed to stay the same at 6 W. The baseline case considered here is that of a 26650 cell that delivers 2.6 A-hr charge at 3.0 V, resulting in a total energy capacity of 28080 J. It is assumed that the capacity scales

with the cell volume, since the volume directly influences that total volume of electrodes within the cell, thus affecting the capacity of the cell.

It is seen that increasing the inner radius results in rapid temperature reduction. The temperature curve in Figure 4.6 is very steep at low R_i. This indicates that even an axial hole of very small diameter results in significant temperature reduction with negligible reduction in capacity. For example, an annular cell with R_i=0.1 mm results in a temperature rise of only 24 °C compared to a 30 °C temperature rise for an equivalent 26650 cell without an axial channel. At the same time, the reduction in cell capacity due to the axial channel is negligible. At a somewhat larger value of R_i=1.3 mm, the reduction in capacity is still only 1% whereas there is a 40% reduction in peak temperature compared to the equivalent cell without an axial channel. However, as R_i increases, the cell capacity also reduces, due to which the trade-off between capacity reduction and improved thermal performance must be analyzed in detail. A reduction in peak temperature rise of a cell due to active cooling presents a direct opportunity to improve the electrical performance of the cell. The thermal head provided by the reduced cell temperature enables, for example an increase in the C-rate of the cell. The C-rate of the cell can be increased in order to reach the baseline temperature rise. This opportunity enabled by active cooling, however comes at the cost of reduced cell capacity. Thus, active cooling can be thought of as a means to balance the trade-off between capacity and power of a Li-ion cell.

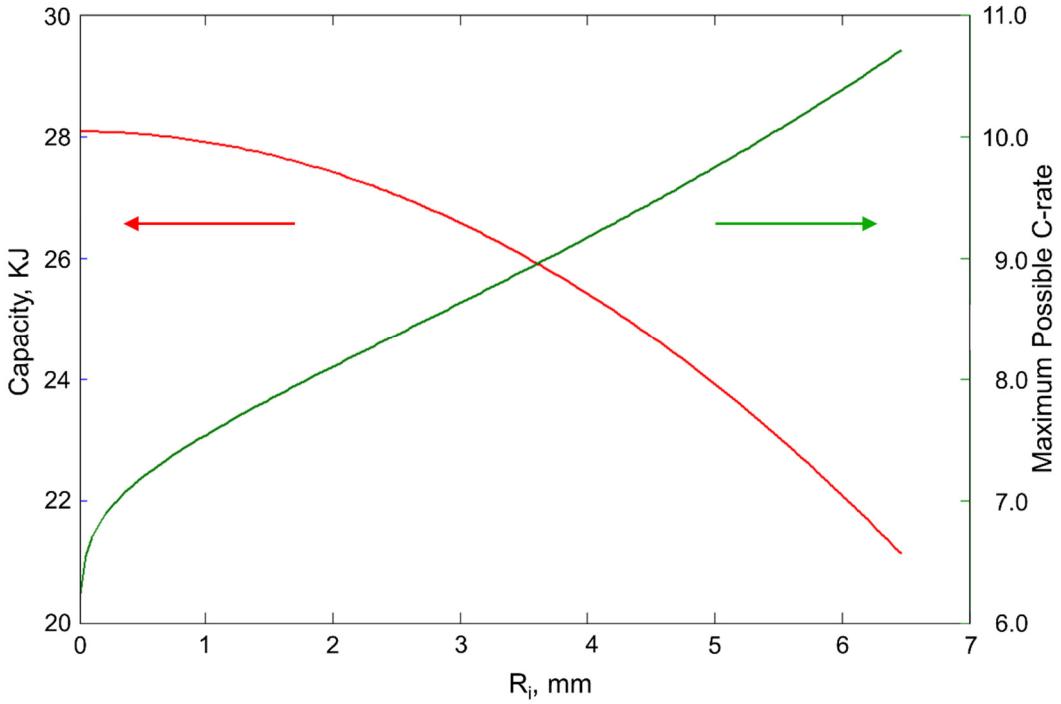

Figure 4.7. Maximum possible C-rate and cell capacity as function of inner radius R_i.

Figure 4.7 examines this by plotting the total capacity and C-rate as functions of the inner radius R_i, while keeping all other parameters constant. In particular, the C-rate is chosen in order to maintain the same peak temperature rise of 30 °C. The heat generation rate in the cell is modeled to vary as the square of the C-rate, or discharge current. That is,

$$Q = I^2 r_{\text{int},eff} \tag{76}$$

Where $r_{int,eff}$ is the effective internal resistance of the cell that determines the heat generation rate. Note that $r_{int,eff}$ absorbs a number of disparate heat generation mechanisms that occur inside the cell, including Ohmic losses, entropic heating, heats of reactions, etc. [5,86]. In Figures 4.6 and 4.7, a Li-ion cell with a capacity of 2.6 A-hr is assumed for calculating the C-rate. Figure 4.7 shows that by increasing the radius of the axial channel in the Li-ion cell, the C-rate of the cell can be increased significantly without any increase in operating temperature. Even small R_i results in significant potential for C-rate improvement. However, even with R_i as small as 1.3 mm, the C-rate can be 7.7 compared to the baseline C-rate of 6.0 for a solid cell, with minimal reduction in cell capacity.

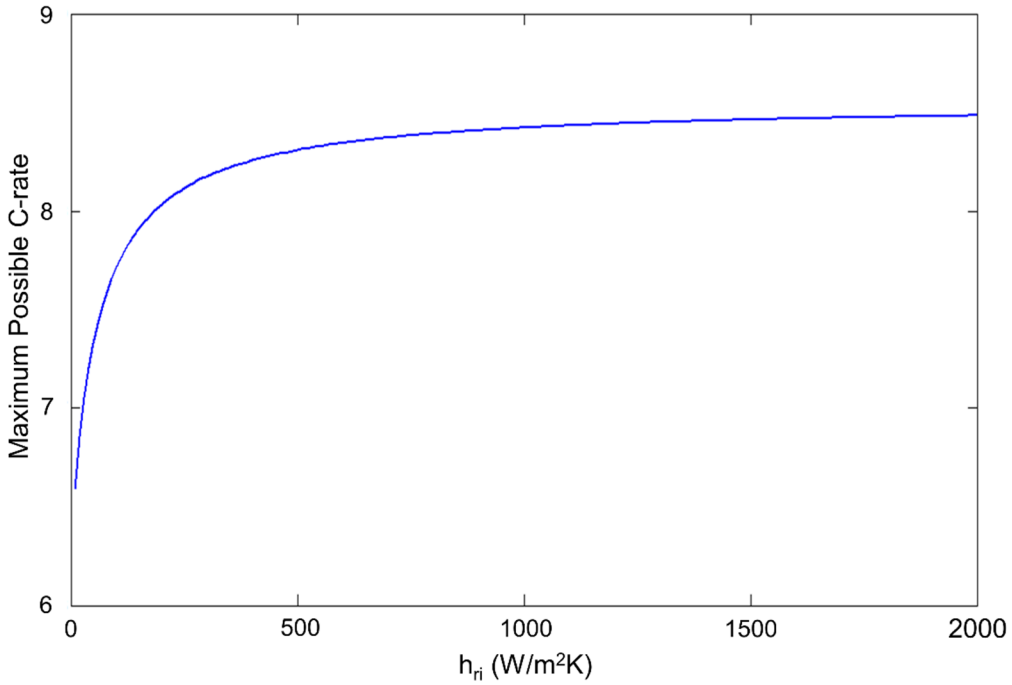

Figure 4.8. Maximum possible C-rate as a function of h_{ri} for fixed R_i.

The improvement in C-rate due to effective cooling, as demonstrated in Figure 4.7 is also a function of h_{ri}, the convective heat transfer coefficient available at the inner wall of the cell where heat is convected out from the cell into the cooling fluid. Improvement in h_{ri} can be brought about by increasing coolant flowrate, increasing coolant thermal conductivity, etc. Improvement in h_{ri} is expected to result in reduced temperature, and hence increased C-rate to maintain the same baseline temperature. Figure 4.8 plots the maximum possible C-rate as a function of h_{ri}, and shows that initially, C-rate increases rapidly with increasing h_{ri}. This effect however diminishes at large values of h_{ri}, and the improvement obtained in C-rate is minimal a value of h_{ri} of about 300 W/m^{2}K. This is because at large h_{ri}, convection to the coolant fluid is no longer the thermal bottleneck, and hence further improvement in h_{ri} does not any more result in significant further improvement in C-rate. Given the critical importance of limiting temperature rise in Li-ion cells in order to prevent thermal runaway, it may be acceptable to sacrifice some capacity in return for improved thermal performance, which as shown in Figures 4.6 and 4.7 may in turn be used to increase discharge rates. Other challenges that may need to be considered in the system-level analysis of this trade-off include the pumping power required to flow coolant through the axial channel, which can be large particularly for small sized channels, sealing of the channel, and its effect on the electrochemistry of the cell.

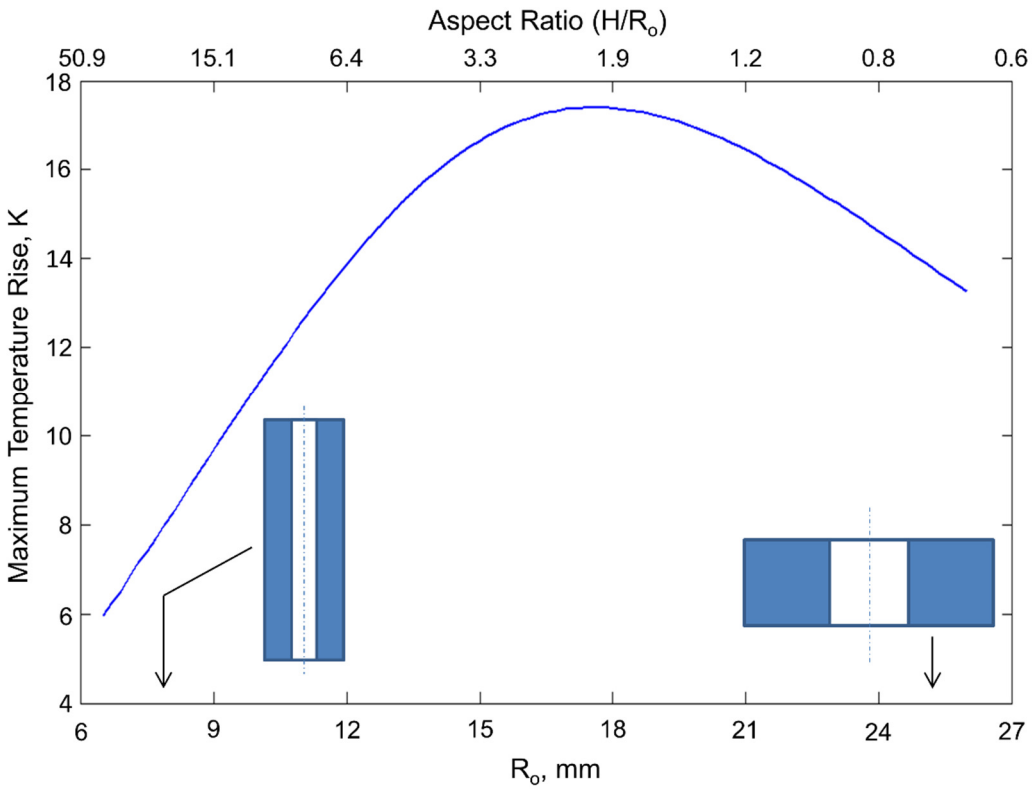

Figure 4.9. Effect of cell sizing on thermal performance of the annular cell.

Figure 4.9 analyzes the effect of the overall shape of the annular Li-ion cell on maximum temperature rise in the cell, which is plotted as a function of the outer radius R_o. The overall volume of the cell is maintained constant, in this case equal to the volume of the 26650 cell. As R_o increases, the cell becomes shorter and stouter. In each case, R_i is maintained at 20% of R_o. Figure 4.9 shows that as R_o increases, the peak temperature of the cell increases until a worst-case value of R_o beyond which the temperature reduces. This phenomenon occurs because as R_o changes, the surface area, and hence the rate of convective heat transfer from cell to the ambient changes. The worst-case value of R_o can be thought of as one at which the available convective surface area is the minimum, resulting in worst

conditions for convective heat loss from the cell. Figure 4.9 indicates that tall and slender cells may in general be thermally more attractive.

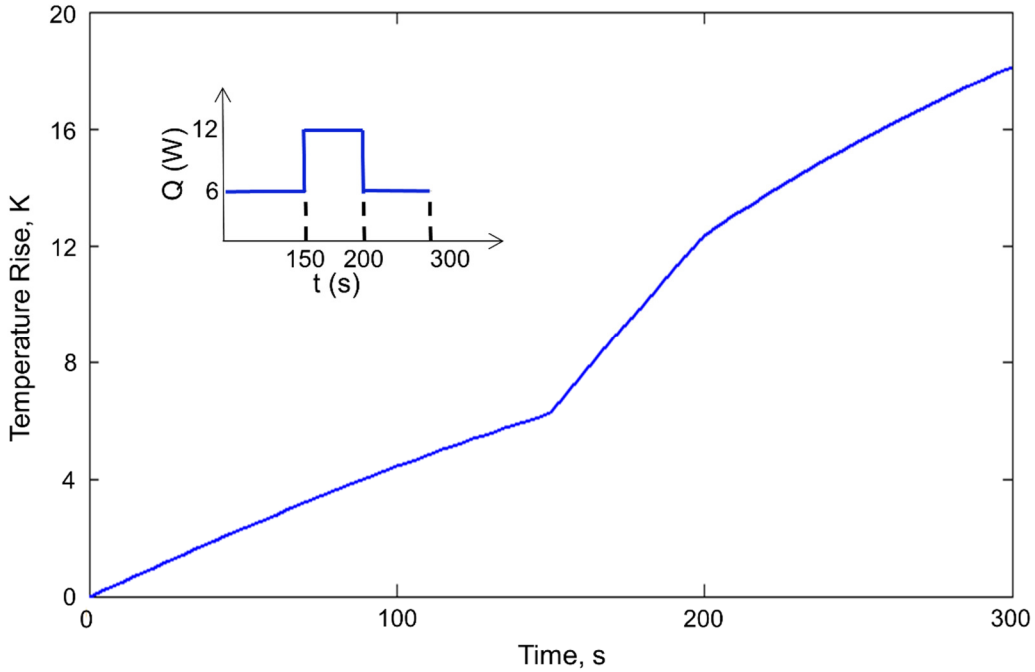

Figure 4.10. Computed temperature at the center of the cell material as a function of time for a short time excursion in heat generation rate.

Figures 4.10 and 4.11 present applications of the transient model discussed in Section 4.1.2. The case of a discharging annular Li-ion cell is considered. Figure 4.10 considers a transient scenario where there is a sudden in heat generation rate in a Li-ion cell, possibly due to short circuiting. The heat generation rate is assumed to rise from 6 W to 12 W for a period of 50s. The variation of temperature with time, computed using the model in Section 1.2, shows a sudden spike in the rate at which temperature increases. Once the heat generation rate returns to baseline value, so does the rate of increase in temperature.

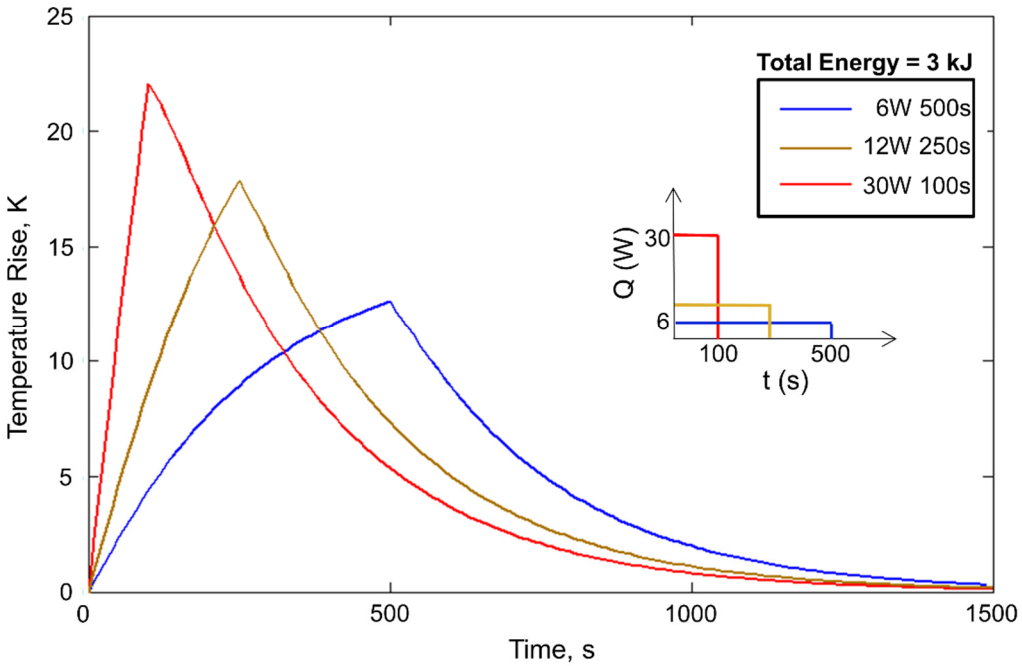

Figure 4.11. Peak cell temperature as a function of time for pulsed discharge processes at different rates, with fixed total discharge energy.

On the other hand, discharge at a low C-rate results in lower heat generation, but longer duration for the heat generation. In Figure 4.11, the cell is assumed to discharge a specific amount of energy, 3000 J in this case. Three different cases are considered with different C-rates, due to which heat dissipation of the cell and duration of discharge vary. For discharge at a high C-rate, the heat generation rate is large, while the discharge duration is small. On the other hand, discharge at a low C-rate results in lower heat generation, but longer duration for the heat generation. The peak temperature of the cell is plotted as a function of time during these discharge processes. It is found that despite the shorter discharge duration, the peak temperature rise in the high power discharge case is the highest. This indicates that from a thermal perspective, it is preferable to discharge at low rates, even if the discharge lasts for a longer duration. Note,

however, that a longer duration discharge reduces overall system throughput, since each discharge process takes a long time. Figure 4.6 quantifies a typical thermal vs. performance trade-off that must be considered in the design of the operation of annular Li-ion cells.

The availability of analytical tools to predict steady-state and transient temperature distribution in Li-ion cells could be used by the Battery Management System (BMS) to take smart, thermal-based decisions to maximize system-level performance without overheating. For example, based on current loads, the BMS can predict when a particular cell is close to overheating, and can accordingly reduce load at the appropriate time.

CHAPTER 5

AN ITERATIVE, ANALYTICAL METHOD FOR SOLVING CONJUGATE HEAT TRANSFER PROBLEMS

Shah, K., & Jain, A. (2015). An iterative, analytical method for solving conjugate heat transfer problems. International Journal of Heat and Mass Transfer, 90, 1232-1240.

Abstract

Conjugate heat transfer involving convection and conduction in a fluid flow and a solid body in contact with each other occurs commonly in engineering applications. While analytical solutions for the individual convection and conduction problems are relatively easier, it is a lot more challenging to solve the combined conjugate heat transfer problem. In this paper, an iterative method is developed for analytically solving conjugate heat transfer problems. Based on an initial assumption of the temperature field at the solid-fluid interface, the temperature distributions in the fluid and solid body are determined by separately solving the governing energy conservation equations in the two domains. These solutions are used to improve the initial assumption of the interface temperature until convergence. It is found that only a few iterations of this process are needed for convergence. Temperature fields computed from this analytical approach are found to be in good agreement with finite element simulation results. The iterative analytical approach is used to solve two technologically relevant problems related to internal and external flows. Given the general nature of the iterative approach, results from this paper may be helpful in solving a variety of conjugate heat transfer problems.

Keywords: Conjugate Heat Transfer, Thermal Conduction, Convection, Analytical Methods.

5.1 General Solution: The Iterative Approach

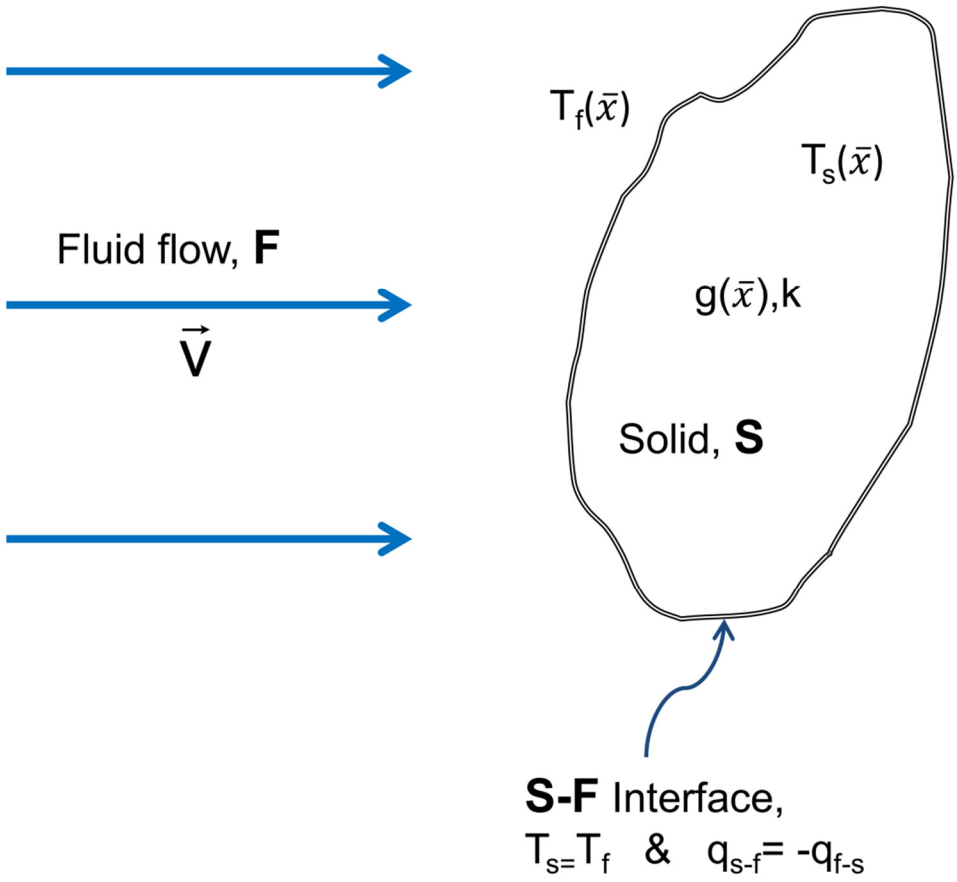

Figure 5.1. Schematic of a general conjugate heat transfer problem involving a fluid flow over an arbitrarily shaped solid with internal heat generation.

This section presents the general approach for analytically solving a conjugate problem involving thermal conduction and convection in a solid and fluid flow respectively. Consider a solid (**S**) with an arbitrary shape as shown in Figure 5.1. Fluid flow **(F)** occurs with a given velocity profiles. The solid and fluid phases intersect at an interface, denoted by **S-F**. In general, internal heat generation within the solid

is considered. Although Figure 5.1 shows an external flow scenario, in general, fluid flow may occur either over the solid (external flow), or it may be enclosed by the solid (internal flow).

In general, the interest is in deriving expressions for temperature distributions $T_s(\bar{x})$ and $T_f(\bar{x})$ where $\bar{x}$ is the general spatial coordinate. Only the laminar, steady state problem is considered here. The governing conservation equations that must be solved to determine these temperature distributions are given by

$$\alpha\nabla^2 T_f = (\vec{v}\cdot\nabla)T_f + \mu\cdot\Phi + \bar{g}_f \tag{77}$$

and

$$k\nabla^2 T_s + g_s(\bar{x}) = 0 \tag{78}$$

Here, $\mu\cdot\Phi$ is the viscous dissipation, and $\bar{g}_f$ and $\bar{g}_s$ are volumetric heat generation rates in the solid and fluid respectively. The methodology discussed in this paper for deriving analytical solutions for the temperature fields in **S** and **F** is based on analytically solving the temperature fields individually in the solid and fluid domains, and utilizing principles of temperature compatibility and conservation of energy at the interface to iterate until a stable solution is obtained. To start with, the fluid temperature distribution at the interface **S-F** is assumed to be

$$T_f(\bar{x}_{S-F}) = T_0(\bar{x}_{S-F}) \tag{79}$$

Assuming the velocity field in the fluid is known in advance, equation (77) can now be solved along with the assumed boundary condition at the interface.

Once $T_f(\bar{x})$ is known, the heat flux into the solid at the solid-fluid interface can be obtained by differentiating.

$$q_{s,in}(\bar{x}) = k_f \frac{\partial T_f}{\partial \bar{n}} \tag{80}$$

Where $\bar{n}$ is the outward normal to the solid surface at the **S-F.**

Equation (80) represents a boundary condition for the temperature distribution in the solid $T_s(\bar{x})$. The governing equation (77) can now be solved along with equation (80). The solution for $T_s(\bar{x})$ provides a means to determine the temperature of the solid at the interface, which can then be used to update the interface temperature distribution that was assumed in equation (78). The entire procedure can be repeated to determine the temperature distributions over multiple iterations. Eventually, the temperature distributions may be expected to converge, with negligible change from one iteration to the next.

The analytical framework described above is used for analyzing both internal and external flows, which are discussed in subsequent sub-sections.

5.2 Internal flow

Consider the laminar flow of a fluid through an annular cylinder, shown schematically in Figure 5.2(a). The fluid flow is assumed to be hydrodynamically fully developed when it enters the cylinder, with a given velocity profile $u(r^+)$ and entry temperature T_e at the entrance, $z^+=0$. The solid portion of the cylinder is assumed to generate heat with a volumetric rate of Q. Convective heat transfer with coefficients h_{ro} and h_z are assumed over the outer surface and axial faces of the cylinder respectively.

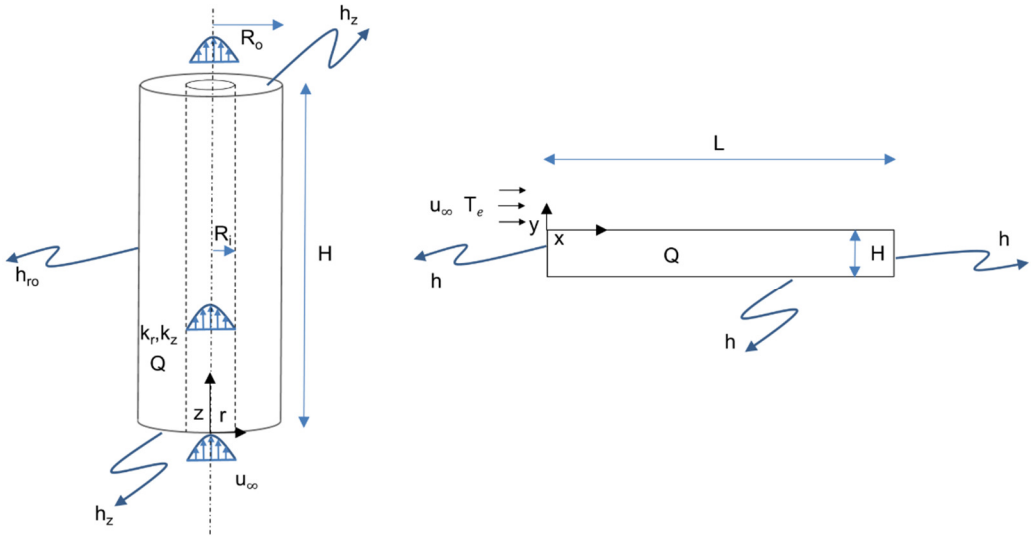

Figure 5.2. (a) Schematic of hydrodynamically fully developed flow through an annular cylinder with anisotropic thermal conductivity and volumetric internal heat generation, (b) Schematic of fluid flow with constant freestream velocity over a semi-infinite flat plate with volumetric heat generation.

To start with, a temperature distribution is assumed at the wall

$$T_{wall}(z^+) = T_0(z^+) \tag{81}$$

Neglecting viscous dissipation, heat transfer in the fluid domain is governed by the following governing conservation equation [50],

$$\frac{\partial^2 T_f}{\partial r^{+2}} + \frac{1}{r^+}\frac{\partial T_f}{\partial r^+} = (1 - r^{+2})\frac{\partial T_f}{\partial z^+} \tag{82}$$

The non-dimensional parameters z^+ and r^+ are given by

$$z^+ = \frac{z / R_i}{\mathrm{Re}\cdot \mathrm{Pr}} \tag{83}$$

$$r^+ = \frac{r}{R_i} \tag{84}$$

The temperature solution based on a given $T_{wall}(z^+)$ is obtained as follows

$$T_f(z^+, r^+) - T_e = \int_0^{x^+} \left[1 - \theta(z^+ - \xi, r^+)\right] \frac{dT_{wall}}{d\xi} d\xi + \sum_{i=1}^{k} \left[1 - \theta(z^+ - \xi_i, r^+)\right] \left(T_{wall}(i) - T_e\right) \tag{85}$$

The integral in equation (85) accounts for continuous variations in wall temperature and summations account for discrete step changes. Note that the coolant entry temperature T_e could be lower than zero in case the coolant fluid is precooled prior to entering the annular cylinder. This helps analyze the effect of precooling.

The function θ is given by

$$\theta(z^+, r^+) = \sum_{n=0}^{\infty} C_n R_n(r^+) \exp(-\lambda_n^2 z^+) \tag{86}$$

Here, λ_n are the eigenvalues, R_n are the corresponding eigenfunctions and C_n are constants. Analytical expressions for λ_n, R_n and C_n are given by Sellars, *et al.* [56].

Equations (43)-(44) define the temperature solution within the fluid, from which the wall heat flux can be obtained:

$$q_{wall}(z^+) = \frac{k}{R_i} \left. \frac{\partial T_f}{\partial r^+} \right|_{r^+=1}$$

$$= -\frac{k}{R_i} \left[\int_0^{z^+} \theta_{r^+}(z^+ - \xi, r^+) \frac{dT_{wall}}{d\xi} d\xi + \sum_{i=1}^{k} \theta_{r^+}(z^+ - \xi_i, r^+) \left(T_{wall}(i) - T_e\right) \right] \tag{87}$$

where,

$$\theta_{r^+}(x^+, 1) = -2 \sum_{n=0}^{\infty} G_n \exp(-\lambda_n^2 x^+) \tag{88}$$

Analytical expression for G_n is also provided by Sellars, *et al.* [56]. Equation (88) provides an analytical basis for computing the heat flux distribution at the solid-fluid interface, given an assumed temperature distribution at the wall. Once the heat flux is determined, the temperature distribution in the solid domain can be

computed. In this case, the governing equation for the temperature distribution in the solid domain is

$$\frac{1}{R_i^2}\frac{k_r}{r^+}\frac{\partial}{\partial r^+}\left(r^+\frac{\partial T_s}{\partial r^+}\right)+\frac{k_z}{H^2}\frac{\partial^2 T_s}{\partial z^{+2}}+Q=0 \qquad (89)$$

where $T_s(r^+,z^+)$ is the temperature rise in the solid. Note that thermal conductivities in the radial and axial directions are assumed to be unequal, in order to account for the general case of anisotropic thermal conduction in the Li-ion cell [22].

The governing equation is subject to the following boundary conditions:

$$\frac{\partial T_s}{\partial z^+}=Bi_z \mathrm{T_s} \qquad \text{at } z^+=0 \qquad (90)$$

$$\frac{\partial T_s}{\partial z^+}=-Bi_z T_s \qquad \text{at } z^+=1 \qquad (91)$$

$$\frac{\partial T_s}{\partial r^+}=\frac{R_i}{k_r}q_{wall}(z^+) \qquad \text{at } r^+=1 \qquad (92)$$

$$\frac{\partial T_s}{\partial r^+}=-Bi_{R_o}\frac{R_i}{R_o}T_s \qquad \text{at } r^+=R_o/R_i \qquad (93)$$

Note that the wall heat flux in the boundary condition at $r^+=1$ can be obtained based on the solution of the fluid problem. The temperature field may be determined by first splitting $T_s(r^+,z^+)$ into two components

$$T_s(r^+, z^+) = T_{s1}(z^+) + T_{s2}(r^+, z^+) \tag{94}$$

Where

$$T_{s1}(z^+) = \frac{QH^2}{2k_z}\left[z^+\left(1 - z^+\right) + Bi_H^{-1}\right] \tag{95}$$

and

$$T_{s2}(r^+, z^+) = \sum_{n=1}^{\infty}\left[\left(A_n + B_n\right)\cdot I_0(\lambda_n r^+ R_i) + \left(A_n\beta_1 + B_n\beta_2\right)\cdot K_0(\lambda_n r^+ R_i)\right]\cdot\left[\mu_n H Cos\left(\mu_n H z^+\right) + Bi_H Sin\left(\mu_n H z^+\right)\right] \tag{96}$$

The coefficients A_n and B_n in equation (96) are given by

$$A_n = \frac{-\int_0^1 T_{s1}(z^+)\left[(\mu_n H) Cos\left(\mu_n H\cdot z^+\right) + Bi_H Sin\left(\mu_n H\cdot z^+\right)\right]dz^+}{\frac{1}{2}\left[(\mu_n H)^2 + Bi_H{}^2 + 2Bi_H\right]\cdot\left[I_o(\lambda_n R_o) + Bi_{R_o}(\lambda_n R_o)\cdot I_1(\lambda_n R_o) + \beta_1\left(K_o(\lambda_n R_o) - Bi_{R_o}(\lambda_n R_o)\cdot K_1(\lambda_n R_o)\right)\right]} \tag{97}$$

$$B_n = \frac{\frac{R_i}{k_r}\int_0^1 q_{wall}(z^+)\left[\mu_n Cos\left(\mu_n H\cdot z^+\right) + Bi_H Sin\left(\mu_n H\cdot z^+\right)\right]dz^+}{\frac{1}{2}(\lambda_n R_i)\left[\left(\mu_n H\right)^2 + Bi_H{}^2 + 2Bi_H\right]\cdot\left[I_1(\lambda_n R_i) - \beta_2\left(K_1(\lambda_n R_i)\right)\right]} \tag{98}$$

where

$$\beta_1 = \frac{I_1(\lambda_n R_i)}{K_1(\lambda_n R_i)} \tag{99}$$

$$\beta_2 = \frac{k_r \lambda_n I_1(\lambda_n R_o) + h_{ro} I_o(\lambda_n R_o)}{k_r \lambda_n K_1(\lambda_n R_o) - h_{ro} K_o(\lambda_n R_o)} \tag{100}$$

The eigenvalues $\mu_n H$ are obtained from roots of the transcendental equation

$$Tan(\mu H) = \frac{2Bi_H \cdot (\mu H)}{(\mu H)^2 - Bi_H{}^2} \tag{101}$$

Bi_H is the axial Biot number, defined as $Bi_H = \frac{h_z H}{k_z}$, and $\lambda_n = \sqrt{\frac{k_z}{k_r}}\mu_n$

Finally, $T_{wall}(z^+)$ is determined from the solid temperature distribution in equation (94) computed at $r^+=1$. This provides an update to the initial assumption of $T_{wall}(z^+)$ shown in equation (81) and initiates the next iteration of computing the fluid temperature field, followed by the solid temperature field. In order to avoid divergence, a weighted average of T_{wall} from the previous iteration and T_{wall} determined from the solid temperature field may be used for updating T_{wall} for the next iteration. Iterations are carried out until the change in $T_{wall}(z^+)$ from one iteration to the next is below a desired threshold.

5.3 External Flow

The application of the general approach outlined in section 5.11 is now discussed for solving an external flow problem, in which a fluid with a known freestream velocity flows over a heated solid. The flow is assumed to be laminar.

Similar to the problem discussed in Section 5.2, this is also a commonly encountered heat transfer problem. As shown schematically in figure 5.2(b), a semi-infinite flat plate of length *L* and thickness *t* generates heat at a volumetric rate of *Q*. Fluid flow occurs at the top surface with given freestream velocity and temperature of u_∞ and T_e respectively. The plate is also being cooled at the other three surfaces with convective heat transfer coefficient *h*.

The procedure starts with an assumed temperature distribution $T_{wall}(x)$ on the solid-fluid interface, $y=0$. Neglecting viscous dissipation, the governing energy equation for the fluid is

$$\alpha \frac{\partial^2 T_f}{\partial y^2} = u \frac{\partial T_f}{\partial x} + v \frac{\partial T_f}{\partial y} \tag{102}$$

The solution to equation (102) with the assumed wall temperature boundary condition is given by [50]

$$T_f(x, y) - T_e = \int_0^x [1 - \theta(\xi, x, y)] \frac{dT_{wall}}{d\xi} d\xi + \sum_{i=1}^{k} [1 - \theta(\xi_i, x, y)] (T_{wall}(i) - T_e) \tag{103}$$

where the function $\theta(\xi,x,y)$ is given by [50]

$$\theta(\xi, x, y) = \frac{T_{wall} - T_f}{T_{wall} - T_e} = \frac{0.331 \,\mathrm{Pr}^{1/3} \,\mathrm{Re}_x^{1/2} \, y}{x\left[1 - \left(\frac{\xi}{x}\right)^{3/4}\right]^{1/3}} - \frac{0.005405 \,\mathrm{Pr}\,\mathrm{Re}_x^{3/2} \, y^3}{x^3\left[1 - \left(\frac{\xi}{x}\right)^{3/4}\right]} \tag{104}$$

The integral and summation terms in equation (103) account for the variation in T_{wall} as a function of *x*, and any step changes that may exist in the T_{wall} distribution.

Similar to the internal flow problem, the wall heat flux can be computed as follows:

$$q_{wall}(x) = -k\left.\frac{\partial T_f}{\partial y}\right|_{y=0}$$
$$= k\left[\int_0^x \theta_y(\xi, x, 0)\frac{dT_{wall}}{d\xi}d\xi + \sum_{i=1}^{k}\theta_y(\xi_i, x, 0)\left(T_{wall}(i) - T_e\right)\right] \quad (105)$$

By differentiating (104) with respect to y, $\theta_{\mathrm{y}}(\xi, \mathrm{x}, 0)$ is given by

$$\theta_{\mathrm{y}}(\xi, \mathrm{x}, 0) = \frac{0.331\,\mathrm{Pr}^{1/3}\,\mathrm{Re}_{\mathrm{x}}^{1/2}}{\mathrm{x}}\left[1 - \left(\frac{\xi}{\mathrm{x}}\right)^{3/4}\right]^{-1/3} \quad (106)$$

$q_{wall}(x)$ computed by equation (105) is then used to provide a boundary condition for the energy conservation equation that governs the temperature distribution in solid:

$$\frac{\partial^2 T_s}{\partial x^2} + \frac{\partial^2 T_s}{\partial y^2} + \frac{Q}{k} = 0 \quad (107)$$

where $T_s(x,y)$ is the temperature rise above ambient in the solid.

The governing equation is subject to the following boundary conditions:

$$\frac{\partial T_s}{\partial x} = \frac{h}{k}T_s \qquad \text{at x = } 0 \qquad (108)$$

$$\frac{\partial T_s}{\partial x} = -\frac{h}{k}T_s \qquad \text{at x = } L \qquad (109)$$

$$\frac{\partial T_s}{\partial y} = \frac{h}{k}T_s \qquad \text{at y = } -H \qquad (110)$$

$$k\frac{\partial T_s}{\partial y} = -q_{wall}(x) \qquad \text{at y = } 0 \qquad (111)$$

Solution for $T_s(x,y)$ proceeds along similar lines as the previous section. The temperature field may be determined by splitting $T_s(x,y)$ into two components

$$T_s(x, y) = p(x) + w(x, y) \tag{112}$$

The two components of the temperature distribution are given by

$$p(x) = \frac{QL^2}{2k}\left[\frac{x}{L}\left(1-\frac{x}{L}\right)+\frac{1}{Bi_L}\right] \tag{113}$$

and

$$w(x,y) = \sum_{n=1}^{\infty}\left[C_n Cosh(\mu_n y) + D_n\left(\beta_n Cosh(\mu_n y) + Sinh(\mu_n y)\right)\right]\cdot\left[\mu_n L Cos(\mu_n x) + Bi_L Sin(\mu_n x)\right] \tag{114}$$

The coefficients C_n, D_n and β_n in equation (114) are given by

$$C_n = \frac{-h\int_0^L p(x)\cdot\left[\mu_n Cos(\mu_n x)+(h/k)Sin(\mu_n x)\right]dx}{\frac{1}{2}\cdot L\cdot\left[\left(\mu_n^2 LH + Bi_H Bi_L\right)\left(1+\frac{Bi_L}{(\mu_n L)^2+Bi_L^2}\right)+Bi_H\right]\cdot\left[k\mu_n Sinh(\mu_n H)+hCosh(\mu_n H)\right]} \tag{115}$$

$$D_n = \frac{\int_0^L q(x)\cdot\left[\mu_n Cos(\mu_n x)+(h/k)Sin(\mu_n x)\right]dx}{\frac{1}{2}\cdot L\cdot\mu_n k\left[\left(\mu_n^2 LH + Bi_H Bi_L\right)\left(1+\frac{Bi_L}{(\mu_n L)^2+Bi_L^2}\right)+Bi_H\right]} \tag{116}$$

$$\beta_n = \frac{k\mu_n Cosh(\mu_n H) - h \cdot Sinh(\mu_n H)}{k\mu_n Sinh(\mu_n H) + h \cdot Cosh(\mu_n H)} \tag{117}$$

The eigenvalues μ_n are obtained from roots of the transcendental equation

$$Tan(\mu L) = \frac{2Bi_L \cdot (\mu L)}{(\mu L)^2 - Bi_L{}^2} \tag{118}$$

Where $Bi_H = \frac{hH}{k}$ & $Bi_L = \frac{hL}{k}$

This completes the solution methodology for the external flow problem. The wall temperature determined from the solid temperature distribution may be used to repeat the process outlined above, starting with solving the fluid flow problem, which will iteratively lead to a converged solution.

Characteristics of the general methodology outlined above are discussed in the next section. Comparison with finite-element simulation results is also shown. Applications of the method for internal and external flow problems are also discussed.

5.4 Results and Discussion

The solution methodology described and illustrated for internal and external flows in section 5.2 and 5.3 is iterative in nature, beginning with a guessed temperature distribution along the solid-liquid interface. To understand the nature of convergence of this iterative process, two problems – one of internal flow, and another of external flow – are solved using the iterative technique. For the internal flow problem, hydrodynamically developed flow of air entering at a uniform temperature and fluid velocity of 0.5 m/s through a 0.065 m long annular cylinder with annulus diameter of 0.0026 m is considered.

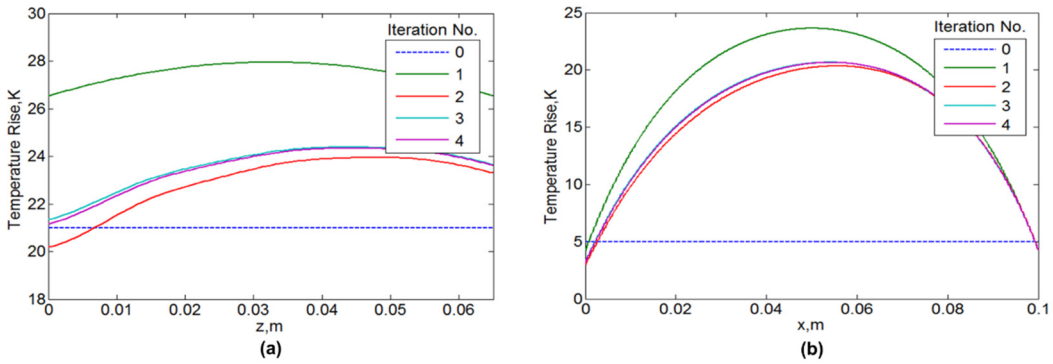

Figure 5.3. (a) Temperature distribution along the inner wall as a function of number of iterations for the internal flow problem, (b) Temperature distribution along the solid-fluid interface as a function of number of iterations for the external flow problem.

For the external flow problem, flow over a 0.03 m thick plate at fluid velocity of 0.01 m/s is considered. Internal heat generation of 6 W and 30 W is considered within the solid domain for the internal and external flow cases respectively. Heat transfer coefficient of 100 $W/m^2 \cdot K$ and 50 $W/m^2 \cdot K$ is considered along all other surfaces for the internal and external flow cases respectively. Axial and radial thermal conductivity values of 30.0 and 0.2 $W/m \cdot K$ are assumed for the solid in the

internal flow case. This models thermal conduction in systems like Li-ion cells, where thermal conduction is known to be highly anisotropic [22]. For external flow problem, an isotropic slab with thermal conductivity of 0.2W/m·K is considered. Figures 5.3(a) and 5.3(b) plot the temperature distributions at the start of successive iterations along the solid-liquid interface for the internal flow and external flow problems. The initial assumed wall temperature is also shown. Figures 5.3(a) & 5.3(b) show excellent convergence of the temperature distribution within 4-5 iterations, even when the temperature distribution assumed initially is not accurate.

In case of the internal flow problem, the accuracy of the temperature solution further depends on the number of eigenvalues considered for the infinite series solution represented by equation (118). Figure 5.4 plots the temperature distribution at the solid-liquid interface for the internal flow problem as a function of the number of eigenvalues considered. It is found that using around 8-10 eigenvalues is sufficient, and the solution does not change significantly by considering additional eigenvalues.

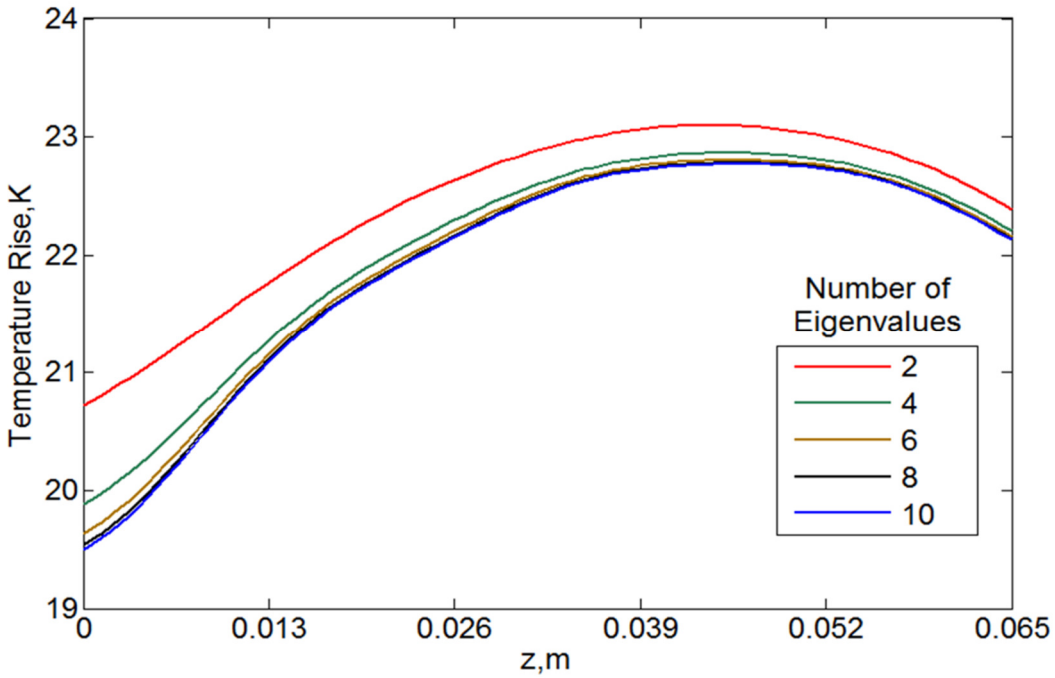

Figure 5.4. Temperature distribution as function of eigenvalues considered in the internal flow solution.

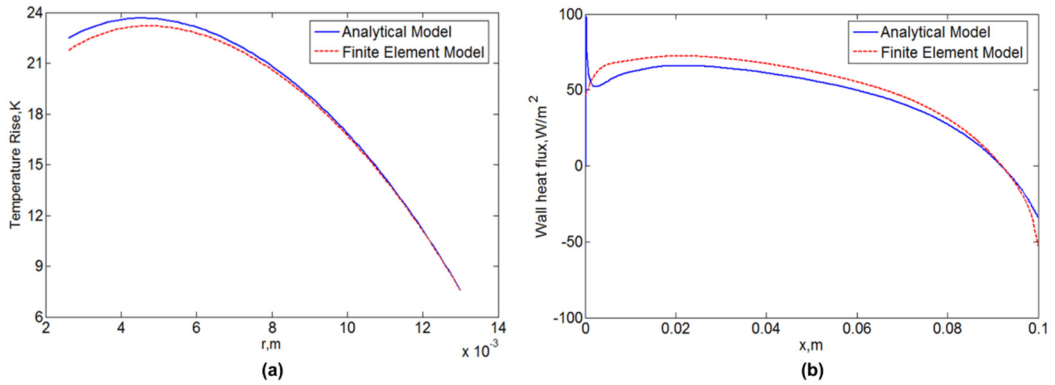

Figure 5.5. (a) Comparison of temperature plot inside the solid computed using the iterative model for internal flow problem with finite element simulation results, (b) Comparison of wall heat flow computed using the iterative model for external flow problem with finite element simulation results.

The analytical solutions derived for internal and external flow using the methodology described in section 2 are also compared against finite-element

simulation results for validation. The finite-element simulations are carried out in ANSYS. Sufficient grid refinement is carried out to ensure grid independence of results. Figure 5.5(a) plots the temperature rise at mid height along the radius for the internal flow problem, using the iterative analytical model, as well as finite-element simulations. There is excellent agreement between the two. Similarly, Figure 5.5(b) shows good agreement for wall heat flux for the external flow problem between the analytical model and finite-element simulation results.

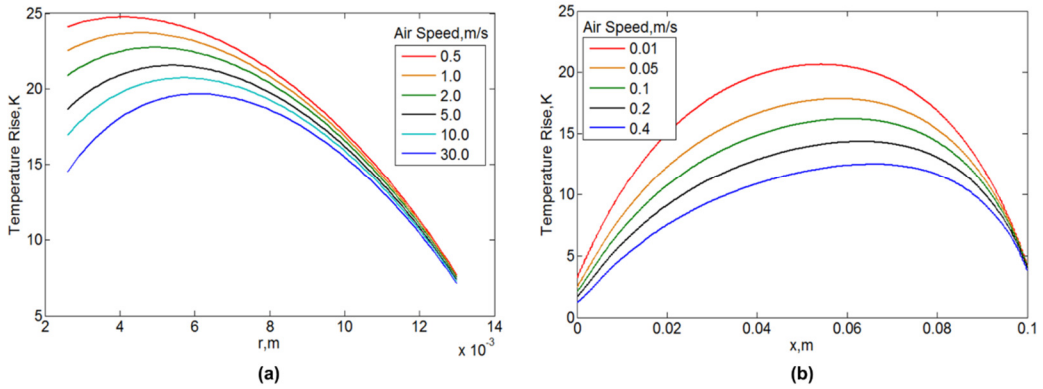

Figure 5.6. (a) Solid temperature as a function of radius at mid-height for different air speeds in the internal flow problem, (b) Wall temperature distribution in the external flow problem for different air speeds

Figures 5.6(a) and 5.6(b) plot the temperature distributions in the solid body for internal and external flow cases respectively for a number of inlet fluid velocities. As expected, in each case, the iterative model discussed in Section 5.2 and 5.3 predicts a strong reduction in peak temperature as the fluid velocity increases. While the wall temperature continues to reduce as the fluid velocity is increased, this effect of fluid velocity on the solid temperature distribution is most

prominent at the wall, particularly for the effect saturates in regions closer to the outer wall, where the effect of the coolant flow is not so prominent.

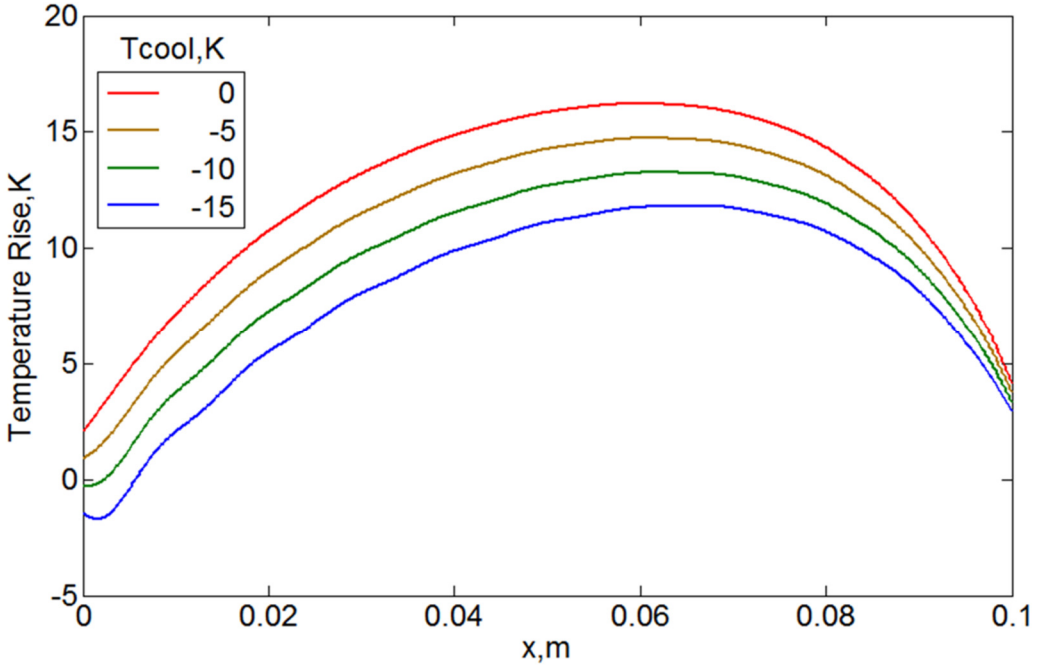

Figure 5.7. Wall temperature distribution in the external flow problem for different precooling temperatures at 0.1 m/s coolant speed.

Figure 5.7 presents results for the effect of precooling the inlet fluid in the external flow problem for a fluid velocity of 0.1m/s. It is found that reducing the inlet flow temperature reduces the wall temperature distribution, plotted in Figure 5.7 as a function of length along the cylinder. However, the effect is not very significant. For example, even for a precooling of -15 K, the model computations predict a peak temperature drop of only 5 K at most.

Figure 5.8(a) examines the wall heat flux from the heat-generating solid into the cooling fluid as a function of the coordinate along the flow, plotted for a number of fluid flow speeds. In each case, the wall heat flux is positive for nearly the entire

length, except for a small region towards the end. In this region, the sign of the heat flux reverses, and heat flows back from the fluid into the solid. This interesting phenomenon occurs because as the fluid traverses the length of the solid, it progressively gets hotter, so that beyond a certain critical length, the heat flow direction reverses, and the fluid actually starts heating up the solid. This interesting behavior is seen at all fluid speeds.

In Figure 5.8(b), the wall heat flux is plotted along the length of the plate at fluid velocity of 0.1m/s at different precool temperatures. It is evident that precooling reduces the length over which reversal of heat flow occurs. Precooling may not affect the peak temperature of the plate significantly but may reduce or eliminate the local heating of the plate near the end region.

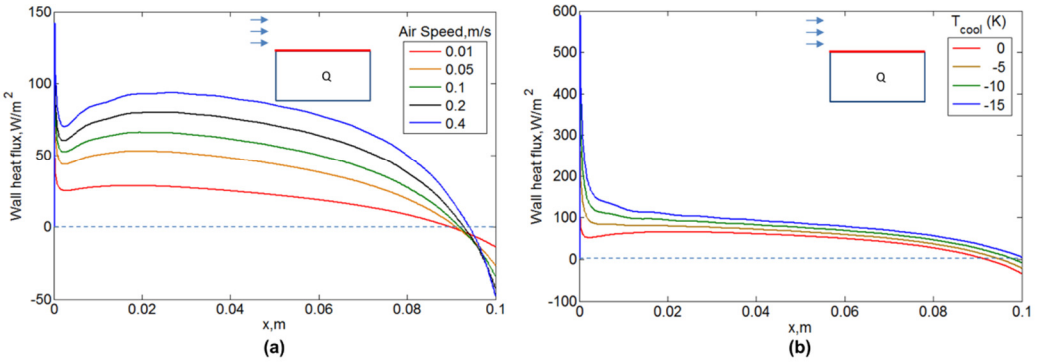

Figure 5.8. (a) Wall heat flux distribution in the external flow problem for different air speeds for no precooling, (b) Wall heat flux distribution in the external flow problem for different precooling temperatures at 0.1 m/s coolant speed.

As shown in figure 5.9(a), the location of heat flux reversal moves further downstream as the fluid velocity increases. On the other hand, the magnitude of the reversed heat flux also increases with increase in fluid velocity. Therefore,

figure 5.9(a) alone is not sufficient in knowing whether the overall reversed heat decreases with increase in fluid velocity.

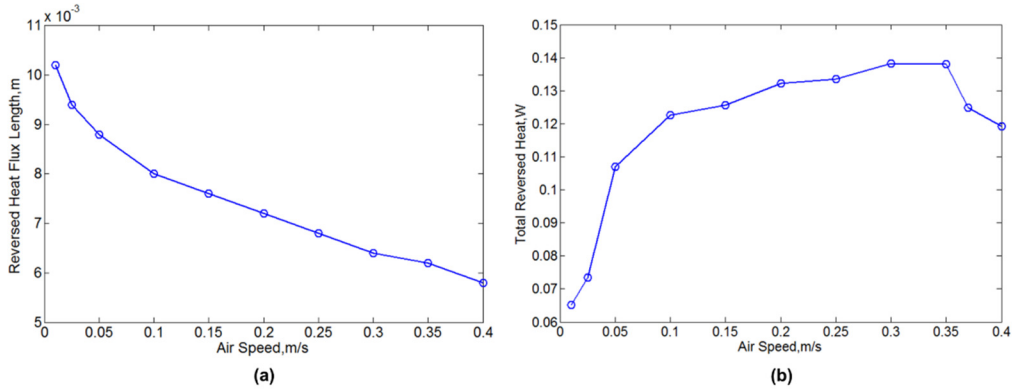

Figure 5.9. Variation of the heated length in external flow as a function of air speed, (b) Variation of total reversed heat in external flow problem as a function of air speed.

In figure 5.9(b), total reversed heat flow is plotted against fluid velocity by integrating the reversed heat flux over the heated length. The total reversed heat increases with increase in velocity up to a certain velocity, after which it starts going down. These plots may be useful in deciding the appropriate fluid velocity, and whether precooling may be helpful in the case of cooling a heat-generating solid with external flow.

CHAPTER 6

EXPERIMENTAL AND NUMERICAL INVESTIGATION OF CORE COOLING OF LI-ION CELLS USING HEAT PIPES

Shah, K., McKee, C., Chalise, D., & Jain, A. (2016). Experimental and numerical investigation of core cooling of Li-ion cells using heat pipes. Energy, 113, 852-860.

Abstract

While Li-ion cells offer excellent energy conversion and storage capabilities for multiple applications, including electric vehicles, heat removal from Li-ion cells remains a serious technological challenge that directly limits performance, and poses serious safety and reliability concerns. Due to poor thermal conductivity of Li-ion cells, traditional cooling methods like air cooling on the cell surface do not effectively access and cool the core. This may lead to large core temperatures and thermal imbalance within the cell. This paper investigates the cooling of Li-ion cells using an annular channel through the axis of the cell. Air flow through this channel and insertion of a heat pipe are both shown to result in effective cooling and temperature reduction of the cell core. A similar effect is observed when a thin metal rod is used instead of a heat pipe. Experimental measurements are found to be in good agreement with finite-element simulations. Experiments demonstrate that a heat pipe successfully prevents overheating in case of sudden increase in heat generation due to malfunction such as cell shorting. This paper illustrates fundamental thermal-electrochemical trade-offs in the design of cell cooling. These results may facilitate the development of novel and effective cooling techniques for Li-ion cells.

Keywords: Lithium-ion Cells; Thermal Runaway; Convective Cooling; Heat Pipe; Thermal Management**.**

6.1 Experimental Approach

6.1.1. Fabrication of annular thermal test cell

Electrochemical heat generation rate in a Li-ion cell varies as a function of the depth of discharge [25], and is difficult to measure directly [39]. Moreover, it is also not straightforward to measure temperature inside a Li-ion cell because a Li-ion cell is a hermetically sealed system, and drilling a hole to insert a thermocouple will disrupt the electrochemical function of the cell. As an alternative, a thermal test cell capable of precise, well-controlled heat generation through Joule heating and internal temperature measurement through embedded thermocouples is fabricated.

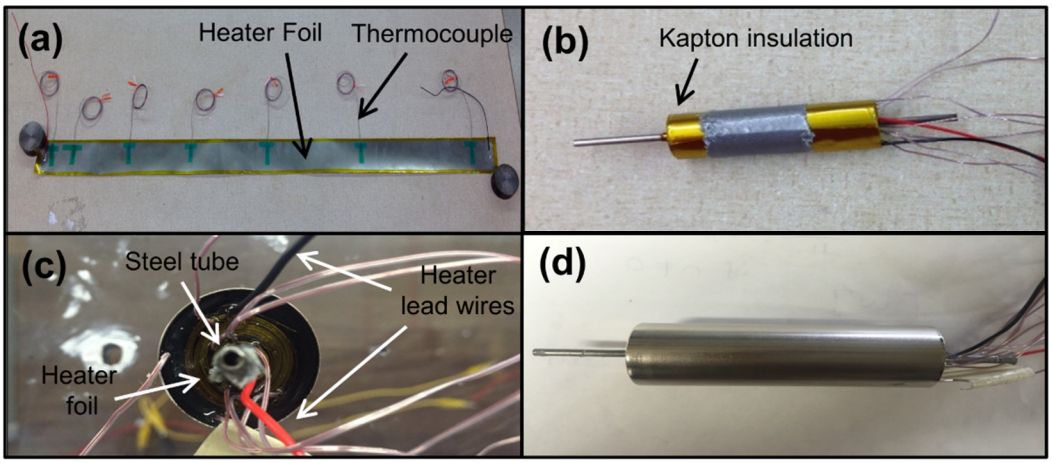

Figure 6.1. Annular thermal test cell fabrication process.

This allows precise thermal measurements at well-controlled and measurable heat generation rates corresponding to discharge at various C-rates without the added uncertainty due to the electrochemistry of an actual Li-ion cell. The thermal test cell is designed and fabricated to be the same dimensions as a

26650 cell, and the constituent materials are chosen in order to closely match the thermal transport properties of an actual Li-ion cell [22, 42].

Two thermal test cells with inner diameter of 2mm and 6mm are fabricated. A steel tube is first cut to approximately 110 mm in length. The outer surface of the tube is insulated with Kapton tape to prevent short circuiting. Next, a 25 μm thick stainless steel foil is cut 1000 mm long and approximately 62.5 mm wide. One side of this foil is insulated with Kapton tape to prevent the foil from short circuiting itself. Two 16 gauge wires are soldered to opposite ends of the foil for connecting to a power source. Seven T-type thermocouples are then placed at increasing distances from one another along the foil (Figure 6.1a). The foil is then wrapped around the steel tube as tightly as possible in order to increase total heater length and hence electrical resistance. Once tightly wound, the roll is secured with tape (Figure 6.1b). The tube and metal sheet roll are then placed inside the casing of the cell, and a thermocouple is also attached to the inside a 26650 cell casing (Figure 6.1c). The cell is filled with poly-dimethylsiloxane (PDMS), which is a thermally-curable polymer that fills up air voids within the test cell. Also, an additional ninth thermocouple is placed within the small layer of PDMS in between the foil and casing. All wires are threaded through a cap that is then inserted at the open end of the cell. PDMS inside the cell is cured at room temperature over a 24 hour period. Since uncured PDMS is very viscous, in order to fully remove air bubbles, PDMS is topped off and self-cured once more.

Figure 1d shows a top view image of the thermal test cell before sealing the top cap, showing the tightly wound metal heater coil and wires leading to the embedded thermocouples. The room temperature resistance of the heater coil is found to be 0.23 Ohms and 0.27 Ohms respectively for the heaters for the 6mm and 2mm hole diameter test cells, which was measured in a four-wire configuration due to the small value of the resistance. Resistance is found to be largely independent of temperature in the temperature range of interest due to the low temperature coefficient of resistance of the heater material.

6.1.2. Thermal property measurement of thermal test cell

Experiments are carried out to measure the key thermal transport properties of the thermal test cell, to ensure that these values are close to that of a Li-ion cell [22, 42]. Due to the spirally wound nature of the thermal test cell, similar to a 26650 Li-ion cell, a strong thermal conductivity anisotropy is expected, with radial thermal conductivity being much lower than the axial thermal conductivity. As a result, it is important to measure and characterize this rate-determining thermal property. This measurement is carried out by inserting a cartridge heater into the metal tubing of the test cell as shown in Figure 6.2. A T-type thermocouple is also placed on the outer surface of the test cell. The cartridge heater spans the entire length of the cell, ensuring uniform heating. The test cell is oriented horizontally in order to minimize heat loss through conduction from the axial ends. A heating current of 58 mA is passed through the heater using a Keithley sourcemeter 2401, resulting in 1.21 W Joule heating. Temperature measured by the outside thermocouple as well as those embedded in the thermal test cell are logged at 2Hz

frequency using a National Instruments DAQ 9213. Experiments are carried out in two different ambient conditions, until steady-state conditions are reached, defined as less than a 0.5 °C temperature change over 600 seconds. Steady-state temperature data are then analyzed and compared with a one dimensional model for heat flow through an annular radial geometry with heat flux at the inner radius to determine the radial thermal conductivity of the thermal test cell.

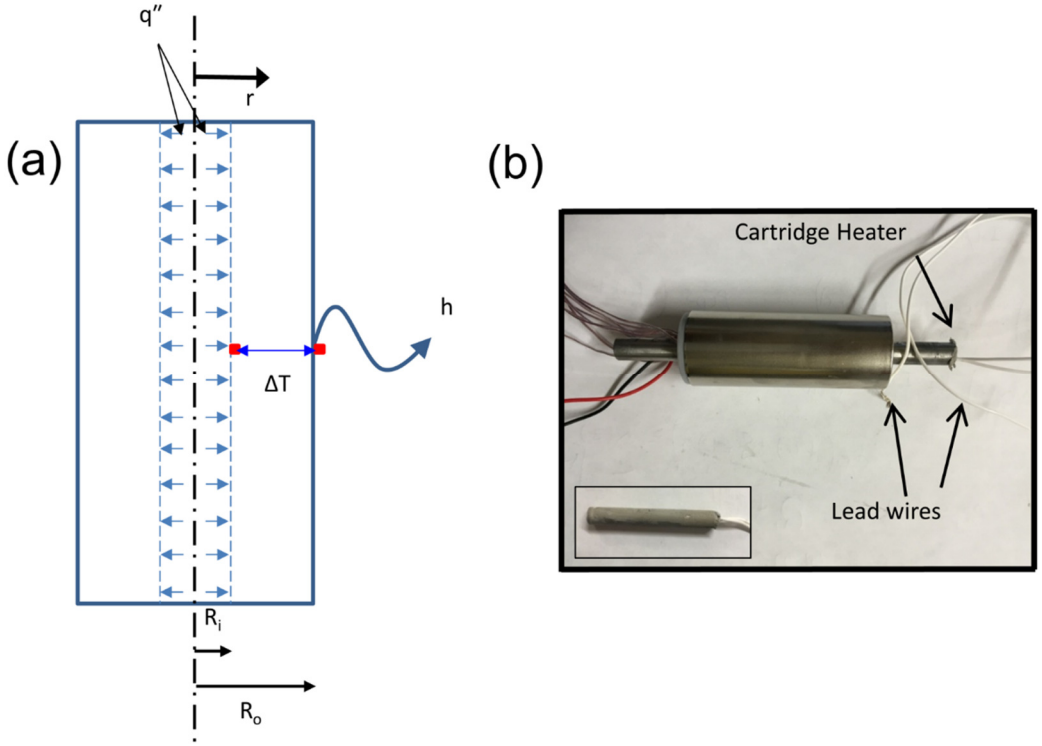

Figure 6.2. (a) Picture of radial thermal conductivity measurement setup, (b) Schematic of heater and thermocouple locations for k_r measurement.

Heat capacity of the test cell is determined by the mass-weighted average of the components used in fabricating the cell as follows:

$$Cp = \frac{\sum_{i=1}^{N} m_i C_{p,i}}{\sum_{i=1}^{N} m_i} \tag{119}$$

where m and C_p refer to mass and heat capacity respectively, and the summations take place over all constituent materials.

Unlike thermal conductivity, heat capacity is a scalar quantity which at this lengthscale is given accurately by the mass-weighted average of heat capacities of constituent materials [90]. All materials used in fabricating the test cell are standard, with well-known thermal properties.

6.1.3. Experimental setup for thermal measurements

Experiments are carried out to investigate the thermal effectiveness of annular cooling of the thermal test cell. In the first set of experiments, the effect of coolant air passing through the annular tube is investigated. The cell is suspended in a low speed wind tunnel by connecting flexible piping on either end of the metal tube inserted into the test cell. Flow rate and pressure of air flow through the cell are controlled and measured using a ball valve, flowmeter and pressure gauge are also utilized to control and measure flow rate and pressure. The pressure gauge used is an Ashcroft 1226 commercial pressure gauge which has an accuracy of ±3% of its/ full scale that is 100kPa. Two different flow meters by King instrument company are used. One of them has a range of 6CFH-60SCFH (standard cubic feet per hour). The resolution of this flowmeter is 2 SCHFH and the accuracy is ± 3.6 SCFH. The other flow meter has a range of 0.8 SCFM-8.2SCFM (standard cubic feet per minute), the resolution 0.2 SCFM and an accuracy of ±0.328SCFM. The volumetrically uniform heat is generated inside the cell by passing a heating current through the rolled metal foil in the test cell. A GPD-4303S programmable multichannel sourcemeter is used for this purpose. The sourcemeter has a current

range of 0-3A and voltage range of 0-30V. It has an accuracy of ± (0.2% of the set value+3mA). T-type thermocouples with an accuracy of 1 °C are embedded in the test cell are connected to a National Instruments DAQ 9213 for data acquisition. A number of experiments are carried out at various air flow rates, including a baseline experiment without any air flow. This experimental setup also enables the characterization of external cooling of the cell, where the airflow is directed over the cell instead of through the cell.

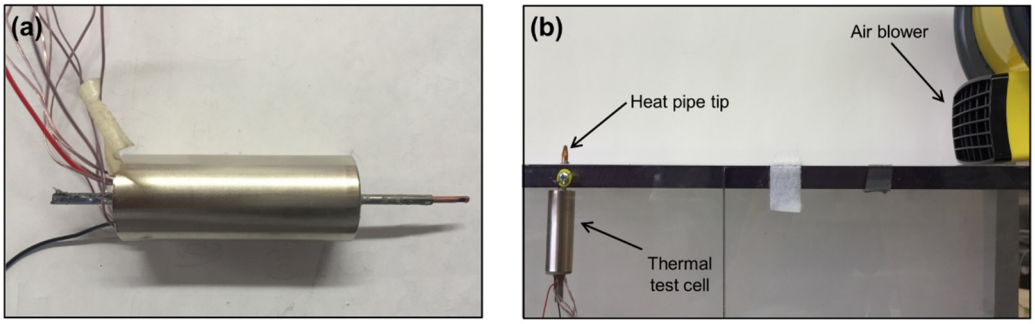

Figure 6.3. Pictures of experimental setup: (a) Wind tunnel experimental setup for studying heat pipe-based cooling, (b) Thermal test cell with heat pipe inserted in the annular region.

In the second set of experiments, passive cooling of the cell is investigated. A heat pipe is inserted into the metal tubing such that it can acquire heat from the entire length of the cell. Two Copper heat pipes of 2mm and 6mm diameter are used in these experiments. Each heat pipe is 10 cm in length. A test cell with a 2mm heat pipe is shown in Figure 6.3(a). The test cell is suspended from the top wall of the wind tunnel in such a way that the condenser end of heat pipe that allows heat loss to the ambient protrudes out of the wind tunnel (Figure 6.3(b)). A STANLEY High Velocity Blower Fan Model 655704 is placed outside the wind tunnel convects heat away from the condenser tip of the heat pipe. The airspeed from this

air blower is measured using an Extech mini thermo-anemometer. The anemometer can measure air speed from 0.5 to 28m/s with a resolution of 0.1m/s. The accuracy of the air speed measured is ± (3% reading + 0.2m/s). The air speed obtained from the blower is in the range of 0- 8.4 m/s. For further investigation of this approach, experiments are also carried out where the heat pipe is replaced by a copper rod of the same size.

The test cell is subjected to internal heat generation through Joule heating. Measurements are carried out in two ambient conditions – natural convection where the condenser tip of the heat pipe cools off by itself, and forced convection where an external air flow occurs over the heat pipe tip. In the latter case, the physical isolation of the test cell from the air flow ensures that the external air flow cools the heat pipe tip, and not the cell directly.

6.2 Finite-element simulations

A finite element model is developed in ANSYS CFX [91] to model the experiments. The geometry of experimental test cells is modeled. The thermal conductivity of the cell is treated as anisotropic, with a radial thermal conductivity value of k_r=0.25 W/mK, obtained from measurements as discussed in section 6.1.3 The value of uniform heat generation applied in the volume of the cell is taken to match experimental conditions. Appropriate fluid domains were also created for both the cooling cases. The geometry is meshed with over 1 million nodes, and grid independence checks are carried out.

For heat pipe based passive cooling, the heat pipe geometry is designed such that similar to experimental conditions, one end protrudes out of the test cell and

other end stays within. A fluid domain is created to simulate air flow over the heat pipe in the case of forced convection. Inlet air velocity is assigned at one of the sides of the fluid domain to represent the air blower supplying cooling air stream over the heat pipe tip. Similar to air cooling simulations, convective heat transfer coefficient of 10 W/m^2K is assigned to outer surfaces of the test cell, which is a typical value for natural convection conditions [41]. The effective thermal conductivity of the heat pipe is assumed to be 5000 W/mK. While the operation of a heat pipe is considerably complicated, involving fluid flow, phase change, etc., these phenomena result in a very high effective thermal conductivity that has often been used to simplify the modeling of a heat pipe [92].

6.3 Results and Discussion

6.3.1. Thermal property measurement results:

Thermal conductivity in the radial direction is a key thermal transport property of a Li-ion cell [22,35]. Due to the poor thermal properties of separator [93] and multiple thermal contact resistances in the rolled nature of the thermal test cell, similar to a Li-ion cell [48], the radial thermal conductivity k_r is expected to be much smaller than the axial component k_z, and hence likely to be the rate-determining thermal parameter. Experiments are carried out to determine the value of k_r as described in section 6.1.2. Considering an annular cylinder being heated on the inner surface and convectively cooled on the outer surface, the steady-state temperature distribution within the cylinder is given by

$$T(r) = \frac{q'' \cdot R_1}{k_r} \ln\left(\frac{R_1}{r}\right) + \frac{q''}{h}\frac{R_1}{R_2} \tag{120}$$

where k_r is the radial thermal conductivity and h is the convective heat transfer coefficient on the outside surface. q'' is the heat flux at the inner surface. R_1 and R_2 are inner and outer radii respectively. Note that in this case, temperature is not a function of the axial dimension z, since the cartridge heater supplies heat all along the z-axis. From equation (120), the temperature difference between the inner and outer surfaces is given by

$$\Delta T = T(R_1) - T(R_2) = \frac{q'' \cdot R_1}{k_r} \ln\left(\frac{R_2}{R_1}\right) \tag{121}$$

Equation (121) shows that the steady-state temperature difference between thermocouples mounted on the inner and outer surfaces can be used to determine the radial thermal conductivity, since q'', R_1 and R_2 are well-known.

Experiments are carried out in two different ambient conditions – free convective cooling of the thermal test cell, and forced convective cooling due to a stream of cooling air directed at the test cell. The measured temperature distribution within the cell is plotted in Figure 6.4 for both cases. The temperature difference ΔT between the innermost and outermost thermocouples results in consistent determination of k_r from both experiments. As expected, the measured temperature difference ΔT is nearly the same in both ambient conditions, resulting in thermal conductivity values of 0.25 W/mK and 0.26 W/mK in free and forced convection respectively. These values are very close to the radial thermal conductivity of a 26650 Li-ion cell [22].

Further, equation (120) is used to determine the radial locations of the thermocouples by fitting the expected radial temperature distribution through the experimental data. This precisely determines the locations of the embedded thermocouples as shown in Figure 6.4. For reference, the approximate thermocouple locations based on a top-view picture of the rolled thermal test cell

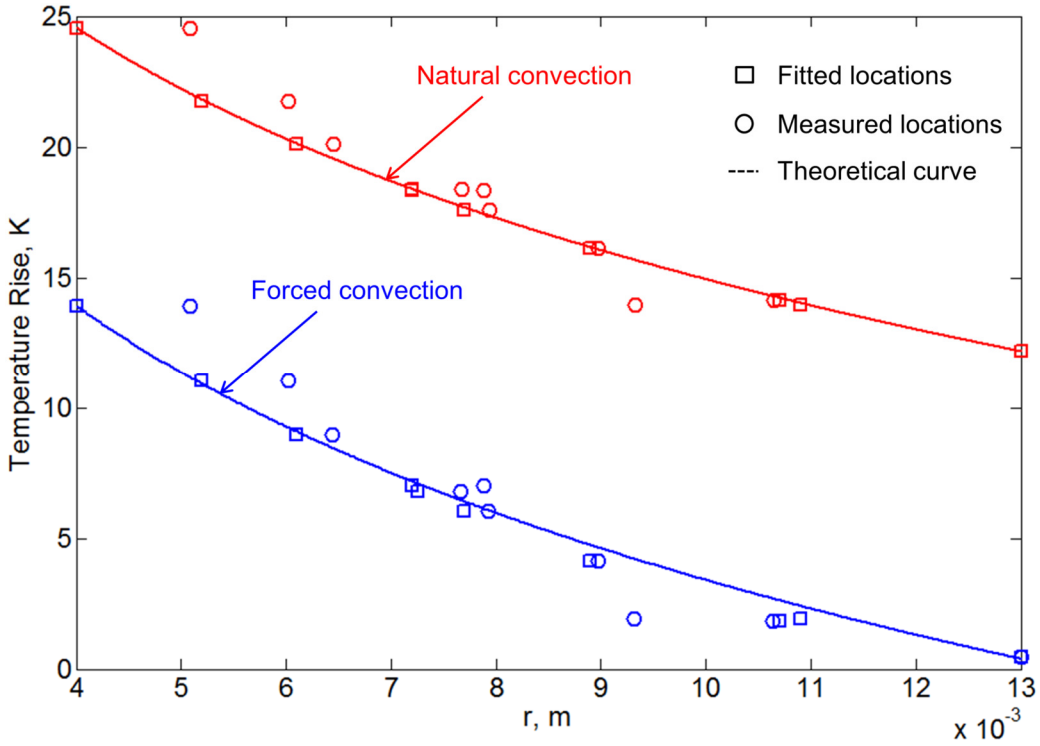

Figure 6.4. Measured T vs r and analytical model fit for radial thermal conductivity measurement at two different convective conditions.

prior to sealing the cell cap are also shown. In most cases, the experimentally determined locations are close to the approximate locations. While the thermocouples were distributed approximately uniformly during the rolling and assembly process of the test cell, some movement is likely, and these experiments help determine the precise locations of the thermocouples.

Once k_r has been determined, temperature measurement from the outer-most thermocouple can also be used to determine the value of the convective heat transfer coefficient h using equation (120). This value is found to be 15 W/m^{2}K and 591 W/m^{2}K for natural and forced convection respectively, both of which are well within the range of these convective cooling regimes [41].

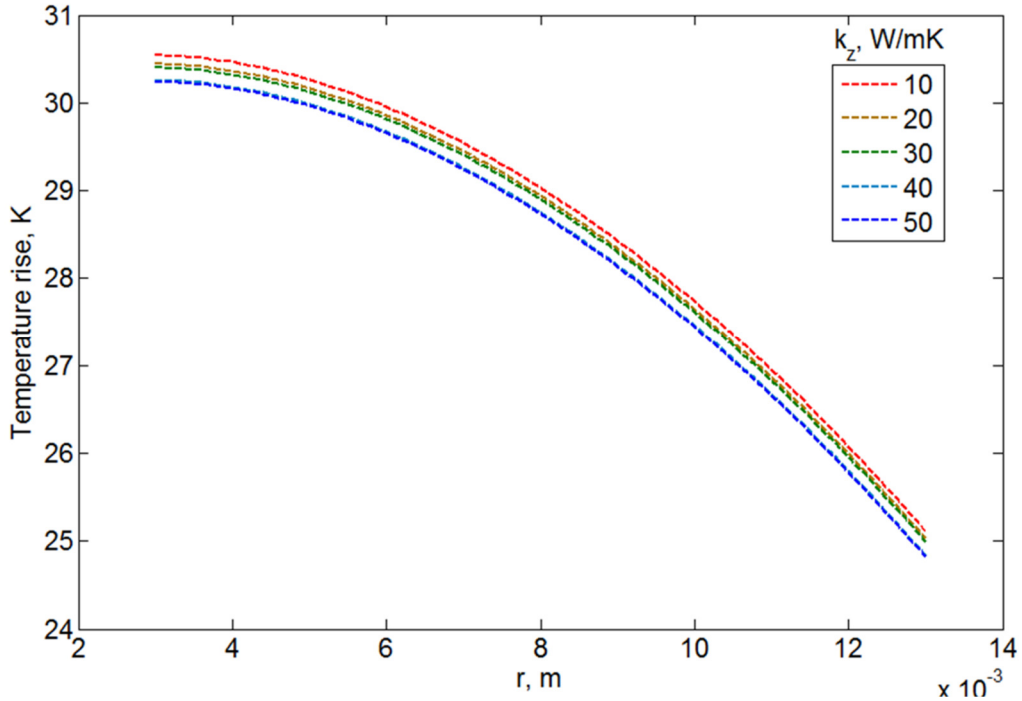

Figure 6.5. T vs. r for a number of k_z values, showing weak dependence on axial thermal conductivity.

Compared to k_r, the axial thermal conductivity k_z does not play a significant role in determining the thermal characteristics of the test cell, since k_z is typically much larger due to the availability of a high thermal conductivity pathway for axial heat transfer. Figure 6.5 plots the temperature distribution inside a cell for a fixed heat generation rate and convective cooling conditions for a number of k_z values based on a recently reported analytical thermal model of an annular geometry [65].

This plot shows that the temperature distribution is largely insensitive to k_z. A value of k_z=30 W/mK is assumed based on past measurements [22].

Note that in addition to a close match in k_r between the thermal test cell and a 26650 Li-ion cell, the specific heat and mass density are also found to match closely. The specific heat of the test cell, determined using a weighted average of its constituent materials is found to be 777 J/kgK, which is also close to a recently reported measurement of 749 J/kgK [42]. The mass density of the test cell is found to be 2093 kg/m^3, which is close to the value of 2285 kg/m^3 for a 26650 cell. Overall, the thermal mass of the thermal test cell is 56 J/K, compared to 59 J/K for a 26650 Li-ion cell.

6.4.2. Internal cooling

A set of experiments are carried out to investigate the effect of internal flow through the annular tube of the thermal test cell on temperature distribution in the test cell. Data is obtained for cells with 2mm and 6mm diameter inner tubes.

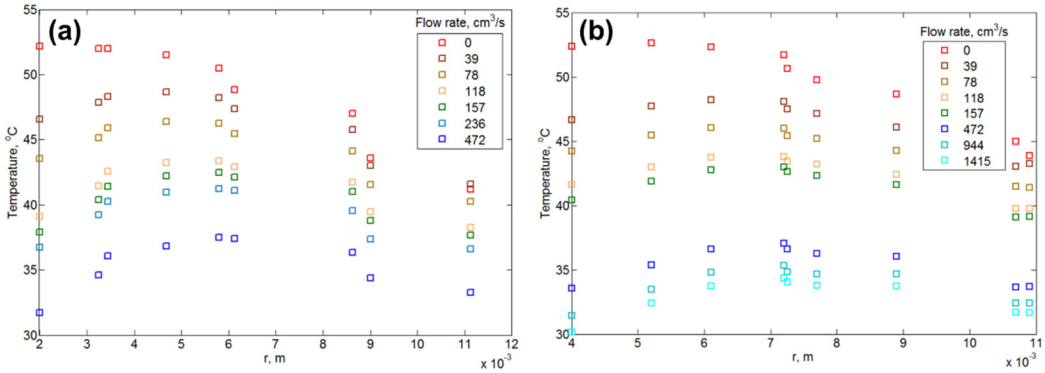

Figure 6.6. Temperature distribution within the cell for baseline and several internal flowrates for (a) 2mm cell, (b) 6mm cell.

Figures 6.6(a) and (b) present the measured temperature distribution for 2mm and 6mm cells respectively for a fixed heat generation rate, but with different

coolant flowrates. The presence of even a small coolant flowrate is shown to result in significant temperature reduction in comparison with the baseline case of no cooling. Specifically, the thermocouple closest to the core of the cell experiences the greatest temperature reduction – nearly 22 °C reduction with 1415 cm^3/s air flow, and the peak temperature rise shifts outwards within the cell. In comparison, temperature in the outer regions of the cell that are farthest from the coolant flow also reduces, but not as dramatically. The effect of the coolant flow saturates somewhat with increasing flowrate, most likely because thermal conduction within the cell begins to dominate the overall thermal transport process. For example, there is not much further reduction in temperature between 472 and 1415 cm^3/s measurements. This saturation effect is shown clearly in Figure 6.7, which plots the peak temperature rise as a function of coolant flowrate for both 2mm and 6mm thermal test cells. Figure 6.7 shows that the thermal characteristics of the 2mm and 6mm cells with internal coolant flow are very similar to each other. All these experiments are carried out by passing a current of 1.5A through the heater coil in the thermal test cell.

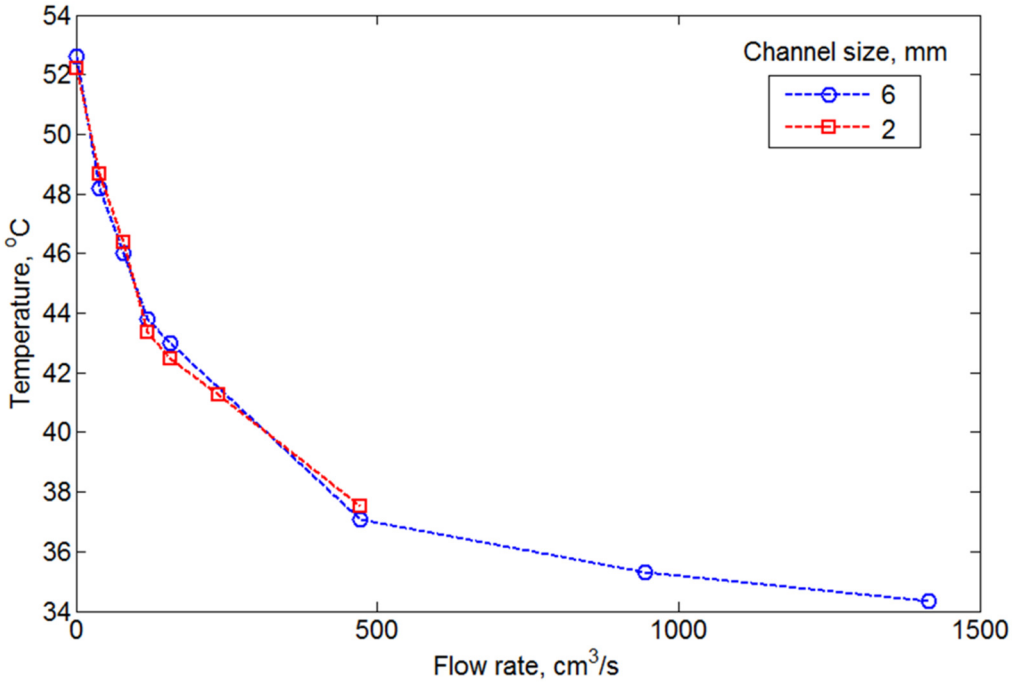

Figure 6.7. Maximum cell temperature as a function of internal flowrate for 2mm and 6mm cells.

6.4.3. Heat pipe and metal rod cooling

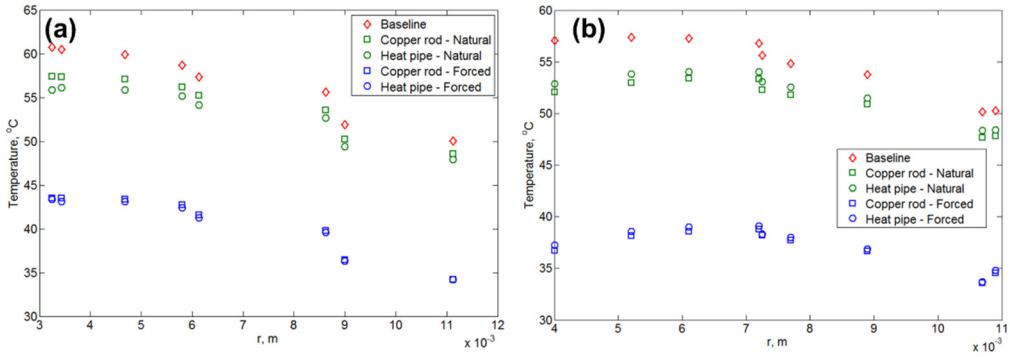

Figure 6.8. Temperature distribution within the cell for baseline, heat pipe and copper rod in two different convective conditions for (a) 2 mm and (b) 6 mm cell.

Results from experiments with embedded heat pipes are summarized in Figure 6.8, where the measured temperature distribution within the cell is plotted for a baseline case as well as with 2 mm (Figure 6.8a) and 6 mm (Figure 6.8b) heat

pipes. Two ambient conditions around the tip of the heat pipe are considered – one where the tip of the heat pipe loses heat simply by natural convection, and one where air flow over the top of the heat pipe (Figure 6.3) results in greater heat loss due to forced convective cooling. In addition to heat pipes, Figures 6.8(a) and 6.8(b) also show experimental data when a plain copper rod of the same size as the heat pipe is used instead. Data show significant reduction in temperature of the thermal test cell due to thermal transport from the core of the cell to the heat pipe. There is a reduction of 3 °C and 17 °C in peak temperature compared to baseline for natural and forced convection on the heat pipe respectively for the 6 mm case. These data show that while some temperature reduction is to be expected by simply embedding the heat pipe, an even greater benefit can be obtained when the tip of the heat pipe is cooled by forced convection. This is along expected lines, since forced convection ensures effective rejection of heat from the tip of the heat pipe into the ambient. In the absence of forced convection, heat flows from the cell into the heat pipe, but is severely impeded in transferring to the ambient, thereby reducing the overall heat transfer effectiveness of the heat pipe. The reduction in temperature within the cell for 6 mm and 2 mm heat pipes are summarized in Figure 6.9. Unlike flow-based cooling discussed in section 6.4.2, where thermal test cells with 2mm and 6mm inner tubes had similar thermal performance, in this case, there is greater temperature reduction when using a 6 mm heat pipe compared to a 2 mm heat pipe. However, a 6mm heat pipe occupies greater volume inside the cell, and thus may result in reduced capacity compared to the 2mm heat pipe cell. Data presented here

helps quantify such thermal-electrochemical trade-offs in the thermal management of a Li-ion cell.

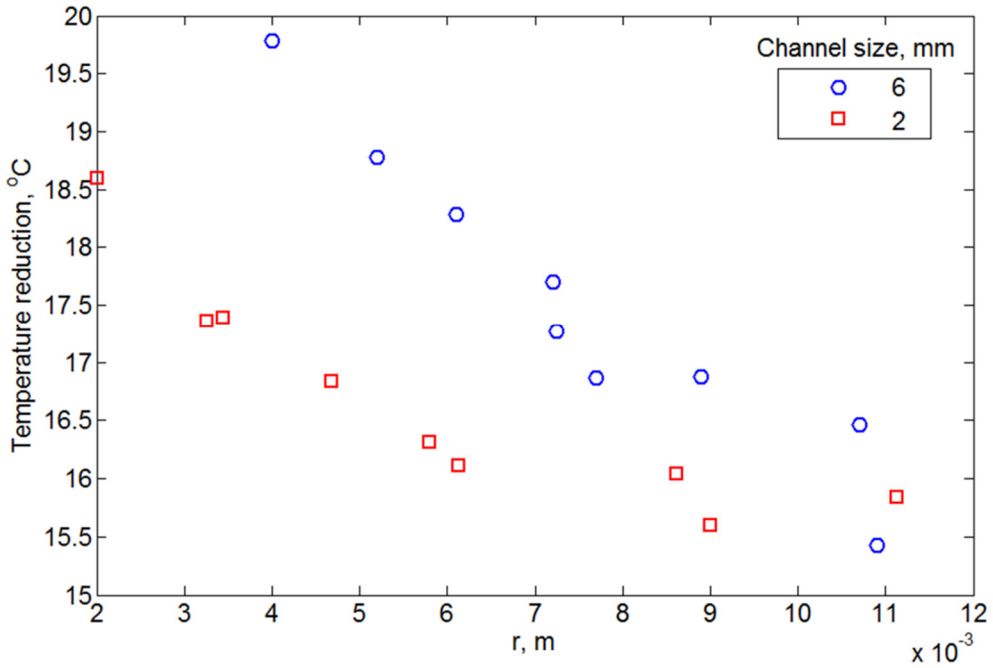

Figure 6.9. Comparison of thermal performance of 2 mm and 6 mm heat pipes.

Data presented in Figures 6.8(a) and 6.8(b) indicate that a cooling effect similar to a heat pipe may be obtained by simply using a copper rod instead of a heat pipe. In each case, the measured temperature distribution with a copper rod is very close to that with a heat pipe of the same size. Theoretically, this occurs because the thermal conductance through the metal rod is already so high that further increase in thermal conductance brought about by two-phase cooling within the heat pipe has negligible impact on the temperature field which is now dominated by thermal conduction within the cell and convection from the heat pipe or metal rod to the ambient. Note that a metal rod is expected to be of much lower cost, since it does not require a hollow tube and the incorporation of various heat pipe

components such as heat pipe fluid, wicking structure, etc. While 2 mm diameter copper rod can be obtained very easily and at low cost, a 2 mm diameter heat pipe be prohibitively expensive.

In addition to reduced peak temperature, the presence of the heat pipe or metal rod improves temperature uniformity within the thermal test cell. As shown in Figures 6.8(a) and 6.8(b), the temperature distribution is much flatter for both 2mm and 6mm cases compared to respective baselines, particularly when forced convection cooling is present.

Both heat pipe and metal rod, when embedded in the core of the cell as shown here provide a low thermal resistance path for heat generated in the cell to dissipate to the ambient. Despite a heat pipe being significantly more expensive than a metal rod, results presented here show that the thermal effect is similar in the two cases. In addition, while the 6 mm heat pipe shows better thermal performance than a 2 mm heat pipe, the 6 mm heat pipe occupies more space inside the cell, and thus may cause greater reduction in cell capacity for the same outer cell volume (around 20% reduction vs. 2% reduction based on volume).

Table 6.1. Comparison of experimental measurements and simulation results for temperature rise in °C in various cooling cases.

	No Cooling	Air Cooling			Heat Pipe or Cu Rod	
		157 cm^3/s	236 cm^3/s	472 cm^3/s	Natural Convection	Forced Convection
Experimental Measurement	52.4	33.6	31.4	30.2	52.1	36.7
Simulation Result	53.5	33.0	30.9	30.1	48.8	38.3

Table 6.1 shows a comparison of experimentally measured temperature rise at the inner-most thermocouple in the cell with finite element simulation results. Results for a number of cooling conditions are listed, including the baseline case, air cooling cases and forced and natural convection cases for a heat pipe. There is good agreement between experiments measurements and simulations in each case. Note that similar to experiments, the simulations results predict that thermal performance of heat pipe and metal rod are close to each other. This is because in each case, thermal transport becomes limited by convection at the tip due to the comparatively lower thermal resistance within the heat pipe or metal rod. This may be an important consideration in the design of a thermal management technique for a Li-ion cell.

6.4.5. Effect of heat pipe cooling on anomalous heat generation

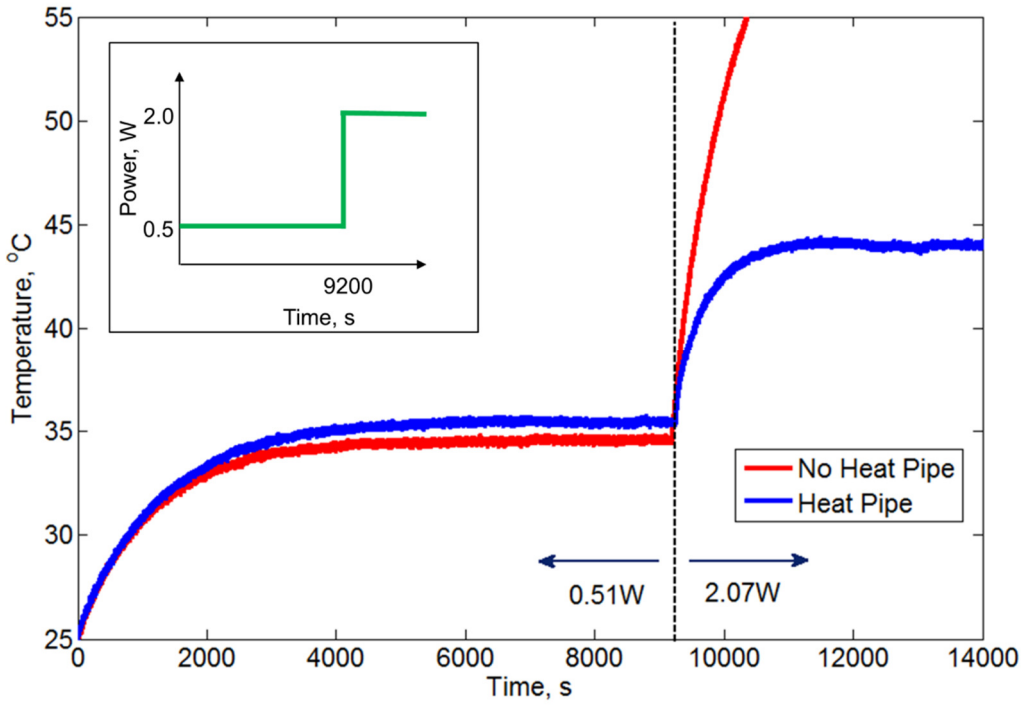

Figure 6.10. Comparison of thermal performance without and with heat pipe during an anomalous heat generation event, showing preventing of overheating by the heat pipe.

Experiments are also carried out to demonstrate the effect of the embedded heat pipe on the transient thermal response of the cell in realistic conditions. The cell is first subjected to a fixed heat generation rate, which is then increased four-folds. This may be representative of a situation where the cell experiences an anomalous increase in heat generation rate due to a malfunction such as an internal short. The thermal response of the cell is very critical in this situation, since thermal runaway may occur if the cell temperature exceeds a certain threshold. The presence of an embedded heat pipe may be able to prevent such a situation by directly removing the additional heat being generated in the core of the cell to the

ambient. In order to quantify this, experiments are carried out without and with the embedded heat pipe. Results are summarized in Figure 6.10, where the measured peak temperature is plotted as a function of time for both cases. Variation in the cell power with time is shown in the inset, and the time at which anomalous heat generation commences is indicated. When no heat pipe is present, the peak temperature in the cell starts increasing sharply as soon as the increased power is applied to the cell. The cell temperature rapidly reaches the threshold of 55 °C, at which point the experiment is terminated for safety of the cell. On the other hand, when a heat pipe is present, the temperature of the cell increases at a much lower rate, and eventually reaches a steady-state without exceeding the safety threshold. This shows that the heat pipe successfully prevents overheating of the cell, whereas without the heat pipe, the cell temperature rapidly reaches a threshold where it may be at risk of thermal runaway. This experiment highlights the potential thermal benefit of the presence of an embedded heat pipe in ensuring the safety of a cell during an anomalous heat generation event.

CHAPTER 7

EXPERIMENTAL AND THEORETICAL ANALYSIS OF A METHOD TO PREDICT THERMAL RUNAWAY IN LI-ION CELLS

Shah, K., Chalise, D., & Jain, A. (2016). Experimental and theoretical analysis of a method to predict thermal runaway in Li-ion cells. Journal of Power Sources, 330, 167-174.

Abstract

Thermal runaway is a well-known safety concern in Li-ion cells. Methods to predict and prevent thermal runaway are critically needed for enhanced safety and performance. While much work has been done on understanding the kinetics of various heat generation processes during thermal runaway, relatively lesser work exists on understanding how heat removal from the cell influences thermal runaway. Through a unified analysis of heat generation and heat removal, this paper derives and experimentally validates a non-dimensional parameter whose value governs whether or not thermal runaway will occur in a Li-ion cell. The parameter comprises contributions from thermal transport within and outside the cell, as well as the temperature dependence of heat generation rate. Experimental data using a 26650 thermal test cell are in good agreement with the model, and demonstrate the dependence of thermal runaway on various thermal transport and heat generation parameters. This parameter is used to predict the thermal design space in which the cell will or will not experience thermal runaway. By combining all thermal processes contributing to thermal runaway in a single parameter, this work contributes towards a unified understanding of thermal runaway, and provides the fundamental basis for design tools for safe, high-performance Li-ion batteries.

Keywords: Lithium Ion Battery, Safety, Thermal Runaway, Battery Cooling, Thermal Modeling.

7.1 Mathematical Modeling

Consider a cylindrical Li-ion cell of radius R, radial thermal conductivity k_r, heat capacity C_p and mass density ρ. The cell experiences a temperature-dependent internal heat generation rate $Q(T)$, and is being cooled at the outside surface with a convective heat transfer h due to a mechanism such as coolant flow. The interest is in determining the parameter space within which the cell will not undergo thermal runaway, i.e. the cell temperature does not become unbounded. In this case, the governing energy equation for the temperature rise $T(r,t)$ in the cell is given by

$$k_r\left(\frac{\partial^2 T}{\partial r^2}+\frac{1}{r}\frac{\partial T}{\partial r}\right)+Q(T)=\rho\cdot C_p\frac{\partial T}{\partial t} \tag{122}$$

subject to

$$\frac{\partial T}{\partial r}=0 \qquad \text{at } r=0 \tag{123}$$

and

$$k_r\left(\frac{\partial T}{\partial r}\right)=h\cdot T \qquad \text{at } r=R \tag{124}$$

Equations (122)-(124) can be solved to determine if there is a set of conditions that will prevent thermal runaway by ensuring a bounded solution for T at all times. To do so, a Taylor series expansion of $Q(T)$ is first carried out about a temperature $T=T_0$, and second order and higher terms are neglected. This results in

$$k_r\left(\frac{\partial^2 T}{\partial r^2}+\frac{1}{r}\frac{\partial T}{\partial r}\right)+Q(T_0)+\beta\left(T-T_0\right)=\rho C_p\frac{\partial T}{\partial t} \tag{125}$$

where $\beta=\dfrac{dQ}{dT}$ is the slope of $Q(T)$.

In order to solve equation (125), it is noted that the heat generation term can be split linearly into two components, $(Q(T_0)-\beta T_0)$ and βT. The first component is a constant quantity, which from thermal conduction theory [66] is known to result in a steady state with a bounded temperature field. However, the second heat generation component βT increases with temperature, and may lead to an unbounded temperature. Solving only for $T_2(r,t)$, which represents the temperature rise due to the second component of heat generation, it can be shown using the technique of separation of variables [66] that

$$T_2(r,t)=\sum_{n=1}^{\infty} C_n J_0\left(\frac{\mu_n r}{R}\right)\cdot\exp\left(\frac{k_r}{\rho\cdot C_p}\left(\frac{\beta}{k_r}-\frac{\mu_n^2}{R^2}\right)\cdot t\right) \tag{126}$$

where J_0 is the Bessel function of the first kind of order 0, C_n are constant coefficients, and μ_n are non-dimensional eigenvalues given by the roots of the equation

$$\mathrm{Bi}\cdot \mathrm{J}_0(\mathrm{x})-\mathrm{xJ}_1(\mathrm{x})=0 \tag{127}$$

where $Bi=\frac{hR}{k_r}$ is the Biot number. Note that C_n in equation (126) are obtained using orthogonality and the initial condition of the temperature field.

The temperature solution in equation (126) may be either bounded or unbounded depending on the sign of the term within the exponential function in equation (126). This term remains bounded if

$$\frac{\beta}{k_r}-\frac{\mu_n^2}{R^2}<0 \tag{128}$$

for each n=1,2,3..

Since the values of μ_n increase with n, it is sufficient to require that the first eigenvalue μ_1 satisfies equation (128). This condition can be written in terms of a single non-dimensional parameter as

$$TRN \equiv \frac{\beta \cdot R^2}{k_r \mu_1^2} < 1 \tag{129}$$

Thus, a fundamental, non-dimensional parameter has been derived, which we denote as the Thermal Runaway Number (*TRN*), whose value must be less than one in order to prevent thermal runaway. Since this derivation is based on Taylor series expansion of $Q(T)$ at a specific temperature T_0, therefore equation (129) must be satisfied over the entire temperature range of operation to ensure that thermal runaway does not occur throughout.

The non-dimensional parameter *TRN* in equation (129) is a combination of properties of thermal transport within the cell (k_r), thermal transport from the cell surface to the outside (μ_1) and the kinetics of heat generation (β), as well as the cell geometry (R). These parameters combined in the manner shown in equation (129) determine whether thermal runaway occurs or not. Li-ion cell design and run-time thermal management must be carried out to either reduce the numerator or increase the denominator or both in equation (129).

The first eigenvalue μ_1 can be determined by solving the transcendental equation (127) once Biot number, comprising the cell radius, R, thermal conductivity, k, and outside convective heat transfer coefficient, h, is known. μ_1 is plotted as a function of the Biot number in Supplementary Figure 1. As *Bi* increases, μ_1 increases, but eventually saturates. This means that regardless of how strong

convective heat transfer outside the cell is, the value of μ_1 will at most be 2.403. Simply continuing to increase *Bi* does not necessarily improve the chances of preventing thermal runaway.

Note that equation (129) is derived by assuming the Li-ion cell to be an infinite cylinder, which for most cell geometries such as 18650 and 26650 cells is a reasonable assumption. If a cylinder of finite height *H* is modeled instead, equation (129) must include additional contributions from the axial eigenvalue as follows:

$$\frac{\beta R^2}{k_r\left(\mu_1^2+\lambda_1^2\left(\frac{R}{H}\right)^2\gamma^2\right)}<1 \tag{130}$$

where λ_1 is the first axial eigenvalue, determined based on convective conditions on the top and bottom surfaces, γ is the thermal conductivity ratio k_z/k_r, and *H/R* is the aspect ratio. As expected, for large aspect ratio, equation (130) reduces to the infinite cylinder result given by equation (129).

It's been shown by a theoretical derivation that if $Bi<<1$, i.e., thermal conduction within the cell is neglected and the entire cell is treated as a lumped thermal mass, as has been done in Semenov plots in previous papers [37,25], equation (129) reduces to the following simpler form:

$$\beta V < h \cdot A \tag{131}$$

which corresponds to the Semenov analysis presented in the past that treats the body as a lumped thermal mass. Equation (131) states simply that to prevent thermal runaway, the rate of heat generation must be lower than the rate of heat removal. However, this simplified condition is accurate only for a lumped thermal

mass because it does not account for thermal transport within the cell. By accounting for this, the model presented here generalizes the Semenov analysis, and offers a more realistic and accurate prediction of thermal behavior of a Li-ion cell.

The next section discusses experiments carried out on a 26650 thermal test cell to experimentally validate the model presented in this section. Results and discussion are presented in Section 4.

7.2 Experiments

Experimental investigation of the influence of *TRN* on thermal runaway presents several challenges. It is difficult to accurately control and measure heat generation rate in a Li-ion cell, particularly one that changes with temperature, as required for such experiments. Further, measurement of temperature inside the cell is not straightforward [39,42]. As a result, these experiments utilize a thermal test cell that mimics heat generation in a Li-ion cell and provides the capability of close control of temperature-dependent heat generation rate.

7.2.1. Fabrication of Thermal Test Cell

A thermal test cell is designed and built to closely mimic the thermal behavior of a 26650 Li-ion cell. The thermal test cell has similar geometry and thermal transport properties as a 26650 Li-ion cell. Heat generation in the thermal test cell occurs due to Joule heating in a wound resistive metal sheet, which makes it possible to measure and change the heat generation rate as a function of temperature by varying the heating current. A thin foil of 304 Stainless Steel and thickness 0.025 mm is first insulated by adhering Kapton tape on its surface. The

foil-Kapton sandwich is rolled around a thin rod to form a cylinder of height 65 mm and radius 13 mm. Seven T-type thermocouples are placed during the rolling process at different radii. Thin metal wires are soldered to the two ends of the foil to provide electrical access to the metal foil. The roll is then lowered inside an Aluminum casing of the same dimensions as a 26650 Li-ion cell, and the thin rod is carefully taken out. The heater and thermocouple wires are routed out of the casing. The remaining volume inside the casing is filled with uncured poly-dimethylsiloxane (PDMS), a commonly used electrically insulating soft polymer, followed by curing for 2 hours at 60 °C. PDMS filling is carried out in two steps in order to expel all air inside the test cell. Once filled with PDMS and cured, the test cell is sealed with an epoxy.

Measurement of thermal conductivity of the thermal test cell has been reported in a recent paper to be 0.25 W/mK [22] using an adiabatic radial heating method [22]. This value is close to that of a 26650 Li-ion cell [22,40].

7.2.2. Temperature-Dependent Heat Generation in Thermal Test Cell

Electrochemical processes in a Li-ion cell generate heat at a rate that

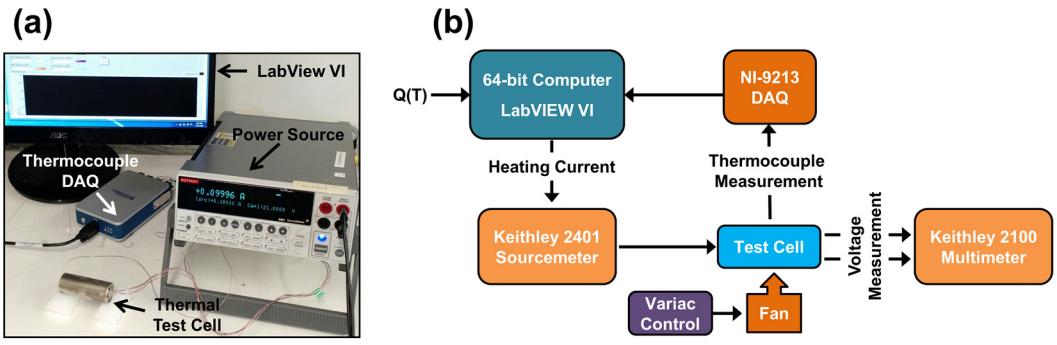

Figure 7.1. (a) Picture, and (b) Schematic of the experimental setup.

typically increases with temperature due to Arrhenius-type nature of these processes [9,13]. In order to obtain a similar temperature dependence of heat generation in the thermal test cell, the heating current, supplied by a LabView-controlled Keithley 2401 sourcemeter is modulated based on temperature measurement from the embedded thermocouples. Figure 7.1 shows a picture of the experimental setup, and a schematic of information flow between various instruments for control of the heat-generation rate. The thermocouple is read every one second, and the heating current is changed in order to maintain the heat generation rate according to any desired function of temperature.

It has been shown that the heat generation rate in the test cell remains close to the desired profile throughout the experiment, thereby demonstrating the capability of inducing a desired, temperature-dependent heat generation rate in the thermal test cell. Two specific temperature profiles investigated in this work include linearly and exponentially increasing heat generation as functions of temperature.

7.3 Results and discussion

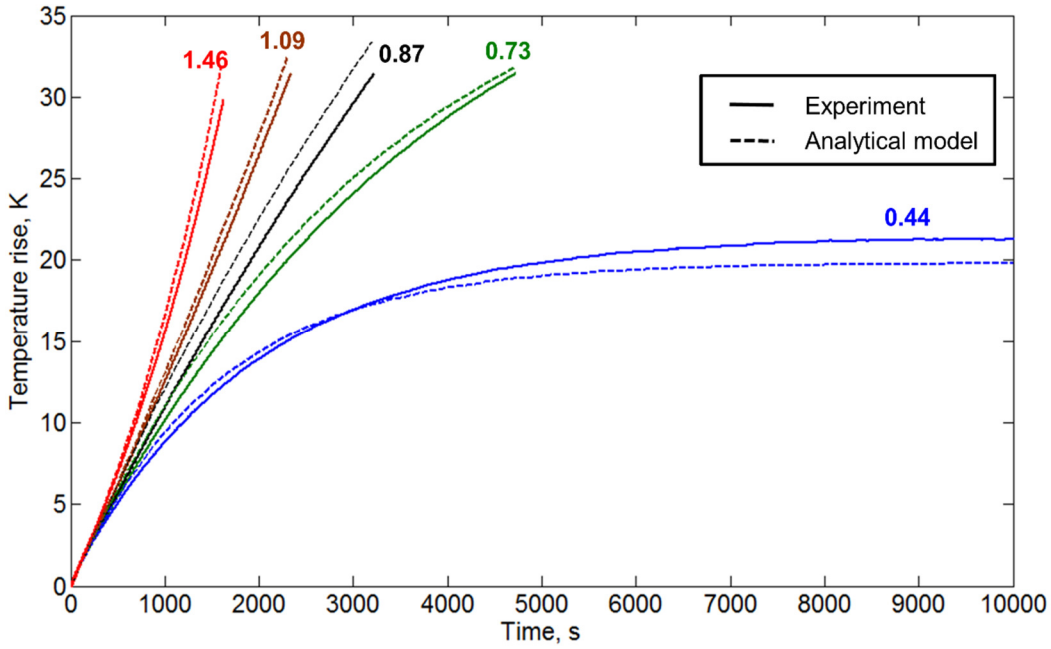

Figure 7.2. Core temperature of the thermal test cell measured as a function of time for a number of values of β, ranging from 805 W/m^{3}K for the left-most (blue) curve to 2685 W/m^{3}K for the rightmost (red) curve. These data show that thermal runaway occurs when $TRN>1$, and is prevented when $TRN<1$. The value of TRN is shown for each curve. Prediction of temperature profile from the analytical model in Section 2 is also shown for comparison

Figure 7.2 plots results from temperature measurements on the thermal test cell subjected to linearly increasing $Q(T)$, with different values of the slope β. Equation (129) predicts that as β increases, the value of TRN will increase, and eventually exceed the threshold value of 1, beyond which thermal runaway is expected to occur. This effect is clearly seen in Figure 7.2 where the value of TRN corresponding to various experiments is shown alongside each curve. For low TRN, the cell temperature remains bounded. As TRN increases, the temperature starts to increase due to increased heat generation, but still stays bounded. Once TRN exceeds 1, however, thermal runaway occurs, with the shape of the temperature

curve changing from concave to convex. Experimental data in Figure 7.2 demonstrate that runaway occurs beyond a threshold value of 1, as expected from the model. In addition, Figure 7.2 also shows that in each experiment, there is good agreement between experimental data and analytical model over the entire time period.

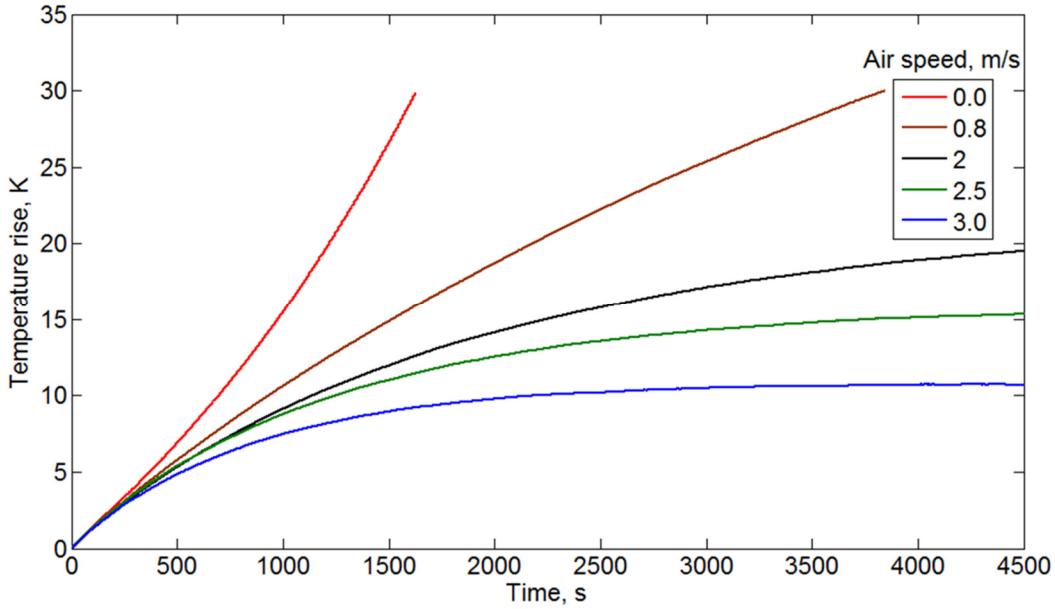

Figure 7.3. Core temperature of the thermal test cell measured as a function of time for fixed β and different convective heat transfer conditions.

As described in section 7.2, *TRN* includes contributions from heat generation rate (β), thermal conduction within the cell (k) as well as convective heat transfer on the outside (h). To investigate this further, experiments are carried out at fixed β and k, but with different cooling conditions on the outside surface of the cell to vary h. This is accomplished by providing a cooling fan to blow air over the fan and varying the cooling air speed. Figure 7.3 plots the temperature of the cell as a function of time for these experiments. As the air speed increases, so does h, resulting in reduction in the value of *TRN* according to equation (8). Eventually, as

TRN keeps reducing, as predicted by the model, the cell does not enter into thermal runaway, shown by the bottom three curves in Figure 7.3. These data further validate the theoretical prediction of a threshold value of *TRN* to induce thermal runaway in the cell.

A set of experiments is then carried out using an Arrhenius-type temperature dependence of the heat generation rate, which is more representative of physiochemical processes in a Li-ion cell that are responsible for thermal runaway. In general, the Arrhenius relationship for heat generation rate in a process is given by [94]

$$Q(T) = Q_0 \exp\left(-\frac{E_a}{RT}\right) \tag{132}$$

Where Q_0 is the pre-exponential constant, R is the ideal gas constant, and E_a is the activation energy. Note that due to the exponential relationship, β, the slope of Q is not constant, but increases with increasing temperature.

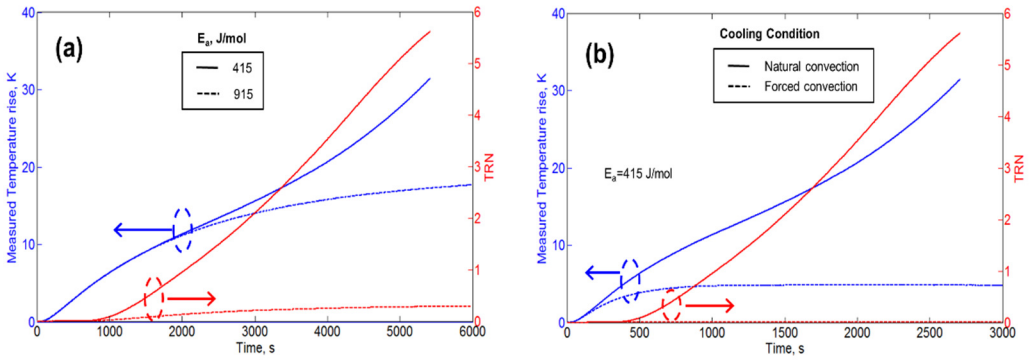

Figure 7.4. Experimental measurement of thermal test cell core temperature for (a) two different values of activation energy, Ea, (b) two different values of convective heat transfer coefficient. Plots also indicate the evolution of TRN with time, and show that thermal runaway occurs when TRN exceeds 1.

Two experiments are carried out at two different values of E_a. The values of E_a are chosen such that the resulting *TRN* corresponding to one of the E_a values crosses over the threshold within a specific temperature window, but not for the other. Figure 7.4(a) plots the measured temperature response as a function of time for both cases. As temperature increases, the heat generation rate increases exponentially, which results in a dynamic value of *TRN*. The variation in *TRN* as a function of time is also plotted in Figure 7.4(a), which shows that for the higher E_a case, *TRN* always stays under 1, and as a result, the measured temperature remains bounded. For the lower E_a case, *TRN* starts at a low value, but increases rapidly, and exceeds the threshold of 1 beyond around 1000s. During the time that *TRN* remains under 1, the temperature profile for this case also appears to remain bounded, but, as expected from the theoretical model, once *TRN* exceeds 1, the temperature distribution becomes unbounded, resulting in thermal runaway. There is an inflexion in the temperature curve at the time that *TRN* crosses the threshold value of 1. Figure 7.4(b) investigates this further by plotting the temperature profile for the lower E_a value at which thermal runaway occurred in the previous experiment, but with two different cooling conditions – natural convection and forced convection using a fan. Figure 7.4(b) shows that thermal runaway that occurred in the previous experiment could be prevented through external cooling, which increases the value of h, and hence reduce the value of *TRN*. Figure 7.4(b)

shows that when externally cooled, the value of TRN always stays below 1, thereby preventing thermal runaway as predicted by the model presented in section 2.

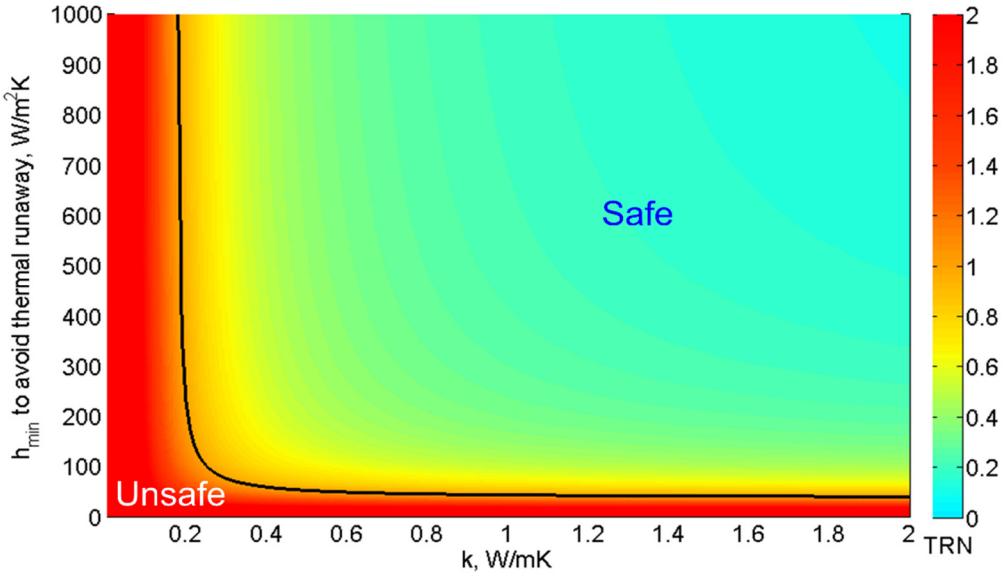

Figure 7.5**.** Colorplot of TRN in the h-k space. The TRN=1 curve that separates safe and unsafe regions is also shown.

For a Li-ion cell of a given chemistry and operating at a certain C-rate, there are two thermal transport parameters that influence the rate of heat removal from the cell – the thermal conductivity *k*, which governs the thermal conduction process within the cell, and convective heat transfer coefficient *h*, which governs heat removal from the cell surface to a coolant through thermal convection. It is important to understand how the value of *TRN* depends on these two parameters. Figure 7.5 shows a colorplot of *TRN* in the *h-k* space relevant for most practical cooling strategies for β=6000 W/m^{3}K. A curve corresponding to *TRN*=1, which is the threshold that separates the safe region (to the top and right of the *TRN*=1 curve) and unsafe region (to the bottom and left of the curve) of this space is also shown. This curve provides a useful design guideline for thermal management of Li-ion

cells by specifying what values of thermal transport parameters are expected to be sufficient to prevent thermal runaway at a given value of β. Further, in case thermal runaway is to be expected, this figure shows what parameters need to be changed and by how much in order to cross into the safe region of the *h*-*k* space shown in Figure 7.5. In general, the TRN=1 curve that separates the safe and unsafe regions shifts towards the top and right as β increases, leaving lesser and lesser of the *h*-*k* space in the safe region. For reference, recent measurements have reported the radial thermal conductivity of 26650 cells to be in the range of 0.2-0.65 W/mK [22,40]. On the *h* axis, natural convection cooling results in a value of *h* in the range of 10-100 W/m^{2}K [41], while forced convection values for *h* are larger, depending on the nature of coolant fluid and flow speed [41].

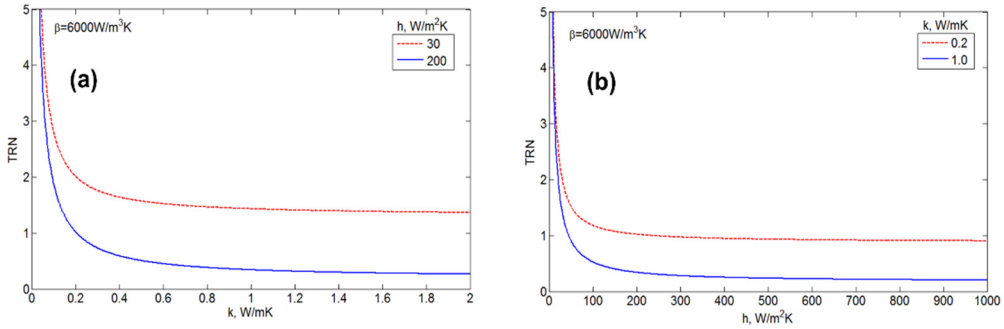

Figure 7.6. (a) TRN as a function of cell thermal conductivity, k for two different values of the convective heat transfer coefficient, h; (b) TRN as a function of the convective heat transfer coefficient, h for two different values of the cell thermal conductivity, k

Figures 7.6(a) and (b) plot TRN as a function of *h* and *k* respectively while the other parameter is fixed. Both figures use β=6000 W/m^{3}K. Figure 7.6(a) shows that at a fixed *k*=0.2 W/mK, *TRN* reduces as *h* increases, i.e., as the cell is cooled more and more aggressively, and dips below the threshold value of 1 at around *h*=233 W/m^{2}K. This transition can be made to occur at a lower *h*, if the thermal

conductivity of the cell could be improved. At k=1 W/mK, Figure 7.6(a) shows that a heat transfer coefficient of 45 W/m^{2}K is sufficient to prevent thermal runaway. Similarly, Figure 7.6(b) shows that increasing the cell thermal conductivity reduces *TRN* when h is held constant. Both Figures 7.6(a) and 7.6(b) exhibit a saturation effect in *TRN* as either h or k continue to increase. *TRN* for a cell with too low thermal conductivity might not dip below the threshold value of 1 at all regardless of how effectively it is cooled on the outside. Note that increasing h requires improved heat transfer external to the cell, whereas increasing k requires improving material and interfacial thermal resistances within the cell [48].

The interplay between h and k for reducing TRN and preventing thermal runaway is further illustrated in Supplementary Figure 1, which plots the first root μ_1 of equation (127) as a function of the Biot number, *Bi*. As *Bi* increases, there is a sharp increase in μ_1, resulting in significant benefit to *TRN*, but beyond a value of around 30, further increase in *Bi* does not significantly increase μ_1. This illustrates the inherent limitations in using convective cooling to improve thermal runaway performance of the cell, for which k is a constant. Once the heat transfer coefficient is somewhat large, its role in preventing thermal runaway saturates, and further benefit must come from thermal-friendly cell design, for example by improving thermal transport through materials and interfaces inside the cell.

When carrying out an effective thermal design of the cell to prevent thermal runaway, parameters such as cell radius and thermal conductivity of the cell are usually fixed, whereas the convective heat transfer coefficient can be increased somewhat, for example, by providing additional coolant flow on the outside of the

cell. In such a case, it is important to determine h_{min}, the minimum value of the convective heat transfer coefficient that can sustain a given heat generation rate without causing thermal runaway. Figure 7.7 plots h_{min} as a function of β for a number of values of the cell thermal conductivity, k. This plot shows that for a given value of k, as β increases, the minimum value of h needed to prevent thermal runaway increases slowly at first, but then very sharply, eventually becoming too large to be practicable. Since mu1 has a theoretical maximum value of 2.405 (see Suppl. Fig 3), therefore, for a given R and k, the maximum β that a cell can sustain without thermal runaway is given by $\beta_{max}=5.78 \cdot k/R^2$, which requires very strong convective cooling corresponding to a Biot number of around 50 or more. If the expected β of a cell is greater than β_{max}, then, even the best possible external cooling may not be effective.

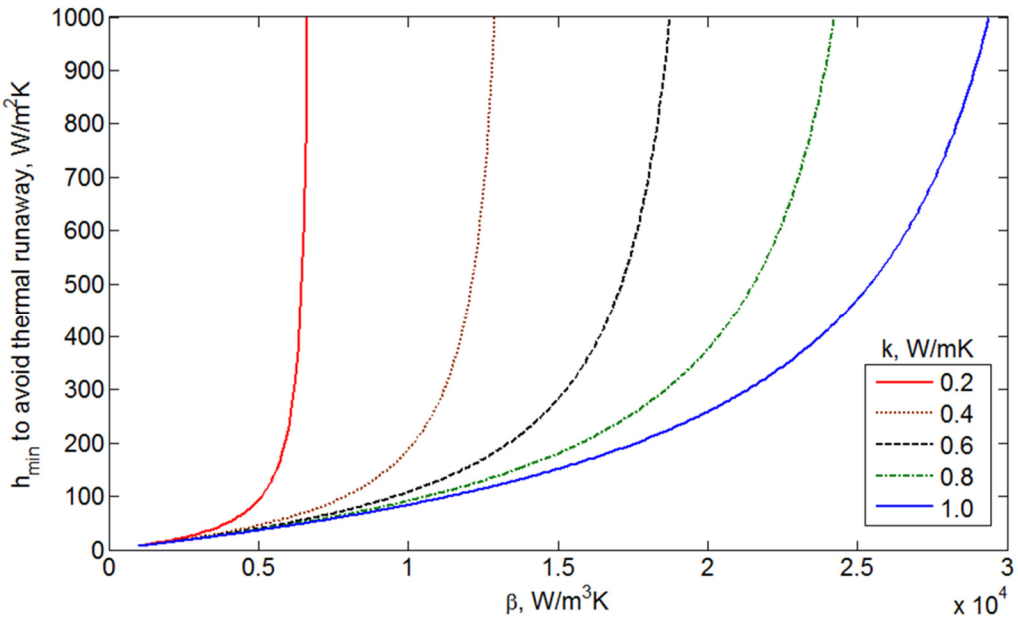

Figure 7.7. Minimum heat transfer coefficient needed to prevent thermal runaway as a function of β for different values of cell thermal conductivity.

Finally, the two-dimensional thermal runaway model is utilized to predict β_{max}, the maximum value of β that a cell can sustain as a function of the shape of the cell. Figure 7.8 plots β_{max} as a function of cell radius for fixed total volume, corresponding to the volume of a 26650 cell. As R increases, β_{max} first reduces, but then starts increasing after reaching a minima. This non-monotonic behavior occurs because for a fixed volume, equation (130) can be rearranged as follows:

$$\beta_{max} = \left(\frac{k_r \mu_1^2}{R^2} + \frac{\lambda_1^2 \gamma^2 \pi R^4}{V^2} \right) \tag{133}$$

where V is the volume.

The first term in equation (133) is inversely proportional to R^2, whereas the second term is directly proportional to R^4, which explains the non-monotonic behavior in Figure 7.8. This shows that among all cells of the same volume at given values of h and k, the cell of a certain radius sustains the lowest β_{max},

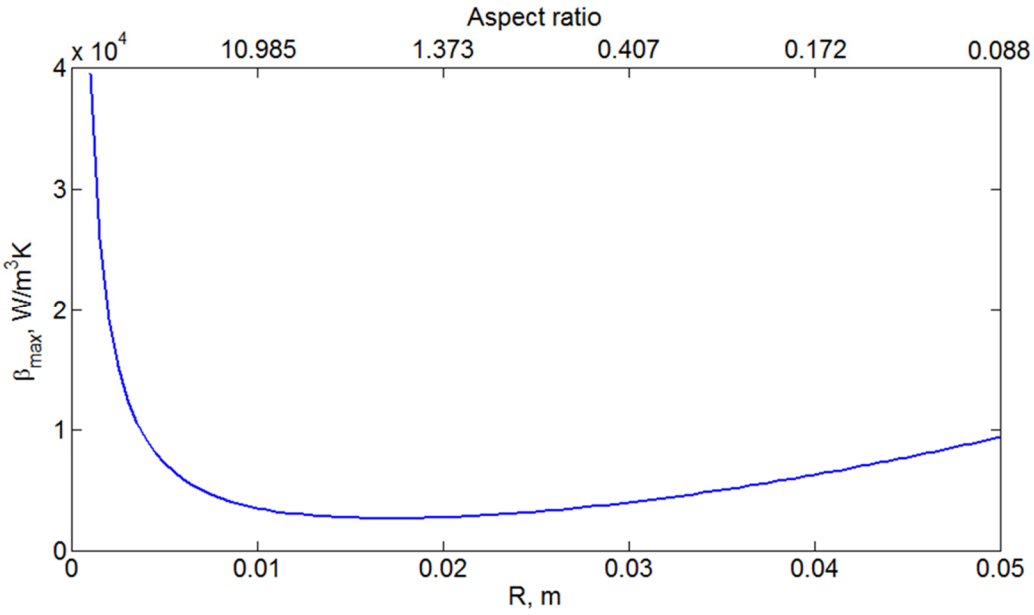

Figure 7.8. Maximum sustainable β as a function of the aspect ratio of a finite-length, cylindrical cell.

and thus has the worst possible thermal runaway behavior at the assumed values of h and k. This worst-case radius can be easily obtained by differentiating equation (133). For conditions considered here, as shown in Figure 7.8, this minima occurs at a radius of around 17 mm, which is quite close to that of the commonly used 26650 cell.

CHAPTER 8

AN EXPERIMENTALLY VALIDATED NON-LINEAR TRANSIENT THERMAL MODEL TO PREDICT THERMAL RUNAWAY IN CYLINDRICAL LI-ION CELLS

Abstract

Thermal runaway is a widely investigated safety concern in Li-ion based energy storage devices. Model to predict temperature and help prevent thermal runaway is critically needed for improved safety as well design considerations. Significant amount work has been done on understanding the kinetics of electrochemical reactions responsible for heat generation during thermal runaway, the effect of those reactions on the core temperature of cell and prediction of thermal runaway has not been investigated as much. A Thermal model capable of accounting for various heat generation mechanisms and the resulting temperature dependent heat generation has been demonstrated. Such a model can prove to be key in improving the ability to predict the catastrophic event of thermal runaway in Li-ion cell. The model has been rigorously validated experimentally. Controllable temperature dependent heat generation has been obtained by simulating the required temperature dependent nature in a thermal test cell. Experimental measurement of the temperature has been obtained by varying value of various parameters of heat generation. There is good agreement between the experimental data and prediction from thermal model for different values of various heat generation parameters. The model is also used to analyze effect of different heat generation terms and heat transfer parameters such as thermal conductivity and convective heat transfer coefficient on the temperature of the cell. The model has also demonstrated the capability to simulate effect of thermal abuse of Li-ion cell.

Keywords: Lithium Ion Battery, Safety, Thermal Runaway, Battery Cooling, Thermal Modeling.

8.1. Mathematical Modeling

Consider a cylindrical Li-ion cell of radius R, radial thermal conductivity k_r and radial thermal diffusivity α_r. The cell experiences internal heat generation due to Ohmic Joule heating (Q_J) and exothermic reactions (Q_e), and is being cooled at the outside surface with a convective heat transfer coefficient h. The interest is in predicting the temperature distribution in the cell as a function of time, and specifically, predict whether the cell enters thermal runaway. The mathematical modeling of this problem is inherently challenging due to the temperature-dependent heat generation from the exothermic electrochemical reactions. This makes the governing energy equations non-linear. The governing energy equation for the temperature rise $\theta(r,t)$ in the cell is given by

$$\left(\frac{\partial^2\theta}{\partial r^2}+\frac{1}{r}\frac{\partial\theta}{\partial r}\right)+\frac{Q_J+Q_e}{k_r}=\frac{1}{\alpha_r}\frac{\partial\theta}{\partial t} \tag{134}$$

subject to

$$\frac{\partial\theta}{\partial r}=0 \qquad \text{at } r=0 \tag{135}$$

and

$$-k_r\left(\frac{\partial\theta}{\partial r}\right)=h\cdot\theta \qquad \text{at } r=R \tag{136}$$

$$\theta=\theta_i \qquad \text{at } t=t_i \tag{137}$$

$$\theta=T-T_\infty \tag{138}$$

where T and T_∞ are absolute temperatures of the cell and ambient respectively.

Note that while Q_J is a constant, Qe depends on the local absolute temperature. In order to solve equations (134)-(137), a piecewise linear approximation of $Q_e(T)$ based on Taylor series expansion is utilized. The above governing equation is then simplified (note that it is not linearly varying heat generation yet since beta is temperature dependent – it becomes linear only after discretization in time.. see my comment below) as follows:

$$k_r\left(\frac{\partial^2\theta}{\partial r^2}+\frac{1}{r}\frac{\partial\theta}{\partial r}\right)+\frac{Q_J^*}{k_r}+\frac{\beta(T)\cdot T}{k_r}=\rho C_p\frac{\partial\theta}{\partial t} \tag{139}$$

where β(T) is the instantaneous slope of heat generation with respect to absolute temperature

In order to solve equation (139), it is noted that the total heat generation is split into two components – $Q_{joule\text{-}heating}$ and β(T)·T. Here the second terms β(T)·T captures heat generation due to exothermic electrochemical reactions. The first component is due to joule heating which can be considered as a constant with a temperature, and from thermal conduction theory [66] would lead to a steady state with a bounded temperature field. However, the second heat generation component β(T)·T increases with temperature, and may lead to an unbounded temperature. The reaction rate of exothermic electrochemical reactions increases exponentially with increase in temperature which leads to exponential increase in heat generation with temperature in Li-ion cells.

$$\theta(r,t)=s_i(r)+w_i(r,t) \tag{140}$$

$$s_i(r) = \frac{h \cdot Q_J^* \cdot J_0\left(\sqrt{\frac{\beta_i}{k}} r\right)}{\beta_i\left(k\sqrt{\frac{\beta_i}{k}} \cdot J_1\left(\sqrt{\frac{\beta_i}{k}} R\right) + h \cdot J_0\left(\sqrt{\frac{\beta_i}{k}} R\right)\right)} - \frac{Q_J^*}{\beta_i} \tag{141}$$

$$w_i(r,t) = \sum_{n=1}^{\infty} C_n(\beta_i) J_0\left(\frac{\mu_n r}{R}\right) \cdot e^{\alpha\left(\frac{\beta_i}{k} - \frac{\mu_n^2}{R^2}\right)t} \tag{142}$$

The above solution is for a constant value of β_i.

where J_0 is the Bessel function of the first kind of order 0, C_n are constant coefficients, and μ_n are non-dimensional eigenvalues given by the roots of the equation

$$Bi \cdot J_0(x) - xJ_1(x) = 0 \tag{143}$$

where $Bi = \frac{hR}{k_r}$ is the Biot number. Note that $C_n(\beta_i)$ in equation (5) are obtained using orthogonality and the initial condition of the temperature field for the corresponding β_i. The above solution is implemented such that the heat generation from piecewise linear approximation at a given temperature is within a certain tolerance of the actual heat generation values. In order to ensure that, value of β is updated to instantaneous slope value as required. Every time β is changed in order to obtain the piecewise linear approximation, coefficients C_n are recalculated as given below,

$$C_n(\beta_i) = \frac{\int_0^R \left(-s_i(r) + s_{i-1}(r) + \sum_{n=1}^{\infty} C_n(\beta_{i-1}) J_0\left(\frac{\mu_n r}{R}\right) \cdot e^{\alpha\left(\frac{\beta_{i-1}}{k} - \frac{\mu_n^2}{R^2}\right)t_i} \right) \cdot r \cdot J_0\left(\frac{\mu_n r}{R}\right) dr}{\int_0^R r \cdot J_0^2\left(\frac{\mu_n r}{R}\right) \cdot dr} \quad (144)$$

The next section discusses experiments carried out on a 26650 thermal test cell to experimentally validate the model presented in this section. Results and discussion are presented in Section 4.

8.2. Experiments

Experimental validation of any analytical thermal model for a Li-ion cell in thermal runaway conditions presents several challenges. Accurate measurement and control of heat generation rate and its variation with temperature in real time is not straightforward. Heat generation in abuse conditions in a Li-ion cell occurs due to a variety of decomposition processes. Even though several papers have estimated the reaction kinetics of these processes [8,13,95], the heat generation rates are not known exactly, and may vary depending on experimental conditions. Further, temperature measurement inside a Li-ion cell during abuse conditions is also not straightforward. Most past research on temperature measurement in a Li-ion cell is limited to the surface temperature [25,34,96] whereas thermal runaway most likely originates the core of the cell where the temperature is the highest.

In order to overcome these experimental difficulties, a thermal test cell is used for model validation. This thermal test cell closely mimics the geometry and thermal properties of a 26650 Li-ion cell while enabling the capability of close

control of temperature-dependent heat generation rate and temperature measurement.

8.2.1. Fabrication of Thermal Test Cell

The design and fabrication of a thermal test cell used in this work have been described in section 7.2. In brief, the thermal test cell comprises a tightly wound roll of thin metal foil in 26650 stainless steel casing. First, a thin metal foil of thickness 0.025 mm is insulated by adhering Kapton tape on both sides, and then wrapped around a thin rod to form a roll with radius and height very close to that of a 26650 Li-ion cell. Seven T-type thermocouples are placed at different lengths on the metal foil, which results in thermocouples at different radii after rolling. To make electrical connection to the metal foil roll, thin metal wires are soldered to the two ends of the metal foil. The roll is then inserted into an Aluminum casing usually used for a 26650 Li-ion cell. The thin rod used for rolling is carefully removed from the casing. A hole is made in the cap of the casing, through which the heater and thermocouple wires are routed out. In order to fill up air voids inside the cell, it is filled with uncured poly-dimethylsiloxane (PDMS), a commonly used electrically insulating soft polymer. PDMS is then cured for 2 hours at 60 °C. PDMS filling is carried out in two steps in order to completely expel out all air inside the cell. Finally, the test cell is sealed by putting the cap on and securing it with an epoxy.

Radial thermal conductivity of a thermal test cell fabricated using this process has been reported in a recent paper to be 0.25 W/mK [22], measured using an adiabatic radial heating method [22]. This value is close to that of a 26650 Li-ion cell [22,40].

8.2.2. Experiments for Temperature-Dependent Heat Generation in Thermal Test Cell

Experiments are carried out to mimic temperature-dependent heat generation in the thermal test cell, similar to what would happen in a Li-ion cell. The experimental setup, and the mechanism to simulate temperature dependent heat generation behavior is as described in section 7.2. Electrical current is passed through the metal foil of the thermal test cell using a Keithley 2401 sourcemeter to produce Joule heating. Since the heat generation rate is expected to increase with temperature, for example, according to an Arrhenius relationship, the amount of current passing through the thermal test cell is increased as the cell temperature increases. This is accomplished by temperature measurement through embedded thermocouples using a NI cDAQ 9213 data acquisition unit controlled by LabView software running on a 64-bit computer, followed by changes in the current sourced from the Keithley 2401 sourcemeter, which is also controlled by LabView. The software uses the measured temperature as input to determine the required electrical current every one second according to any desired Q(T) relationship. Through this approach, any desired temperature-dependent heat generation, similar to exothermic reactions responsible for thermal runaway in a Li-ion cell, can be imposed on the thermal test cell.

8.3. Results and discussion

8.3.1. Experimental Validation

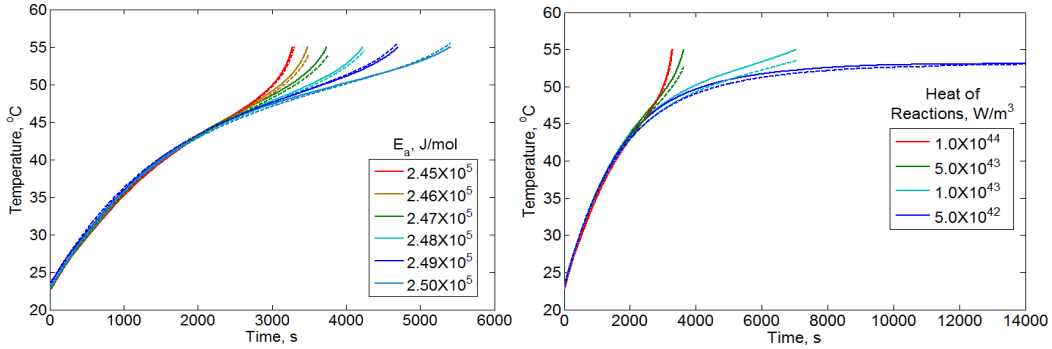

Figure 8.1 Experimental validation for (a) different activation energy(E_a) values (b) different values of heat of reactions (Q_0)

Figures 8.1(a) and (b) present experimental validation of the analytical thermal model discussed in Section 8.1. The two key Arrhenius parameters that govern temperature dependent heat generation during thermal runaway in a Li-ion cell are the activation energy, E_a and pre-exponential constant, Q_0. Experiments are carried out to measure temperature rise in the thermal test cell for different values of both of these parameters and compare against predictions from the analytical thermal model. Figure 8.1(a) presents this comparison for different values of activation energy E_a while Q0 remains fixed. There is very good agreement between measurements and analytical model across multiple values of Ea. Similarly, Figure 8.1(b) presents results when Q_0 is varied while holding Ea constant.. Similar to Figure 8.1(a), there is good agreement across the entire range of variations investigated here. Note that the values of thermal conductivity and heat capacity for the analytical model are taken from past measurement on a similar thermal test cell to be 0.2 W/mK and 777 J/kgK respectively. A value of 10.5 W/m^2K is used

for the convective heat transfer coefficient, which is within the limits of typical value of this parameter during natural convection.

8.3.2. Effect of Arrhenius parameters and Joule heating

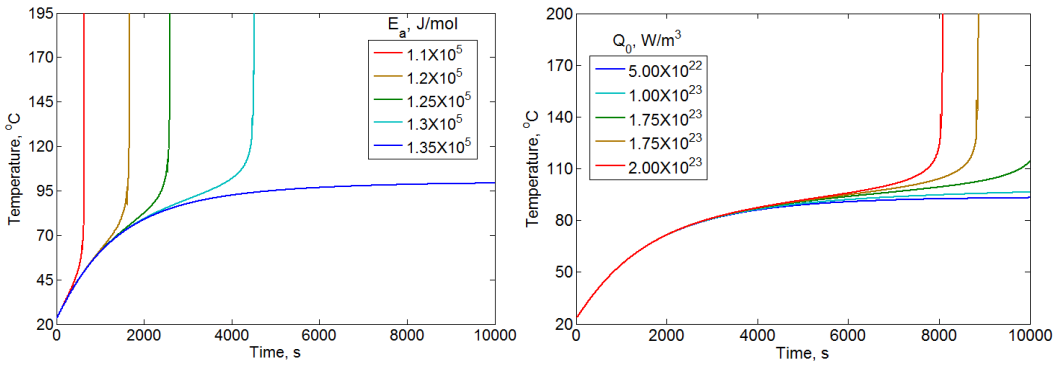

Figure 8.2 Computed Temperature for different (a) different activation energy(E_a) values (b) different values of heat of reactions (Q_0)

The experimentally validated analytical model is used to examine the effect of changing Arrhenius parameters E_a and Q_0 on temperature rise in a Li-ion cell.. Figure 8.2(a) presents predicted temperature rise as a function of time for different values of E_a while holding Q_0 constant at the value corresponding to SEI decomposition reaction [95], which is one of the early decomposition reactions responsible for the onset of thermal runaway. Joule heating component of heat generation is set to 3W. Figure 8.2(a) shows that even relatively minor changes in E_a drastically change the thermal behavior of the cell. There appears to be a threshold value of E_a, below which, the cell temperature becomes unbounded and thermal runaway occurs. Figure 8.2(a) also shows that E_a also influences when the cell goes into thermal runaway. At lower E_a, cell temperature becomes unbounded at a much earlier time than at a larger value. The effect of change in Q_0 on the thermal behavior of the cell is shown in Figure 8.2(b). Unlike Ea, a significant

reduction in Q_0 is required to change the temperature from becoming unbonded to bounded. Further, changes in Q_0 do not significantly affect the time taken for the cell to enter thermal runaway.

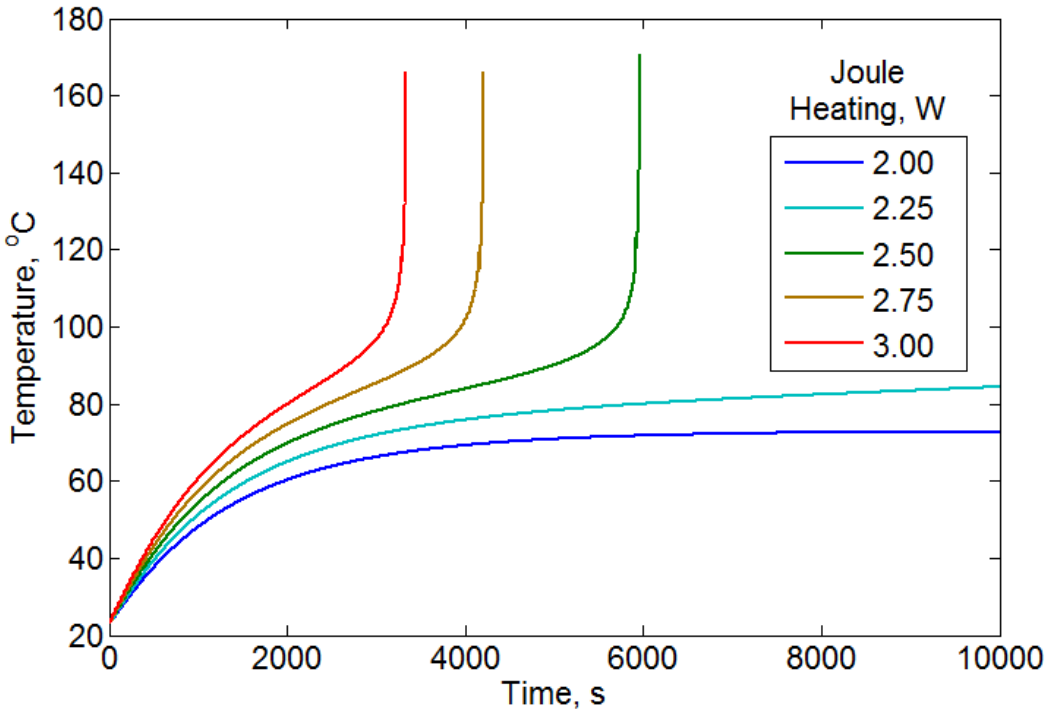

Figure 8.3 Computed Temperature for different joule heating rate

Joule heating is the key contributor to total heat generation in Li-ion cells during nominal, non-runaway operation. Since Joule heating is largely temperature-independent, the corresponding temperature rise is bounded. However, temperature rise resulting from Joule heating may activate other electrochemical reactions governed by Arrhenius kinetics, for which heat generation rate rises with temperature, thereby causing thermal runaway. Threshold temperature for such reactions are well known [13, 95]. Figure 8.3 plots temperature rise as a function of time for different values of Joule heating based heat generation rate. E_a and Q_0

values corresponding to SEI decomposition reaction are used. Figure 8.3 shows that Joule heating of more than 2.5W causes the cell to enter thermal runaway. This happens primarily because at 2.5W or higher, the temperature rise, although bounded, is large enough to trigger significant Arrhenius heat generation, which increases with increasing temperature, thereby causing thermal runaway.

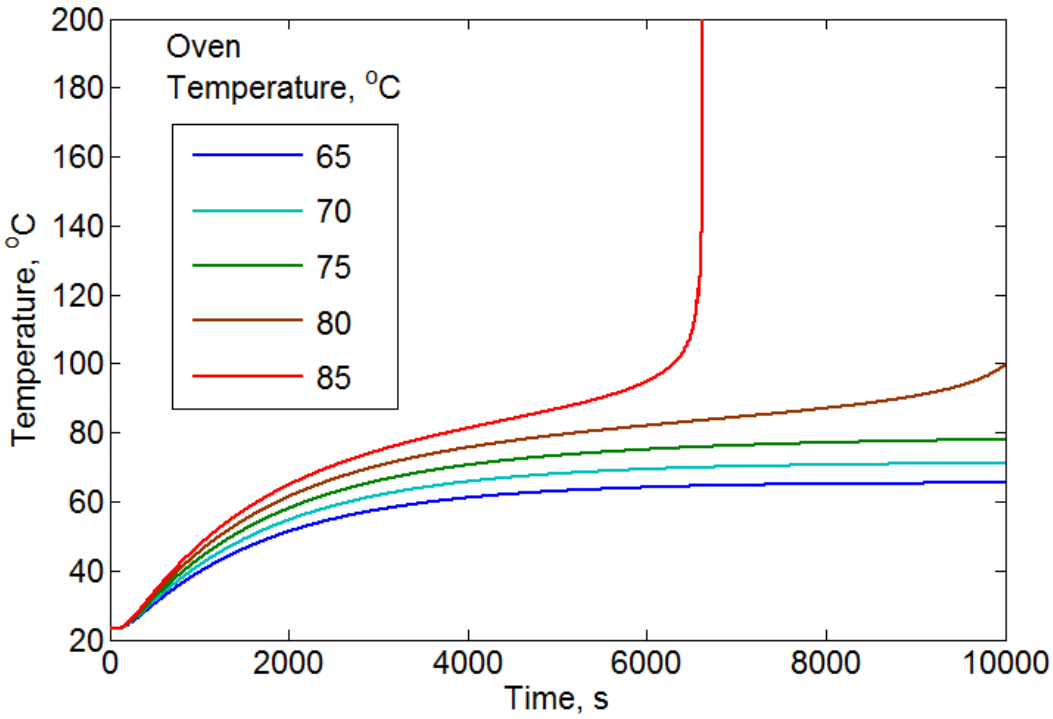

Figure 8.4 Computed Temperature for different oven temperature

The thermal model can also be utilized to predict temperature during oven tests that are commonly used to mimic thermal abuse condition for Li-ion cells and study thermal runaway phenomena. Figure 8.4 presents temperature rise as a function of time for different ambient temperature under natural convection conditions. Heat generation parameters for SEI decomposition, along with 3W Joule heating is used. Figure 5 shows that temperature appears to stay bounded until about 75 ºC ambient temperature. Beyond around 85 ºC, temperature becomes

unbounded, making thermal runaway imminent. The existence of such a sharp threshold for the ambient temperature, at which thermal runaway behavior is suddenly triggered is consistent with experimental observations [32, 96]

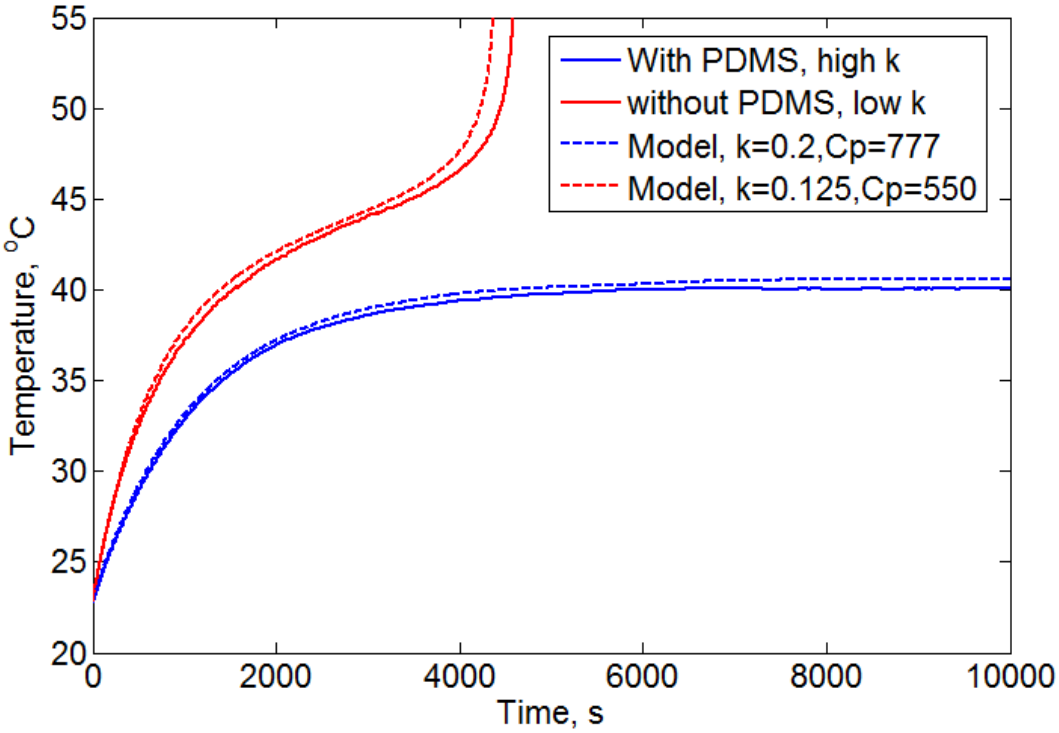

Figure 8.5 Experimentally measured and theoretically computed temperature of thermal test cells with different thermal conductivity

Effect of heat transfer parameters on thermal behavior of a Li-ion cell is investigated next. Figure 8.5 presents experimental measurements where temperature-dependent heat generation is mimicked in two different thermal test cells. These cells, labeled A and B differ slightly in their construction. While cell A has PDMS poured in during its fabrication, cell B does not. Consequently, cell B has air voids inside the casing, resulting in significantly lower thermal conductivity compared to cell A. Figure 8.5, which plots temperature rise as a function of time when both cells are subjected to the same temperature-dependent heating, shows

dramatically different thermal behavior. While the higher thermal conductivity cell reaches a steady state temperature, the lower thermal conductivity cell does not. This highlights the critical importance of thermal conductivity of the cell in preventing thermal runaway, and is consistent with a recent paper that showed that thermal conductivity is one of the parameters that determines the value of the Thermal Runaway Number, the value of which governs whether thermal runaway occurs or not. The experimentally measured behavior has also been predicted by the theoretical model. Since the low thermal conductivity cell, cell B, doesn't have PDMS filling its voids, it has both lower heat capacity and thermal conductivity.

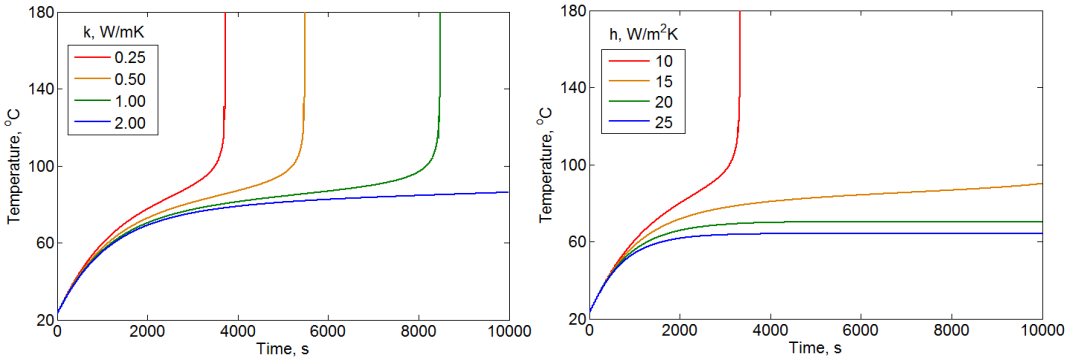

Figure 8.6 Effect of heat transfer parameters (a) different thermal conductivity values (k) (b) different convective heat transfer coefficient values (h)

Figure 8.6 (a) plots the effect of change in thermal conductivity on temperature rise as predicted by the analytical model. Temperature-dependent heat generation parameters for SEI decomposition reaction in a Li-ion cell under natural convection are used in these computations. This figure shows that a 4X increase in thermal conductivity changes the thermal behavior of the cell from being unbounded to bounded, thereby avoiding thermal runaway. A smaller increase in thermal conductivity may not help completely avoid thermal runaway, but may

delay the onset, thereby providing additional time in which steps could be taken to bring the cell back to safety.

Similarly, the effect of convective heat transfer coefficient has also been investigated using the thermal model. Using the same heat generation parameters as before, Figure 8.6 (b) plots temperature rise as a function of time for different values of the convective heat transfer coefficient. This figure shows very strong influence of convective heat transfer coefficient on the thermal behavior of the cell. For a given thermal conductivity, heat transfer rate is limited by convective heat transfer coefficient until the coefficient becomes large enough. A small increase in the convection coefficient increases overall heat dissipation capacity of the system, which enables the heat dissipation rate to match up to heat generation rate at a higher temperature. This results in the change in the thermal behavior of the cell from unbounded to bounded. Unlike the case of thermal conductivity, a certain minimum increase in convection coefficient leads to prevention of thermal runaway, but a smaller increase does not delay the onset of thermal runaway.

Thermal runaway in Li-ion cells is known to be caused by a cascade of exothermic electrochemical reactions that feed into another and ultimately cause thermal runaway. Figure 8.7 demonstrates the capability of the analytical model to account for complicated coupling between multiple temperature-dependent heat generation processes. Figure 8.7 plots temperature rise as a function of time for three distinct reactions individually as well as for a situation where all three reactions occur. Due to their high activation energies, Reaction B and Reaction C do not lead to thermal runaway on their own.

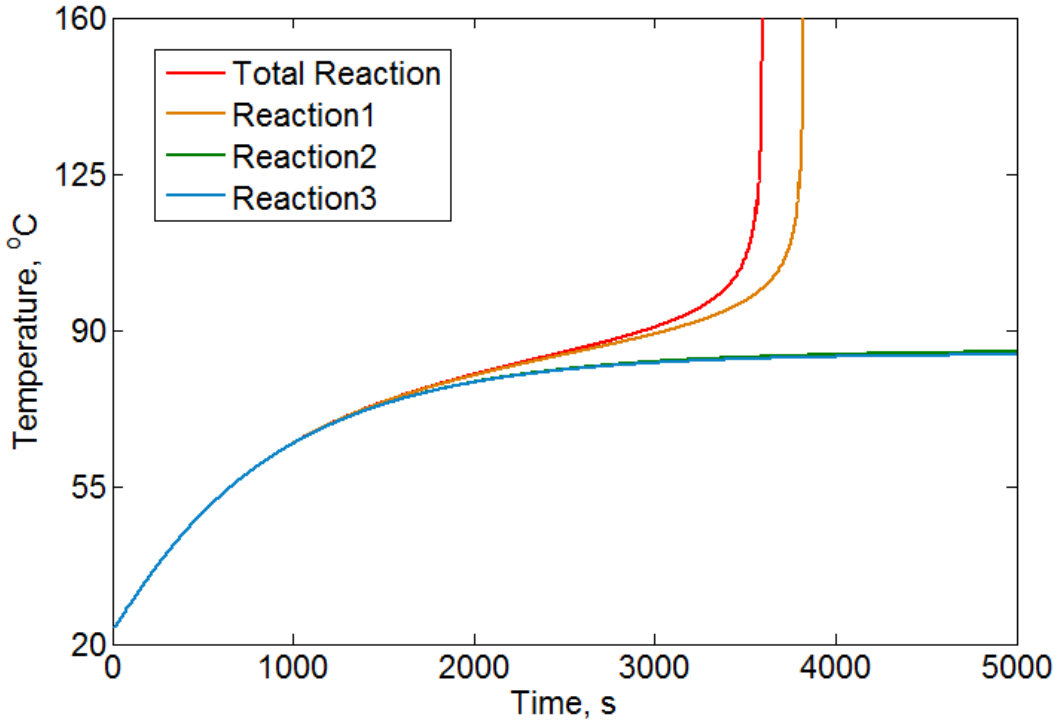

Figure 8.7 Temperature computed for individual reactions and the total of individual reactions

On the other hand, Reaction A leads to unbounded temperature due to its lower activation energy. When the total sum of all three reactions is implemented in the thermal model, Reaction A increases the temperature enough to activate Reaction B and Reaction C. This results in the temperature becoming unbounded earlier than in the case of Reaction A only. This signifies the importance of the cascading effect and the capability of the analytical model to account for the effects of cascading.

CONCLUSIONS

Chapter 1 and 2 present the analytical steady state and transient models for a cylindrical Li-ion cell. These models are capable of accurately predicting the temperature inside a cell and are versatile in handling space and time dependent heat generation rate. Experimental validation of these models is also provided. These models can go beyond their primary function of temperature prediction and provide guidelines in design and safe operation of batteries. They also help us to understand heat transfer inside a cell and give useful insights, which help in directing future research in this field.

In Chapter 3, an innovative conceptual design for Li-ion cell is analyzed by developing an analytical model. The proposed design consists of an axial fluidic channel passing through the core of the battery. This would enhance the cooling of the cell by effectively cooling its core at the cost of reduced storage capacity. The analytical model helps to quantify the gain in terms of reduced temperature rise or increased charge/discharge rate, without compromising the safety of the cell and compares it with reduction in battery capacity as a function of the channel size. The model and the analysis carried out can serve as a guide to design such a cell.

Chapter 5 provides a framework to solve conjugate heat transfer problems analytically. The framework is used to solve two classical heat transfer problems of internal and external flow. The results from this proposed method are validated using a past well validated method from past studies and finite element solver. An interesting result of heat reversal encountered during the analysis is presented and discussed, which demonstrates a possible application of this method in optimizing

cooling parameters. The robustness of this method is demonstrated by solving both internal and external flow problems.

The thermal management approach proposed and modeled in Chapter 3 has been experimentally demonstrated. The experiment and results from the experiments has been shown in Chapter 6. Thermal test cells with an annular channel have been fabricated. Active cooling by passing air through the channel and passive cooling by inserting heat pipe in the channel have been experimentally evaluated. Effect of channel size has also been investigated by doing experiments on thermal test cells with two different channel sizes. The results show effective cooling of the core of the cell and reduced temperature gradient within the cell as desired.

Thermal modeling work in Chapter 1 and 2 has been extended to thermal modeling in the presence of temperature dependent heat generation and thermal runaway prediction. In Chapter 7, a new non-dimensional has been formulated and proposed as a measure of thermal stability of Li-ion cells. The ability of this non-dimensional to quantify thermal stability and predict thermal runaway has been experimentally demonstrated. This non-dimensional has been named Thermal Runaway Number (TRN). Various analyses to analyze the effect of parameters such as thermal conductivity, convective heat transfer coefficient, dimensions of the cell, etc. on the likelihood of thermal runaway has been carried out for possible design optimization and outlining required research efforts to improve safety. Thermal modeling of a Li-ion cell for any arbitrary temperature dependent heat generation has been presented in Chapter 8. The model is used to analyze effect of heat

generation and heat transfer parameters in the presence of Arrhenius heat generation term. The model has also been demonstrated to computer temperature under thermal abuse condition.

REFERENCES

[1] Armand, M., & Tarascon, J. M. (2008). Building better batteries. Nature, 451(7179), 652-657.

[2] Scrosati, B., & Garche, J. (2010). Lithium batteries: Status, prospects and future. Journal of Power Sources, 195(9), 2419-2430.

[3] Winkless, L. (2013). Reducing failure in lithium batteries. Materials Today, 4(16), 108.

[4] Lisbona, D., & Snee, T. (2011). A review of hazards associated with primary lithium and lithium-ion batteries. Process Safety and Environmental Protection, 89(6), 434-442.

[5] Bernardi, D., Pawlikowski, E., & Newman, J. (1985). A general energy balance for battery systems. Journal of the electrochemical society, 132(1), 5-12.

[6] Thomas, K. E., & Newman, J. (2003). Heats of mixing and of entropy in porous insertion electrodes. Journal of power sources, 119, 844-849. [7] A.A. Pesaran, M. Keyser, Proc. Ann. Battery Conf. (2001).

[8] Kim, G. H., Pesaran, A., & Spotnitz, R. (2007). A three-dimensional thermal abuse model for lithium-ion cells. Journal of Power Sources, 170(2), 476-489.

[9] Wang, Q., Ping, P., Zhao, X., Chu, G., Sun, J., & Chen, C. (2012). Thermal runaway caused fire and explosion of lithium ion battery. Journal of power sources, 208, 210-224.

[10] Wang, C. Y., Gu, W. B., & Liaw, B. Y. (1998). Micro-Macroscopic Coupled Modeling of Batteries and Fuel Cells I. Model Development. Journal of the Electrochemical Society, 145(10), 3407-3417.

[11] Du Pasquier, A., Disma, F., Bowmer, T., Gozdz, A. S., Amatucci, G., & Tarascon, J. M. (1998). Differential Scanning Calorimetry Study of the Reactivity

of Carbon Anodes in Plastic Li-Ion Batteries. Journal of the Electrochemical Society, 145(2), 472-477.

[13] Spotnitz, R., and J. Franklin. "Abuse behavior of high-power, lithium-ion cells." Journal of Power Sources 113.1 (2003): 81-100.

[14] Richard, M. N., & Dahn, J. R. (1999). Accelerating rate calorimetry study on the thermal stability of lithium intercalated graphite in electrolyte. I. Experimental. Journal of The Electrochemical Society, 146(6), 2068-2077.

[15] Maleki, H., Deng, G., Anani, A., & Howard, J. (1999). Thermal Stability Studies of Li-Ion Cells and Components. Journal of The electrochemical society, 146(9), 3224-3229.

[16] Aurbach, D., Markovsky, B., Salitra, G., Markevich, E., Talyossef, Y., Koltypin, M., ... & Kovacheva, D. (2007). Review on electrode–electrolyte solution interactions, related to cathode materials for Li-ion batteries. Journal of Power Sources, 165(2), 491-499.

[17] Biensan, P., Simon, B., Peres, J. P., De Guibert, A., Broussely, M., Bodet, J. M., & Perton, F. (1999). On safety of lithium-ion cells. Journal of Power Sources, 81, 906-912.

[18] Roth, E. P., & Nagasubramanian, G. (2000). Thermal stability of electrodes in lithium-ion cells (No. SAND2000-0345J). Sandia National Labs., Albuquerque, NM (US); Sandia National Labs., Livermore, CA (US).

[19] Chen, Y., & Evans, J. W. (1996). Thermal analysis of lithium-ion batteries. Journal of the Electrochemical Society, 143(9), 2708-2712.

[20] Zhang, Z., Fouchard, D., & Rea, J. R. (1998). Differential scanning calorimetry material studies: implications for the safety of lithium-ion cells. Journal of power sources, 70(1), 16-20.

[21] Bandhauer, T. M., Garimella, S., & Fuller, T. F. (2011). A critical review of thermal issues in lithium-ion batteries. Journal of the Electrochemical Society, 158(3), R1-R25.

[22] Drake, S. J., Wetz, D. A., Ostanek, J. K., Miller, S. P., Heinzel, J. M., & Jain, A. (2014). Measurement of anisotropic thermophysical properties of cylindrical Li-ion cells. Journal of Power Sources, 252, 298-304.

[23] Chen, Y., & Evans, J. W. (1993). Heat Transfer Phenomena in Lithium/Polymer-Electrolyte Batteries for Electric Vehicle Application. Journal of the Electrochemical Society, 140(7), 1833-1838.

[24] Fang, W., Kwon, O. J., & Wang, C. Y. (2010). Electrochemical–thermal modeling of automotive Li-ion batteries and experimental validation using a three-electrode cell. International journal of energy research, 34(2), 107-115.

[25] Forgez, C., Do, D. V., Friedrich, G., Morcrette, M., & Delacourt, C. (2010). Thermal modeling of a cylindrical LiFePO 4/graphite lithium-ion battery. Journal of Power Sources, 195(9), 2961-2968.

[26] Chen, S. C., Wan, C. C., & Wang, Y. Y. (2005). Thermal analysis of lithium-ion batteries. Journal of Power Sources, 140(1), 111-124.

[27] Taheri, P., & Bahrami, M. (2012). Temperature rise in prismatic polymer lithium-ion batteries: An analytic approach. SAE International Journal of Passenger Cars-Electronic and Electrical Systems, 5(2012-01-0334), 164-176.

[28] Taheri, P., Yazdanpour, M., & Bahrami, M. (2013). Transient three-dimensional thermal model for batteries with thin electrodes. Journal of Power Sources, 243, 280-289.

[29] Chen, S. C., Wang, Y. Y., & Wan, C. C. (2006). Thermal analysis of spirally wound lithium batteries. Journal of the Electrochemical Society, 153(4), A637-A648.

[30] Tanaka, N., & Bessler, W. G. (2014). Numerical investigation of kinetic mechanism for runaway thermo-electrochemistry in lithium-ion cells. Solid State Ionics, 262, 70-73.

[31] Verbrugge, Mark W. "Three-dimensionai temperature and current distribution in a battery module." AIChE Journal 41.6 (1995): 1550-1562.

[32] Lopez, C. F., Jeevarajan, J. A., & Mukherjee, P. P. (2015). Characterization of lithium-ion battery thermal abuse behavior using experimental and computational analysis. Journal of The Electrochemical Society, 162(10), A2163-A2173.

[33] Smith, K., Kim, G. H., Darcy, E., & Pesaran, A. (2010). Thermal/electrical modeling for abuse-tolerant design of lithium ion modules. International Journal of Energy Research, 34(2), 204-215.

[34] Al Hallaj, S., Maleki, H., Hong, J. S., & Selman, J. R. (1999). Thermal modeling and design considerations of lithium-ion batteries. Journal of Power Sources, 83(1), 1-8.

[35] Shah, K., Drake, S. J., Wetz, D. A., Ostanek, J. K., Miller, S. P., Heinzel, J. M., & Jain, A. (2014). Modeling of steady-state convective cooling of cylindrical Li-ion cells. Journal of Power Sources, 258, 374-381.

[36] Shah, K., Drake, S. J., Wetz, D. A., Ostanek, J. K., Miller, S. P., Heinzel, J. M., & Jain, A. (2014). An experimentally validated transient thermal model for cylindrical Li-ion cells. Journal of Power Sources, 271, 262-268.

[37] Semenov, N. (1959). Some problems in Chemical Kinetics and Reactivity, édit6 par Princeton University Press. Princeton NJ, 2, 331.

[38] Q. Wang, J. Sun, G. Chu, *Proc. 8th Int. Symp. Fire Safety Sci.* (2005) 375-382.

[39] Drake, S. J., Martin, M., Wetz, D. A., Ostanek, J. K., Miller, S. P., Heinzel, J. M., & Jain, A. (2015). Heat generation rate measurement in a Li-ion cell at large

C-rates through temperature and heat flux measurements. Journal of Power Sources, 285, 266-273.

[40] Zhang, G., Cao, L., Ge, S., Wang, C. Y., Shaffer, C. E., & Rahn, C. D. (2014). In situ measurement of radial temperature distributions in cylindrical li-ion cells. Journal of The Electrochemical Society, 161(10), A1499-A1507.

[41] F.P. Incropera, D.P. Dewitt, 'Introduction to heat transfer', 3rd. Ed., Wiley Inc., 2006.

[42] Zhang, J., Wu, B., Li, Z., & Huang, J. (2014). Simultaneous estimation of thermal parameters for large-format laminated lithium-ion batteries. Journal of Power Sources, 259, 106-116.

[43] Wu, M. S., Liu, K. H., Wang, Y. Y., & Wan, C. C. (2002). Heat dissipation design for lithium-ion batteries. Journal of power sources, 109(1), 160-166.

[44] Pesaran, A. A. (2001). Battery thermal management in EV and HEVs: issues and solutions. Battery Man, 43(5), 34-49.

[45] Sabbah, R., Kizilel, R., Selman, J. R., & Al-Hallaj, S. (2008). Active (air-cooled) vs. passive (phase change material) thermal management of high power lithium-ion packs: Limitation of temperature rise and uniformity of temperature distribution. Journal of Power Sources, 182(2), 630-638.

[46] Kizilel, R., Sabbah, R., Selman, J. R., & Al-Hallaj, S. (2009). An alternative cooling system to enhance the safety of Li-ion battery packs. Journal of Power Sources, 194(2), 1105-1112.

[47] Rao, Z., Wang, S., Wu, M., Lin, Z., & Li, F. (2013). Experimental investigation on thermal management of electric vehicle battery with heat pipe. Energy Conversion and Management, 65, 92-97.

[48] Vishwakarma, V., Waghela, C., Wei, Z., Prasher, R., Nagpure, S. C., Li, J., ... & Jain, A. (2015). Heat transfer enhancement in a lithium-ion cell through improved material-level thermal transport. Journal of Power Sources, 300, 123-131.

[49] Lin, X., Perez, H. E., Siegel, J. B., Stefanopoulou, A. G., Li, Y., Anderson, R. D., ... & Castanier, M. P. (2013). Online parameterization of lumped thermal dynamics in cylindrical lithium ion batteries for core temperature estimation and

health monitoring. IEEE Transactions on Control Systems Technology, 21(5), 1745-1755.

[50] Kays, W. M., & Crawford, M. E. Convective Heat and Mass Transfer, McGraw-Hill, New York, 1980.

[51] Shah, R. K., & London, A. L. (1978). Lanimar flow forced convection in duts: a source book for compact heat exchanger analytical data. Academic press.

[52] Graetz, L. (1883). Über die Warmeleitungsfahigheit von Flussingkeiten, part 1. Annalen der Physik und Chemie, 18, 79-94.

[53] Jacob, M. (1949). Heat Transfer, vol. 1, Jonh Wiley & Sons.

[54] Eckert, E. R. G., & Drake Jr, R. M. (1959). Heat and mass transfer, p 485.

[55] Yu, H. S., & Sparrow, E. M. (1971). Local non-similarity thermal boundary-layer solutions. ASME J. Heat Transfer, 93, 328-334.

[56] Sellars, J. R., Tribus, M., & Klein, J. S. (1956). Heat Transfer in Laminar Flow in a Round Tube or Flat Conduit—the Graetz Problem Extended. TRANS. ASME, 78, 441-448.

[57] Tribus, M., & Klein, J. (1953). Forced convection from nonisothermal surfaces. Heat Transfer, A Symposium. Univ. of Michigan, 211.

[58] Yin, X., & Bau, H. H. (1996). The conjugate Graetz problem with axial conduction. Journal of heat transfer, 118(2), 482-485.

[59] Mori, S., Sakakibara, M., & Tanimoto, A. (1974). Steady heat transfer to laminar flow in a circular tube with conduction in the tube wall. Heat Transfer-Jpn. Res, 3(2), 37-46.

[60] Luikov, A. V., Aleksashenko, V. A., & Aleksashenko, A. A. (1971). Analytical methods of solution of conjugated problems in convective heat transfer. International Journal of Heat and Mass Transfer, 14(8), 1047-1056.

[61] Gosse, J. (1980). Analyse simplifiée du couplage conduction—convection pour un écoulement à couche limite laminaire sur une plaque plane. Rev Gen Therm, 228, 967.

[62] Perelman, T. L. (1961). On conjugated problems of heat transfer. International Journal of Heat and Mass Transfer, 3(4), 293-303.

[63] Faghri, M., & Sparrow, E. M. (1980). Simultaneous wall and fluid axial conduction in laminar pipe-flow heat transfer. ASME, Transactions, Journal of Heat Transfer, 102, 58-63.

[64] Shah, R. K., & Bhatti, M. S. (1987). Laminar convective heat transfer in ducts. Handbook of single-phase convective heat transfer, 3.

[65] Shah, K., & Jain, A. (2015). Modeling of steady-state and transient thermal performance of a Li-ion cell with an axial fluidic channel for cooling. International Journal of Energy Research, 39(4), 573-584.

[66] Özışık, M. N. (1993). Heat conduction. John Wiley & Sons.

[67] Carslaw, H. S., & Jaeger, J. C. (1959). Heat in solids (Vol. 1). Clarendon Press, Oxford.

[68] Dorfman, A., & Renner, Z. (2009). Conjugate problems in convective heat transfer. Mathematical Problems in Engineering, 2009.

[69] Weigand, B., & Gassner, G. (2007). The effect of wall conduction for the extended Graetz problem for laminar and turbulent channel flows. International journal of heat and mass transfer, 50(5), 1097-1105.

[70] Aleksashenkto, V. A. (1968). The steady conjugated problem of heat transfer in fluid flow in a semi-infinite tube including the effect of viscous dissipation. J. Eng. Phys, 14(1), 100-108.

[71] Deavours, C. A. (1974). An Exact Solution for the Temperature Distribution in Parallel Plate Poiseuille low. a A, 2, 9v2.

[72] Guedes, R. O. C., & Özişik, M. N. (1992). Conjugated turbulent heat transfer with axial conduction in wall and convection boundary conditions in a parallel-plate channel. International journal of heat and fluid flow, 13(4), 322-328.

[73] Karvinen, R., & Lehtinen, A. (2012). ANALYTICAL SOLUTION FOR A CLASS OF FLAT PLATE CONJUGATE CONVECTIVE HEAT TRANSFER PROBLEMS. Frontiers in Heat and Mass Transfer (FHMT), 2(4).

[74] Pagliarini, G. (1985). A Method to Solwe Conjugate Heat Transfer Problems: The Case of Fully Developed Laminar Flow in a Pipe. Journal of heat transfer, 107, 77.

[75] Pozzi, A., & Lupo, M. (1989). The coupling of conduction with forced convection over a flat plate. International journal of heat and mass transfer, 32(7), 1207-1214.

[76] Bılır, Ş. (1995). Laminar flow heat transfer in pipes including two-dimensional wall and fluid axial conduction. International journal of heat and mass transfer, 38(9), 1619-1625.

[77] Jagad, P. I., Puranik, B. P., & Date, A. W. (2012). An iterative procedure for the evaluation of a conjugate condition in heat transfer problems. Numerical Heat Transfer, Part A: Applications, 61(5), 353-380.

[78] R. Karvinen, Some New Results for Conjugate Heat Transfer in a Flat Plate, Int. J. Heat Mass Transfer, 21 (1978) 1261-1264.

[79] Campo, A., & Schuler, C. (1988). Heat transfer in laminar flow through circular tubes accounting for two-dimensional wall conduction. International journal of heat and mass transfer, 31(11), 2251-2259.

[80] Pop, I., & Ingham, D. B. (1993). A note on conjugate forced convection boundary-layer flow past a flat plate. International journal of heat and mass transfer, 36(15), 3873-3876.

[81] Vynnycky, M., Kimura, S., Kanev, K., & Pop, I. (1998). Forced convection heat transfer from a flat plate: the conjugate problem. International Journal of Heat and Mass Transfer, 41(1), 45-59.

[82] Choobineh, L., & Jain, A. (2013). Determination of temperature distribution in three-dimensional integrated circuits (3D ICs) with unequally-sized die. Applied Thermal Engineering, 56(1), 176-184.

[83] Choobineh, L., & Jain, A. (2012). Analytical solution for steady-state and transient temperature fields in vertically stacked 3-D integrated circuits. IEEE Transactions on Components, Packaging and Manufacturing Technology, 2(12), 2031-2039.

[84] Haji-Sheikh, A., Beck, J. V., & Agonafer, D. (2003). Steady-state heat conduction in multi-layer bodies. International Journal of Heat and Mass Transfer, 46(13), 2363-2379.

[85] E. Kreyszig, 'Advanced engineering mathematics,' 10th Ed., Wiley Inc., 2011.

[86] Pals, Carolyn R., and John Newman. "Thermal modeling of the lithium/polymer battery I. Discharge behavior of a single cell." Journal of the Electrochemical Society 142.10 (1995): 3274-3281.

[87] De Hoog, F. R., Knight, J. H., & Stokes, A. N. (1982). An improved method for numerical inversion of Laplace transforms. SIAM Journal on Scientific and Statistical Computing, 3(3), 357-366.

[88] Hollenbeck, K. J. "INVLAP. M: A matlab function for numerical inversion of Laplace transforms by the de Hoog algorithm." unpublished work (1998). available at http://www.isva.dtu.dk/staff/karl/invlap.htm, accessed 1/01/2012.

[89] Ceraolo, M., Lutzemberger, G., & Marracci, M. (2010, September). High power Lithium Batteries usage in hybrid vehicles. In Vehicle Power and Propulsion Conference (VPPC), 2010 IEEE (pp. 1-5). IEEE.

[90] Kaviany, M. (2002). Principles of heat transfer. John Wiley & Sons.

[91] http://www.ansys.com/Products/Fluids/ANSYS-CFX, last accessed May 4, 2016.

[92] El-Nasr, A. A., & El-Haggar, S. M. (1996). Effective thermal conductivity of heat pipes. Heat and Mass transfer, 32(1), 97-101.

[93] Vishwakarma, V., & Jain, A. (2014). Measurement of in-plane thermal conductivity and heat capacity of separator in Li-ion cells using a transient DC heating method. Journal of Power Sources, 272, 378-385.

[94] Srinivasan, V., & Wang, C. Y. (2003). Analysis of electrochemical and thermal behavior of Li-ion cells. Journal of The Electrochemical Society, 150(1), A98-A106.

[95] Melcher, A., Ziebert, C., Rohde, M., & Seifert, H. J. (2016). Modeling and Simulation of the Thermal Runaway Behavior of Cylindrical Li-Ion Cells—Computing of Critical Parameters. Energies, 9(4), 1-19.

[96] Golubkov, A. W., Fuchs, D., Wagner, J., Wiltsche, H., Stangl, C., Fauler, G., ... & Hacker, V. (2014). Thermal-runaway experiments on consumer Li-ion batteries with metal-oxide and olivin-type cathodes. RSC Advances, 4(7), 3633-3642.

Biographical Information

Krishna Shah had studied Mechatronics as an undergraduate student at Sardar Patel University in India. He graduated with B.E. in Mechatronics in 2011. He joined University of Texas at Arlington (UT Arlington) as a graduate student in the Fall of 2012. His research at UT Arlington focused on understanding heat transfer in Li-ion cells by doing theoretical analysis and experiments. He also worked at Lawrence Berkeley National Laboratory (LBNL) as a visiting student researcher. He contributed to the project on making microscale thermal measurements in Li-ion cells at LBNL. His interest is in continuing research work in the field of heat transfer and explore the broader area of heat transfer in the coming years.

APPENDIX A
Copy of License/Agreement to reprint from Journal articles for the purpose of Thesis/Dissertation

ELSEVIER LICENSE
TERMS AND CONDITIONS

Aug 08, 2017

This Agreement between Krishna Shah ("You") and Elsevier ("Elsevier") consists of your license details and the terms and conditions provided by Elsevier and Copyright Clearance Center.

License Number	4164021498281
License date	Aug 08, 2017
Licensed Content Publisher	Elsevier
Licensed Content Publication	Journal of Power Sources
Licensed Content Title	Modeling of steady-state convective cooling of cylindrical Li-ion cells
Licensed Content Author	K. Shah,S.J. Drake,D.A. Wetz,J.K. Ostanek,S.P. Miller,J.M. Heinzel,A. Jain
Licensed Content Date	Jul 15, 2014
Licensed Content Volume	258
Licensed Content Issue	n/a
Licensed Content Pages	8
Start Page	374
End Page	381
Type of Use	reuse in a thesis/dissertation
Intended publisher of new work	other
Portion	full article
Format	electronic
Are you the author of this Elsevier article?	Yes
Will you be translating?	No
Title of your thesis/dissertation	MODELING AND MEASUREMENTS OF THERMAL TRANSPORT IN LI-ION BASED ENERGY CONVERSION AND STORAGE DEVICES
Expected completion date	Aug 2017
Estimated size (number of pages)	180
Requestor Location	Krishna Shah 914 Greek Row Dr Apt 138 ARLINGTON, TX 76013 United States Attn: Krishna Shah
Publisher Tax ID	98-0397604
Total	0.00 USD

ELSEVIER LICENSE
TERMS AND CONDITIONS

Aug 08, 2017

This Agreement between Krishna Shah ("You") and Elsevier ("Elsevier") consists of your license details and the terms and conditions provided by Elsevier and Copyright Clearance Center.

License Number	4164021399583
License date	Aug 08, 2017
Licensed Content Publisher	Elsevier
Licensed Content Publication	Journal of Power Sources
Licensed Content Title	An experimentally validated transient thermal model for cylindrical Li-ion cells
Licensed Content Author	K. Shah,S.J. Drake,D.A. Wetz,J.K. Ostanek,S.P. Miller,J.M. Heinzel,A. Jain
Licensed Content Date	Dec 20, 2014
Licensed Content Volume	271
Licensed Content Issue	n/a
Licensed Content Pages	7
Start Page	262
End Page	268
Type of Use	reuse in a thesis/dissertation
Intended publisher of new work	other
Portion	full article
Format	electronic
Are you the author of this Elsevier article?	Yes
Will you be translating?	No
Title of your thesis/dissertation	MODELING AND MEASUREMENTS OF THERMAL TRANSPORT IN LI-ION BASED ENERGY CONVERSION AND STORAGE DEVICES
Expected completion date	Aug 2017
Estimated size (number of pages)	180
Requestor Location	Krishna Shah 914 Greek Row Dr Apt 138 ARLINGTON, TX 76013 United States Attn: Krishna Shah
Publisher Tax ID	98-0397604
Total	0.00 USD

Sharing guidelines for Wiley journal articles

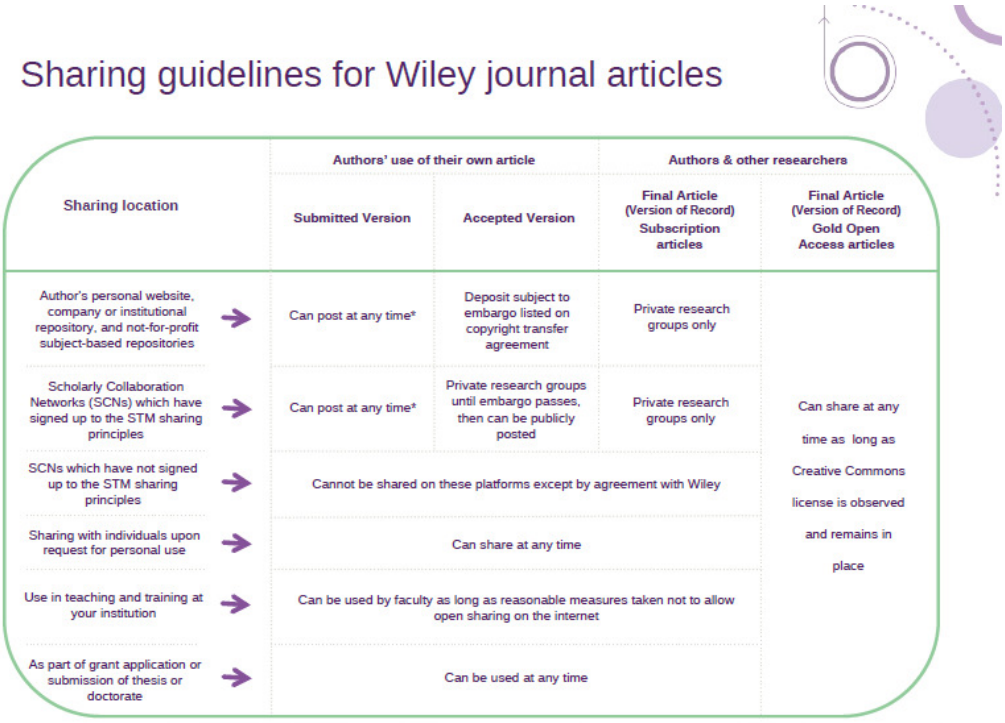

Sharing location	Authors' use of their own article		Authors & other researchers	
	Submitted Version	Accepted Version	Final Article (Version of Record) Subscription articles	Final Article (Version of Record) Gold Open Access articles
Author's personal website, company or institutional repository, and not-for-profit subject-based repositories →	Can post at any time*	Deposit subject to embargo listed on copyright transfer agreement	Private research groups only	Can share at any time as long as Creative Commons license is observed and remains in place
Scholarly Collaboration Networks (SCNs) which have signed up to the STM sharing principles →	Can post at any time*	Private research groups until embargo passes, then can be publicly posted	Private research groups only	
SCNs which have not signed up to the STM sharing principles →	Cannot be shared on these platforms except by agreement with Wiley			
Sharing with individuals upon request for personal use →	Can share at any time			
Use in teaching and training at your institution →	Can be used by faculty as long as reasonable measures taken not to allow open sharing on the internet			
As part of grant application or submission of thesis or doctorate →	Can be used at any time			

For more details, view the full policy online at http://olabout.wiley.com/WileyCDA/Section/id-826716.html

* This is the copyright policy, individual journals may operate different editorial policies and authors should consult the relevant author guidelines.

WILEY

ELSEVIER LICENSE
TERMS AND CONDITIONS

Aug 08, 2017

This Agreement between Krishna Shah ("You") and Elsevier ("Elsevier") consists of your license details and the terms and conditions provided by Elsevier and Copyright Clearance Center.

License Number	4164010750970
License date	Aug 08, 2017
Licensed Content Publisher	Elsevier
Licensed Content Publication	International Journal of Heat and Mass Transfer
Licensed Content Title	An iterative, analytical method for solving conjugate heat transfer problems
Licensed Content Author	Krishna Shah,Ankur Jain
Licensed Content Date	Nov 1, 2015
Licensed Content Volume	90
Licensed Content Issue	n/a
Licensed Content Pages	9
Start Page	1232
End Page	1240
Type of Use	reuse in a thesis/dissertation
Portion	full article
Format	electronic
Are you the author of this Elsevier article?	Yes
Will you be translating?	No
Title of your thesis/dissertation	MODELING AND MEASUREMENTS OF THERMAL TRANSPORT IN LI-ION BASED ENERGY CONVERSION AND STORAGE DEVICES
Expected completion date	Aug 2017
Estimated size (number of pages)	180
Requestor Location	Krishna Shah 914 Greek Row Dr Apt 138 ARLINGTON, TX 76013 United States Attn: Krishna Shah
Publisher Tax ID	98-0397604
Total	0.00 USD
Terms and Conditions	

ELSEVIER LICENSE
TERMS AND CONDITIONS

Aug 08, 2017

This Agreement between Krishna Shah ("You") and Elsevier ("Elsevier") consists of your license details and the terms and conditions provided by Elsevier and Copyright Clearance Center.

License Number	4164021304852
License date	Aug 08, 2017
Licensed Content Publisher	Elsevier
Licensed Content Publication	Energy
Licensed Content Title	Experimental and numerical investigation of core cooling of Li-ion cells using heat pipes
Licensed Content Author	K. Shah,C. McKee,D. Chalise,A. Jain
Licensed Content Date	Oct 15, 2016
Licensed Content Volume	113
Licensed Content Issue	n/a
Licensed Content Pages	9
Start Page	852
End Page	860
Type of Use	reuse in a thesis/dissertation
Intended publisher of new work	other
Portion	full article
Format	electronic
Are you the author of this Elsevier article?	Yes
Will you be translating?	No
Title of your thesis/dissertation	MODELING AND MEASUREMENTS OF THERMAL TRANSPORT IN LI-ION BASED ENERGY CONVERSION AND STORAGE DEVICES
Expected completion date	Aug 2017
Estimated size (number of pages)	180
Requestor Location	Krishna Shah 914 Greek Row Dr Apt 138 ARLINGTON, TX 76013 United States Attn: Krishna Shah
Publisher Tax ID	98-0397604
Total	0.00 USD

ELSEVIER LICENSE
TERMS AND CONDITIONS

Aug 08, 2017

This Agreement between Krishna Shah ("You") and Elsevier ("Elsevier") consists of your license details and the terms and conditions provided by Elsevier and Copyright Clearance Center.

License Number	4164021165801
License date	Aug 08, 2017
Licensed Content Publisher	Elsevier
Licensed Content Publication	Journal of Power Sources
Licensed Content Title	Experimental and theoretical analysis of a method to predict thermal runaway in Li-ion cells
Licensed Content Author	Krishna Shah,Divya Chalise,Ankur Jain
Licensed Content Date	Oct 31, 2016
Licensed Content Volume	330
Licensed Content Issue	n/a
Licensed Content Pages	8
Start Page	167
End Page	174
Type of Use	reuse in a thesis/dissertation
Portion	full article
Format	electronic
Are you the author of this Elsevier article?	Yes
Will you be translating?	No
Title of your thesis/dissertation	MODELING AND MEASUREMENTS OF THERMAL TRANSPORT IN LI-ION BASED ENERGY CONVERSION AND STORAGE DEVICES
Expected completion date	Aug 2017
Estimated size (number of pages)	180
Requestor Location	Krishna Shah 914 Greek Row Dr Apt 138 ARLINGTON, TX 76013 United States Attn: Krishna Shah
Publisher Tax ID	98-0397604
Total	0.00 USD